Mathematical Modelling, Flight Control System Design and Air Flow Control Investigation for Low Speed UAVs

a thesis submitted by

Ibrahim Elgayar

for the Degree of

Doctor of Philosophy (PhD)

School of Engineering and Mathematical Sciences
City University London

July 2013

Table of Contents

List of Tables

List of Figures

Acknowledgment

Firstly, I owe great thanks to my supervisor, Dr Efstathios Milonidis, for his excellent supervision, guidance and encouragement. I would also like to express my gratitude to my second supervisor, Professor Nicos Karcanias for his constructive feedback. . I am also indebted to Professor George Halikias for his help in the area of control design.

My deepest gratitude to ERSRC for sponsoring me to conduct this research. I would further like to extend my thanks to the School of Engineering and Mathematical Sciences for supporting me during my time at the university.

Finally, my deepest acknowledgment and dedication of this thesis goes to my wife Dr Souad Mohamed and my family for their love, continuous encouragement and support.

Copyright Declaration

Abstract

The demand for unmanned aerial vehicles (UAVs) has increased dramatically in the last decade from reconnaissance missions to attack roles. As their missions become more complex, advances in endurance and manoeuvrability become crucial. Due to the advances in material fabrication, wing morphing can be seen as an ideal solution for UAVs to provide improvements by overcoming the weight drawback.

This thesis investigates the area of aircraft design and simulation for low speed UAVs looking at performance enhancements techniques for low speed UAVs, and their effects on the aerodynamic capabilities of the wing. The focus is on both suitable control design and wing morphing techniques based on current research findings. The low speed UAV X-RAE1 is used as the test bed for this investigation and is initially analytically presented as three dimensional body where the equations relate to the forces and moments acting on the UAV.

A linearised model for straight flight at different velocities is implemented and validated against a non-linear model. Simulations showed the X-RAE1 to have acceptable stability properties over the design operating range.

Control design techniques, linear quadratic regulators (LQR) and H-infinity optimisation with Loop Shaping Design Procedure (LSDP), are used to design simple control schemes for linearised longitudinal model of the X-RAE1 UAV at different velocities. The effectiveness and limitations of the two design methods show that both designs are very fast, with settling times 2-3 seconds in the height response and remarkably low variation of the results at different velocities.

Computational fluid dynamics is then used to investigate and simulate the impact of introducing smart effector arrays on a UAV. The smart effector array produces a form of active flow control by providing localised flow field changes. These induced changes have direct impact on the aerodynamic forces and showed a substantial increase of lift at low angles of attack. There was also a significant increase to the lift to drag ratio at high angles of attack which resulted to a delay in stall.

Symbols and Abbreviations

A	wing aspect ratio
a	Vector of unknown parameters
b	wing span
C_D	drag coefficient
C_L	lift coefficient
C_I	rolling moment coefficient
C_m	pitching moment coefficient
C_n	yawing moment coefficient
C_y	side force coefficient
c	mean aerodynamic chord
D	drag
e	eccentricity
F	force
I_x, I_y, I_z	moments of inertia
I_{xy}, I_{yz}, I_{zx}	products of inertia
L	lift, rolling moment
l_t	tail arm
M	pitching moment
m	aircraft mass
N	yawing moment
P, p	roll rate (body axes)
Q, q	pitch rate (body axes)
R, r	yaw rate (body axes)
S	wing area
S_t	tail area
T	thrust
U, u	forward velocity (body axes)
V, v	side velocity (body axes)
$\underset{\sim}{V_T}$	total rectilinear velocity
W, w	downward velocity (body axes)
X	force (aprat from gravitational) along x body axes
$\overset{o}{X}_u, ..., \overset{o}{N}_\varsigma$	basic aerodynamic derivatives
$Xu, ..., N$	normalised aerodynamic derivatives
$\underset{\sim}{x}$	state vector
Y	side force (aprat from gravitational) in body axes
Z	force (aprat from gravitational) along z body axes

H_∞	is the set of transfer functions G with $\|G\|_\infty < \infty$
$\sigma(s)$	principal gain (singular value)
$\bar{\sigma}$(s), $\underline{\sigma}$(s)	largest and smallest singular values
α	angle of attack
β	angle of sideslip
δ_T	throttle setting
ε	downwash angle, thrust line orientation, wing twist
ς	rudder deflection
η	elevator deflection
θ	pitch angle
λ	taper ration
ξ	aileron deflection
ρ	air density
φ	roll angle
ϕ	yaw angle
$\underset{\sim}{\Omega}$	total angular velocity

3D	Three dimensions: x, y and z.
6DOF	Six Degrees-of-Freedom dynamics
CFD	Computational Fluid Dynamics
LSDP	Robust Control Loop-Shaping Design Procedure
LQG	Linear Quadratic Gaussian
LQR	Linear quadratic regulator
MIMO	Multi-Input Multi-Output
PZT	Piezoelectric actuators
UAV	Unmanned Air Vehicle
SMA	Shape Memory Alloys
SISO	Single-Input Single-Output
SMP	Shape Memory Polymers

CHAPTER

1 Introduction

Research in aircraft flight and control Engineering is an on-going battle to revolutionise aviation with the aim to reduce emissions and engine noise, enhance passenger safety, aircraft capacity and mobility. The National Aeronautics and Space Administration (NASA) has stated that improvement in aviation is critical to the economic health, national security, and the overall quality of life (Washburn, 2002). This resulted in a multi-disciplinary approach to technology development led by researchers from fluid mechanics/aerodynamics, material science, structural mechanics, and control theory.

This chapter introduces the focus of interest of this research. It presents the area of aircraft design and simulation for low speed UAVs. This compromises of the formation of the six degrees of freedom mathematical model for a low speed UAV. This model describes analytically the motions of the UAV as a three dimensional body where the equations relate to the forces and moments acting on the UAV. This in turn provides the model parameter for aircraft simulation and a basis for the control system design. Control design techniques LQR and H_∞ optimisation with Loop Shaping Design Procedure (LSDP) are applied to a UAV and results are presented.

Computational fluid dynamics is then used to investigate and simulate the impact of introducing a smart effector arrays on a UAV. The smart effector array produces a form of active flow control by providing localised flow field changes. These induced changes have direct impact on the aerodynamics forces. The aim, objectives and an overview of the context of each chapter is then provided.

1.1 Background and Motivation

The area of active flow control specialises in developing devices for flight vehicles that affect their flow-field to generate aerodynamic forces. These aerodynamic forces can be used as control forces or used to improve flight efficiency. Current flight vehicles use relatively small number of high authority control surfaces known as rudder, ailerons, elevators and flaps to produce control forces. The advancements in material science has brought forward a new generation of smaller and less specialised distributed devices. These devices can be grouped together in an array and operate in conjunction with the flight vehicles main control surfaces or replacing them altogether. The name given to these devices are *Smart Effector Arrays*. The smart effector arrays can also be used to increase flight efficiency by producing aerodynamic forces which increase the lift drag ratio, giving the flight vehicle more speed for the same angle of attack. To achieve the required level of flow control a combination of the right smart effector array and placement technique is needed.

The uniqueness of the smart effector comes from its material composition, which is made up of an actuator, sensor and controller all embedded into one structure. An illustrative view of composition of smart effector is given below in Figure 1-1 (Hurlebaus, 2006).

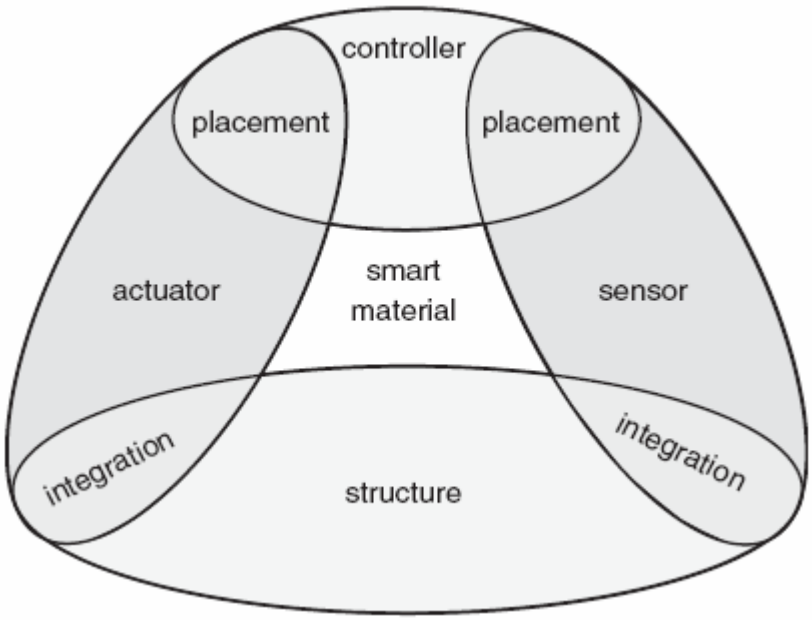

Figure 1-1 Illustration of Smart Effector device (Hurlebaus, 2006)

The materials used in developing the smart effector are labelled as smart materials, which have interesting and unusual properties. They can "remember" configurations and can conform to them in response to a specific stimulus these being changes in electricity, heat, or magnetic waves. Examples of smart materials are electrostrictive materials, magnetostrictive materials, shape memory alloys, magneto- or electrorheological fluids, polymer gels, and piezoelectric materials.

Once the smart effector array is developed it needs to be incorporated within the flight vehicle control system. This is a challenging task as it requires precise placement and real-time feedback control. The effectors need to be placed where they will have the highest impact on flow control. The control system needs to be aware of which effectors need to be triggered to produce the required response force for a given flight path. Once implemented an intelligent control system can be achieved offering many potential advantages for flight control, including reduced fuel consumption, enhanced maneuverability, robustness and health monitoring. A number of effector arrays and placement techniques have being researched; jets (Sandra, 2007), shape-change blisters (Raney, 2004) and micro flaps (Lee, 2005) showing promising results for the future of aviation.

1.2 Importance of the Research and Potential Outcomes

An unmanned aerial vehicle (UAV) is an aircraft without a human pilot on board. Its flight is either controlled autonomously based on pre-programmed flight plans, or under the remote control of a pilot. UAVs are currently used for a number of missions, including reconnaissance and attack roles. The demand for UAV is growing drastically due to their unique capabilities and advances in manoeuvrability are being sought out. All of which highlights the importance of creating an accurate mathematical model of a UAV to be able to successfully design new innovative ideas.

Compared to supersonic aircraft, the small or low speed planes require more dramatic wing variations for a noticeable and practical change in their aerodynamic properties. This points us to the crux of the development of low speed/small shape morphing planes which is the large weight penalty for an addition of actuation systems capable of

causing wing variations to the overall allowed weight. To address the above challenge, any successful conceptual design for shape morphing of low speed/small aircraft should:

- Undergo large geometry change
- Use smart materials for actuation
- Use the smart material actuators for supporting part of the aerodynamic loads
- Have integrated and distributed actuators to avoid transmission mechanisms
- Use advance light weight composites for the fixed structure and the skin.

The concept of flow control uses smart materials which are made of light weight composites such as shape memory alloys. The key concept of flow control is to affect the flow-field round the UAV which has an impact on the aerodynamics and in turn can be used to reduce drag or produce a control force. The geometry change provided by a single flow control devices is considered small but when combined into an array of devices as a skin round the UAV all working synchronously together they will have a greater effect. The UAV X-RAE1 (Trebble, 1985a) will be used as a test bed for this research due to its classification as a low speed UAV. The X-RAE1 is an experimental UAV with control surfaces and the UAV is powered by a 1.5cc two stroke engine.

The potential outcomes of this research will be the development of a six degrees of freedom mathematical model of an experimental UAV and an analysis of its dynamic responses. The design of a multivariable, robust flight control system and the comparison of selected control techniques. The identification of current state of the art wing morphing techniques capable of improving overall performance for a UAV and carrying out CFD analysis on flow control devices.

1.3 Research Aim, Objectives and Contribution of the Work

1.3.1 Research Aim

The main research aim of this work is to analyse performance enhancement techniques for low speed UAVs by evaluating the aerodynamic forces lift, drag and drag/lift ratio from the CFD results of the X-RAE1 wing with embedded effector array against the

original X-RAE1 wing from wind tunnel data. The endurance of the wing can be examined across different angles of attack where an increase in endurance can be seen by an increase in lift and a decrease in drag, which subsequently leads to a decrease in drag/lift ratio.

1.3.2 Research Objectives

In addressing the aim, the study has a number of objectives, based on literature analysis and modelling implementation is listed below and illustrated in Figure 1-2 :

- To improve and correct an existing nonlinear six degrees of freedom mathematical model of an experimental UAV X-RAE1, which is then linearised for straight level flight.

- Design a multivariable, robust flight control system for the X-RAE1 using LQR and H_∞ optimisation with loop shaping.

- CFD modelling and analysis of the X-RAE1 wing with positioned embedded effector array. Validating and comparing the CFD model to experimental data taken from the original X-RAE1 wing.

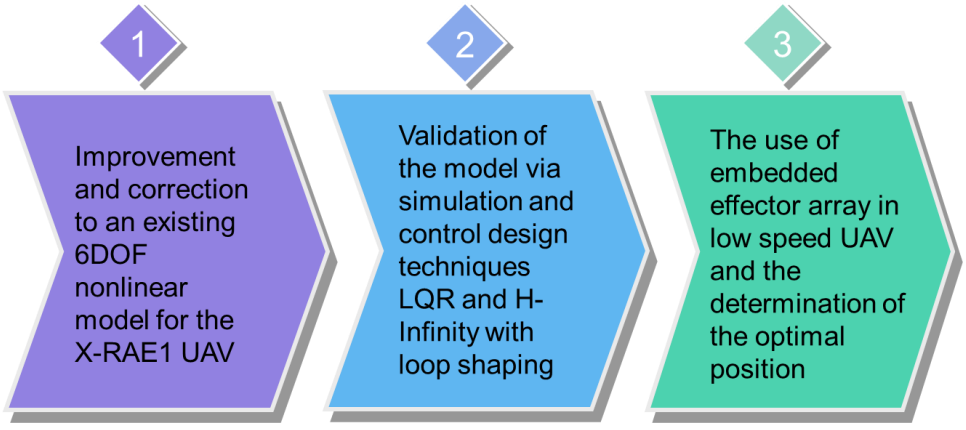

Figure 1-2 Main research objectives in consecutive order

1.3.3 The Main Contribution of the Work

1. Improvement and correction to an existing six DOF nonlinear model has been undertaken for the X-RAE1 UAV based on a combination of theoretical/ empirical (ESDU datasheets) and experimental wind tunnel data.

2. Validation of the derived nonlinear model via nonlinear/linear simulation studies. Use of preliminary control methodologies, i.e. LQR and H_∞ with loop shaping to illustrate that proposed model is fit for control purposes.

3. The use of embedded effector array for active flow control in low speed UAV through CFD analysis in particular determination of the optimal position of the embedded effector array on the wing.

1.3.4 Dissemination of Results

The main results of this work will be submitted for publication in technical journals and conference proceedings. The first paper is due to be submitted to the conference RED-UAS (Research, Education and Development of Unmanned Aerial Systems) in November 2013. This paper will cover the mathematical modelling and control of the XRAE-1 UAV presented in chapters 4 and 5. The second paper due to be submitted in December 2013 to the Unmanned Systems journal published by world scientific will cover the research carried out on smart effector arrays for low speed UAVs as presented in chapter 6.

1.4 Thesis Structure

The structure of the presented research is based on a framework of theory, modelling and simulation. A brief description of the material covered in each chapter is given below, to provide an overview of the approach followed in this thesis:

1.4.1 Chapter 2: Literature Review

This chapter provides a detailed critical analysis of the current state of the art research in wing morphing technologies that can be applied to low speed UAVs such as the X-

RAE1 UAV. It commences by briefly discussing the need for shape morphing and the advances in shape morphing materials. The chapter then provides a breakdown of wing morphing variations and current research in each area highlighting the advantages and drawbacks of these implementations in respect to low speed UAVs. Subsequently, flow control techniques are investigated further as a viable solution for the low speed UAVs due to the performance capabilities and positive integration.

1.4.2 Chapter 3: Aircraft Mechanics Review

This Chapter gives an overview of the fundamental areas of aircraft mechanics which will be used in the derivation of the mathematical model and simulation. This encapsulates the breakdown of aircraft motion into pitch, roll and yaw. The non-dimensional reference parameters of the aircraft geometry and the control surfaces in addition to the three axis systems and their translation between each other. This is followed by a brief presentation of the derivation of the equations of motion and their linearisation which is to be implemented for the X-RAE1 UAV.

1.4.3 Chapter 4: The Mathematical Modelling of the X-RAE1 UAV

The concepts and principles presented in chapter three are used in the development of the six degrees of freedom model for the X-RAE1. A combination of static wind-tunnel tests and ESDU data sheets is used for the formulation of the aerodynamic characteristics of the UAV. A linear and a non-linear model is then presented followed by the dynamics for straight level flight for the X-RAE1.

1.4.4 Chapter 5: Control System Design

This chapter leads with the design of a multivariable, robust flight control system for the X-RAE1 using LQR and H-infinity optimisation with loop shaping capable of stabilising the UAV in-flight during manoeuvrability. Both control design techniques are analysed and responses compared.

1.4.5 Chapter 6: Effector Array CFD Model

This chapter provides an outline of the Computational Fluid Dynamics Procedure used to construct both a two and three dimensional models of the X-RAE1 unmanned aircraft wing. The first model is a reconstruction of the actual wing which is a Wortmann FX63-137 wing which has a concave lower surface and is used to validate the CFD results against experimental data. The second model is the modified Wortmann FX63-137 with an embedded effector array to modify the air flow. The effect of having an effector array is analysed for lift, drag and moments. Contours around the wing are examined to facilitate the results obtained.

1.4.6 Chapter 7: Conclusions and Recommendations for Future Work

This chapter provides a summary of the research, and presents the main contributions to the field of aeronautics followed by an outline of potential areas of further research.

1.4.7 Appendices: Derivation of the Aerodynamic Derivatives

The appendices cover the derivation and correction of both the longitudinal and lateral aerodynamic derivatives.

CHAPTER 2

Literature Review

This chapter provides a detailed critical analysis of the current state of the art research in wing morphing technologies that can be applied to low speed UAVs such as the X-RAE1 UAV. It commences by briefly discussing the need for shape morphing and the advances in shape morphing materials. The chapter then provides a breakdown of wing morphing variations and current research in each area highlighting the advantages and drawbacks of these implementations in respect to low speed UAVs. Subsequently, flow control techniques are investigated further as a viable solution for the X-RAE1 due to their performance capabilities and suitability.

2.1 Shape Morphing Materials

In the field of aeronautics, "shape morphing" has been used to identify those aircraft that can undergo certain geometrical changes to enhance or adapt to their mission profiles. Current interest in morphing has been fuelled by advances in smart materials. These advances have led to series of breakthroughs in a wide variety of disciplines which have the potential to produce large improvements in aircraft flight (Valasek, 2012). There is no exact definition or an agreement between the researchers about the type or the extent of the geometrical changes necessary to qualify an aircraft for the term "shape morphing" technology. However, there is a general agreement that the conventional hinged control surfaces or high lift devices, such as flaps or slats that provide discrete geometry changes cannot be considered as "morphing" (Sofla et al., 2010).

The interest of wing morphing lies in the benefits that can be achieved which can be defined as four applications (Friswell and Inman, 2006):

1. Improvement of the aircraft performance to expand its flight envelope
2. Replacement of conventional control surfaces for flight control to improve the performance and stealth characteristics
3. Reduction of the drag to improve the range
4. Reduction of the vibration or the control of flutter

These benefits are achievable due to the advances in material technology being used to produce shape morphing. A recent example is wing morphing for solar powered high altitude aircraft which can fold in such a way to orient a solar panel to be hit more directly by the sun's rays at specific times of the day (Dewey and Pezhman, 2013). These Advances have enabled the development of devices which can serve as both sensors and actuators. Integrating these devices into a structure together with a controller, enables the material to become "Smart". Incorporating actuators within a composite structure to make the structure bend enables the concept of shape control or morphing to be implemented. A smart structure should possess the ability to sense its internal and external environment. It should then be able to communicate the sensory signals via appropriate pathways to one or several signal processing and control modules, where the information is analysed and appropriate actions are decided. If necessary, the decisions must be conveyed to actuators incorporated within the structure, which respond by altering its characteristics such as the shape, size, stiffness, position, or natural frequency (Uttamchandani, 1994).

The actuators incorporated in the composite wing structure may induce the wing twist, camber shaping and control surface deformations. Additionally, these materials may produce structures with variable stiffness. The aerodynamic efficiency of a control surface may also be controlled and improved by changing the flow conditions over the lifting surface.

It is common to classify smart materials as:

(a) Intrinsically adaptive materials: This category includes Shape Memory Alloys (SMA) and Shape Memory Polymers (SMP). When stimulated, these materials are subjected to transformations in their molecular or microscopic structures. These transformations induce changes in material mechanical properties. SMAs and SMPs can undergo large free strains and exhibit large blocking forces. Nevertheless, they have a slow response and a limited efficiency.

(b) Active materials: This class includes electro-active polymers (EAP), piezoelectric ceramics (PZT), and magnetostrictive materials. They act as transducers converting electrical, magnetic, or thermal energy into a mechanical energy. Piezo-ceramics exhibit a much lower free strain but they are capable of producing quite high blocking forces, and sensibly more efficient

The material choice depends on the specific morphing purpose. If the morphing is dedicated to flight control, the morphing system should exhibit (Fontanazza et al., 2006):

1. Relatively fast dynamic,
2. Capability to operate over a wide range of flight conditions,
3. High reliability,
4. Capability of repetitive actuation,
5. Robustness against uncertainties and disturbances such as gust loads,
6. Low power consumption.

Therefore, the ideal material should respond quickly to the external stimuli, be capable of large and recoverable free strains; transform effectively the input energy into mechanical energy. Additionally, it should not be affected by fatigue issues. The use of smart materials simplifies mechanical systems and thus reduces operating costs. Moreover, it significantly expands the functionality or operating range so that a single system can have multiple uses with a substantial adaption to different conditions. Furthermore, these materials increase the resilience of the system by improving diagnostics, addressing unforeseen problems, and enabling new capabilities.

2.2 Shape Morphing Variations

Significant geometric variations of an aircraft wing during flight can allow efficient performance during different flight regimes, or permit multi-role missions that are impossible without the aircraft reconfiguration. Conventional aircraft use mechanisms to change discretely the wing area in different flight configurations. These configurations include take off, climb, cruise and landing. The discrete shape change is achieved by extending or retracting flaps, slats, tabs, ailerons to either modify the wing area and the airfoil camber for additional lift or the aircraft controllability characteristics.

Several methods exist to increase the efficiency of different flight aspects of an aircraft through changing the aerodynamic characteristics of the wing. Changing the span or the aspect ratio of the aircraft wing alters the aircraft lift characteristics, and stealth characteristics for military aircraft. Loitering can be performed more efficiently by changing the airfoil shape through drooping the wings, increasing the airfoil camber, or twisting the wing. Performing any of these changes by morphing during a mission would give increased efficiency in the loiter stage (Cesnik et al., 2004). Table 2.1 defines the aerodynamic advantages of varying the wing geometry.

	Max Speed	**Range**	**Landing Distance**	**Take-Off Distance**	**Manoeuvr-ability**	**State Change Effectiveness**	**Relative Total**
Span	5	4	4	4	3	4	24
Aspect Ratio	3	4	3	3	2	3	18
Sweep	5	5	5	5	4	4	26
Taper Ratio	1	2	1	1	1	1	7
Thickness / Chord Ratio	1	2	1	1	1	1	7
Camber	2	2	5	5	5	4	23

Table 2-1 Effects of the change type on the aerodynamic characteristics in the scale 1-5 (Cesnik et al., 2004)

It is evident from the table above that changing the sweep, the span or the airfoil camber provides significant aerodynamic and economic advantages. Increase in the wing aspect ratio will result in a rise of both endurance and range. Therefore, by tailoring the wing geometry through morphing concepts, its lift and drag characteristics can be adjusted to a variety of missions or flight segments.

Adapting (Sofla et al., 2010) model of wing morphing classification to include boundary layer local deformations for flow control and by reviewing morphing concepts presented in (Barbarino et al., 2011, Gomez and Garcia, 2011) the wing morphing concepts can be classified into four major types planform alternation, airfoil adjustment, out of plane transformation and boundary layer local deformations. This is presented below in Figure 2-1.

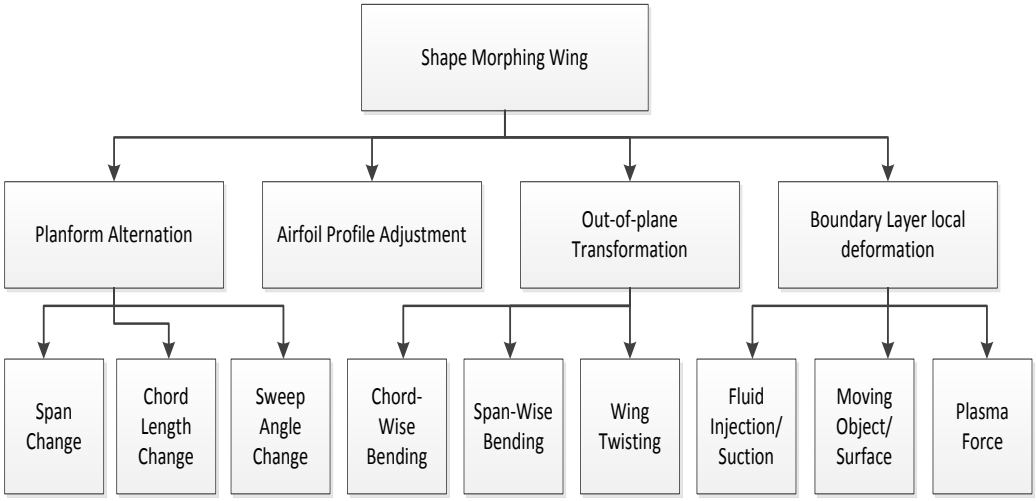

Figure 2-1 Classification for shape morphing of wing

The planform alternation is performed through the wing area resizing by changing parameters including the span, chord length and sweep angle. The airfoil adjustment regroups designs that can alter the wing profile with no significant change in the wing camber; the wing thickness control comes under this category. The out-of-plane transformations include the wing twist, the chord and span-wise camber changes. Boundary layer Local deformations includes flutter control devices and flow control devices.

A summary of current research into shape morphing concepts for aircraft wings that undergo substantial changes of airfoil profile, planform, chord or span-wise camber is presented first focusing on active flow control technologies which create local deformations. These methods consist of techniques able to influence the flow close to the surface of the airfoil altering the airfoil pressure distribution and in affect influencing the aero-dynamics characteristics of the airfoil. Most known methods are

boundary layer suction/blowing, synthetic jets, elastic membranes and plasma actuators. Preference is given to the designs that consist of smart materials such as shape memory alloy actuators (SMA), piezoelectric actuators (PZT) or shape memory polymers (SMP).

2.3 Wing Planform Alternations

The wing planform alternation is either singularly or a combination of alterations to the span, chord length or sweep angle at various flight conditions.

2.3.1 Wing Span Morphing

The main advancements in wing span morphing have been by designing telescopic structures. The underlying design in a telescopic wing is several segments with reducing cross sectional area, such that each segment can encapsulate the adjacent inner segment. Depending on the length required for the wing the number of segments can be determined.

In 1997, Gevers Aircraft developed a 6-seat 'triphibious' aircraft designed for unprecedented speed, utility, safety, and ruggedness. It uses a telescopic wing to adapt the aircraft geometry to the flight conditions. The wing is designed for high-speed cruise when retracted and enhanced low speed capabilities when extended. It is composed of a fixed centre section and two extendable outer sections, using an overlapping extension spar system. The centre section is a high-speed wing (low drag and strong) and the completely retractable high lift section moves in a span-wise direction. Figure 2-2 shows the extension/retraction mechanism as a simple system of cables that prevent asymmetric extension and the extendable spars interlock guided on rollers to drive the span-wise increase (Gevers, 1997).

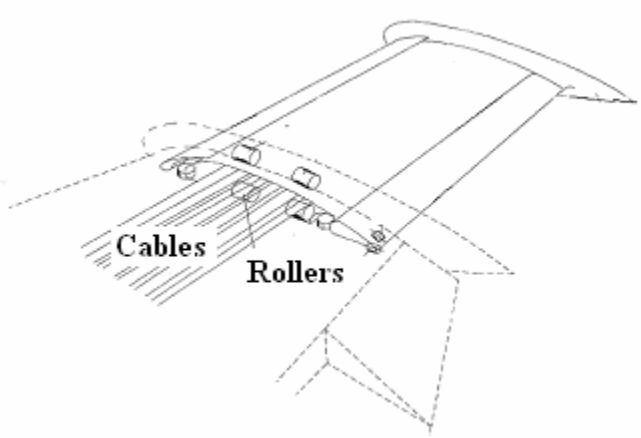

Figure 2-2 Gevers Aircraft's Telescopic Wing (Gevers, 1997)

Pines (2003) and Blondeu (2004) designed and fabricated a three segmented telescopic wing with inflatable actuators replacing the traditional spars. These pneumatic spars consisted of three concentric cylindrical aluminium tubes that could achieve variation span configurations. The alignment of the sliding tubes was ensured using ceramic linear bearings. Their full scale telescopic spar could be smoothly deployed and retracted using input pressures of 340-480 kPa. The wing achieved a change of 114% of the wing aspect ratio. Experimentally it was shown that the drag to lift ratio of the fully extended telescopic wing was about 25% lower that it's rigid fixed wing. Figure 2-3 presents the design drawings. The telescopic wing is represented in three different stages of extension, with and without the skin.

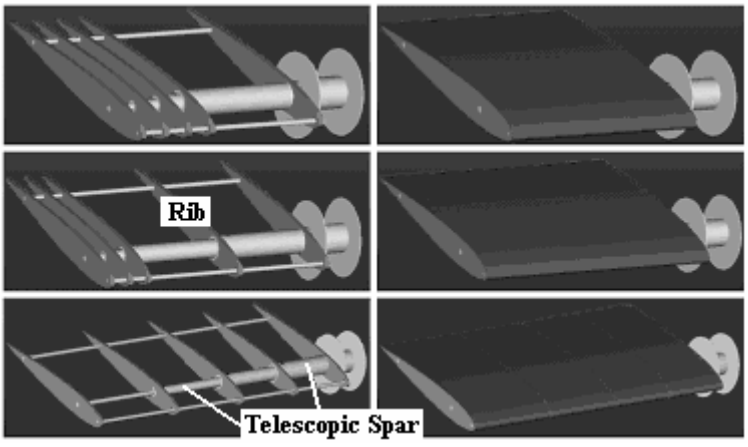

Figure 2-3 Conceptual Drawings of the Pneumatic Telescopic Wing (Blondeau, 2004, Pines, 2003)

Supekar (2007) did a study of the bird wing characteristics and created a biological inspired two-segmented telescopic wing. Structural and aerodynamic evaluations

were carried out however wind tunnel data were inconclusive due to a fabrication malfunction.

For low speed UAVs the advantages of the wings span increasing gives a dramatic improvement in the performance capabilities of the UAV; for example improvement of the rate of climb, range and endurance of the UAV. Nevertheless, the challenges faced by implementing wing span include the ability of the structure to resist bending under the loading due to large wing deflections, a weight penalty, actuator issues, and the energy required to drive the system. Due to an increase in the parasitic drag the telescoping wings have a lower aerodynamic efficiency (lift to drag ratio) than rigid fixed-wings (Pines, 2003).

2.3.2 Chord Length Change

The chord length of the wing in conventional aircraft is resized by means of leading or trailing edge flaps, which are usually moved by actuation systems. Many of these devices are patented and operational. Very few researchers exploited the resizing of the chord length without using such flaps or slats. An early example of chord extension is the flower flap (Day, 2011) used on fixed wing aircraft as illustrated in Figure 2-4. The flower flap slides back from the wing and rotate down creating a slot between it and the wing. The flap acts to increase the wing area and provide additional lift to the aircraft in comparison to traditional flap.

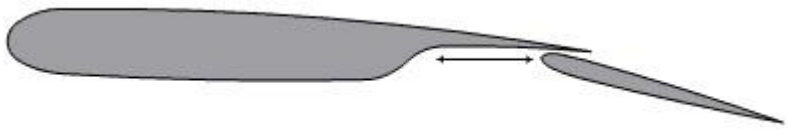

Figure 2-4 Illustration of a flower flap

Another example is the work of Reed et al., (2005). The internal structure of the wing consists of sliding rods and motor and lead screw assembly to drive the leading and trailing edge sections of the planform when actuated They used partial rib structures that could slide through a central slotted box and alter the chord wise position of the leading and trailing edges. The smooth operation of the lead and

screw mechanism under transverse aerodynamic loads is questionable. In addition, maintaining the chord-wise bending stiffness of the wing remained a challenge. The added weight and complexity of the design are other downsides of this work.

The application of smart materials, on the other hand, to achieve chord change is one of the least studied methods of wing morphing. One attempt is the work of researchers at cornerstone research group who experimented with dynamic modulus foam (DMF) to alter the chord length of wing (Perkins et al., 2004). The DMF foam is a lightweight form of shape memory polymer (SMP) with similar behaviour. The foam is highly stretchable at temperature above the glass transition temperature. Although their prototype wing section was extended along the chord upon heating it could not return to the original shape upon cooling, demonstrating the small recovery stress of shape memory foams. (Johnson, 2010) proposed a concept that composed of a lightweight bistable arch, SMA wires for actuation, a thin plate and support roller for the plate. This concept is expected to add little weight, but further no prototype was created. Further examination of smart materials to alter the wing chord length is an attractive research topic considering the importance of chord length of the aerodynamic behaviour of the wing, especially the induced drag.

2.3.3 Sweep Angle Variation

The concept of sweep change has been implemented in many successful and operational aircraft such as Bell X-5, F14 (Weisshaar, 2006). The method used to accomplish wing sweep is a complex pivoting mechanism on the wing. The wing sweep change is designed to change the wing configurations to suit the various flight conditions (Ma et al., 2004). For supersonic flight the Bell X-5 has small compact wings for high speed flights and one with larger area and span for take-off climb and cruising.

Calibration work between Hypercomp and NextGen Aeronautics have designed a wing that has flexible, stretchable skin panels attached to an articulated lattice structure with actuators in the joints. Thus, morphing is achieved through the adjustable framework to allow in-plane reconfiguration of highly flexible skins and

internal components that create wing area and span changes, including changing leading edge sweep to control aerodynamic drag. The variable geometry wing has the ability to move between five different wing planforms as illustrated Figure 2-5. The design incorporates wing planform changes in area, span, chord, and sweep that vary by 51%, 36%, 110% and 30 degrees, respectively (Weisshaar, 2006).

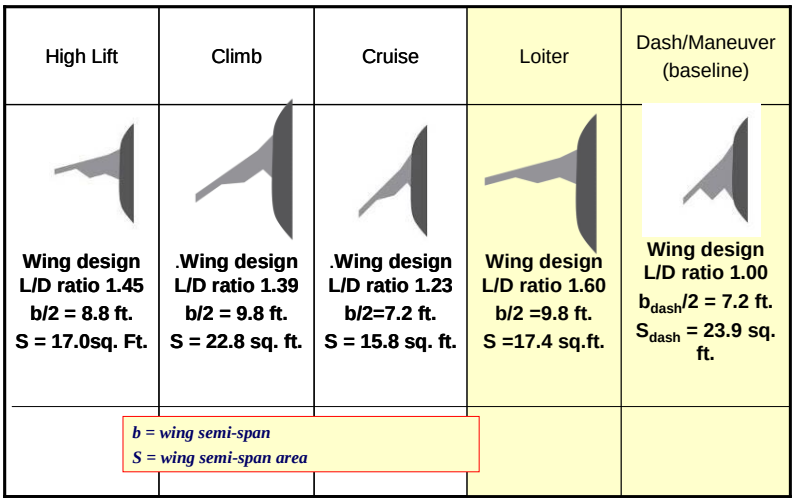

Figure 2-5 Morphing wing configurations for high-lift (Weisshaar, 2006)

On the other hand Mattioni (2008) successfully demonstrated the use of unsymmetrical laminated composites to realise a variable sweep wing for morphing UAV applications. Their numeric analysis identified the bifurcation point referred to as a snapping point at which the geometry changes. This confirms the possibility of eliminating mechanical joints to obtain different geometries. In their design, the wing spars are made of bi-stable composites. When a bending moment is applied on the spar, it causes the spar to snap to a second stable position around the bifurcation point which acts as a hinge. Therefore, the application of multistable composites simplify the complex mechanical systems required to modify the geometry of conventional wings (Friswell, 2011). However, the use of bi-stable composite materials may suffer from fatigue at the bifurcation point. Furthermore, the compliance of the wing skin may interfere with the snapping motion.

An increase of the sweep angle improves the aerodynamic performance at high speed regimes. Additionally, it significantly increases the flight envelope of an aircraft

originally designed for low speed flights. However it can be seen that the structural morphing is complex and made from heavy mechanisms composed of pivots. These pivots must bear bending and torsion loads; they tend to be heavy due to their thickness, reducing thus the overall effectiveness of the design especially when considering them for low speed flight. It is clear that several improvements are needed to reduce these disadvantages.

2.4 Out-Of-Plane Transformations

An alternative approach to modifying the aerodynamic characteristics of a wing is to alter the wing out of its original plane. Several researches have shown the potential of smart materials to accomplish the out-of-plane alternation of a morphing wing through camber change. This section presents the wing camber, chord, and twist controls.

2.4.1 Chord Wise Bending

Chord wise bending is a combination of camber and chord change. In the camber control approach, the adaptive airfoil can alter its camber to obtain the desired lift. This eliminates the need for conventional control surfaces. Experimental and computational results show a high promise for variable camber geometries (Kota et al., 2003). Camber change is performed either by the reconfiguration of the wing internal structure or the alternation of the wing skin. However, variable geometry airfoils such as the one developed for the Mission Adaptive Wing (MAW) (Powers et al., 1992) are complex structurally and consequently heavy and maintenance intensive. Recently, (Troy et al., 2012) has presented a framework for the practical implementation for piezo-ceramic actuators as camber displacement control. A comprehensive comparison of piezoelectic macro fibre composite actuators against a servo-actuated system have been carried out and have shown the morphing demonstrated superior response times (Osgar et al., 2013). Diaconu et al (Diaconu et al., 2007) intensively investigated the use of bi-stable or multi- stable structures as a morphing approach for the airfoil chord and camber changes. In Diaconu's design, such a bi-stable composite plate was embedded chord-wise and vertically in the airfoil cross section. This plate snapped from one stable position to another under

moments applied alternatively by actuators on the edges of the laminate. Thus, the chord-wise composite member controlled the airfoil camber, while the vertical element altered its chord length.

Furthermore, (Narcis et al., 2006) demonstrated that by using structures that are acting in the post-buckling regime, it is possible to obtain significant changes in shape with very modest changes in the applied load. Thus, by making use of non-linear structural responses, camber control of deformable airfoils can be achieved by using a carefully designed pre-loaded internal spinal structure. Such a structure is expected to move through the desired shape changes under the control of a single actuator. This actuator will deliver aerodynamic characteristics that match a set of pre-specified target shapes and also give improved aero-elastic properties.

(Sofla et al., 2004) developed a series of SMA-actuated flexural structures which could be used to deform wing sections. Their actuated structures were based on a concept called Antagonistic Flexural unit Cell (AFC). In this concept, a pair of one-way SMA actuators is placed at either side of a highly flexible unit core structure with large in-plane stiffness. The contraction of one SMA actuator upon heating results in the extension of the opposing SMA actuator mechanically. The contraction by heating of the now-extended actuator, later in the cycle, reverses the actuation.

High authority shape morphing beams can be made by the linear replication of the AFCs. Such actuated beams can be used to make reconfigurable wing boxes for shape morphing wing structures. Although the slow cooling rate of the SMA actuation is not appropriate for the flight control applications, the achievable aero-dynamic changes are still suitable for in-flight mission adaptation of the wing. The AFC based actuated structures are attractive for wing morphing applications because the distributed SMA actuators carry aerodynamic loads and therefore reduce the weight penalty. Additionally, the new wing shapes after the cooling of each SMA actuator are retained without requiring power. This can eventually result in saving fuel and increasing the aircraft endurance (Sofla et al., 2009). More recently (Galantai et al., 2012) has carried out a study the on novel designs to validate their suitability as viable wings for UAVs.

Figure 2-6 illustrates a wing section prototype that is capable of undergoing camber changes when actuated by antagonistic SMA actuators.

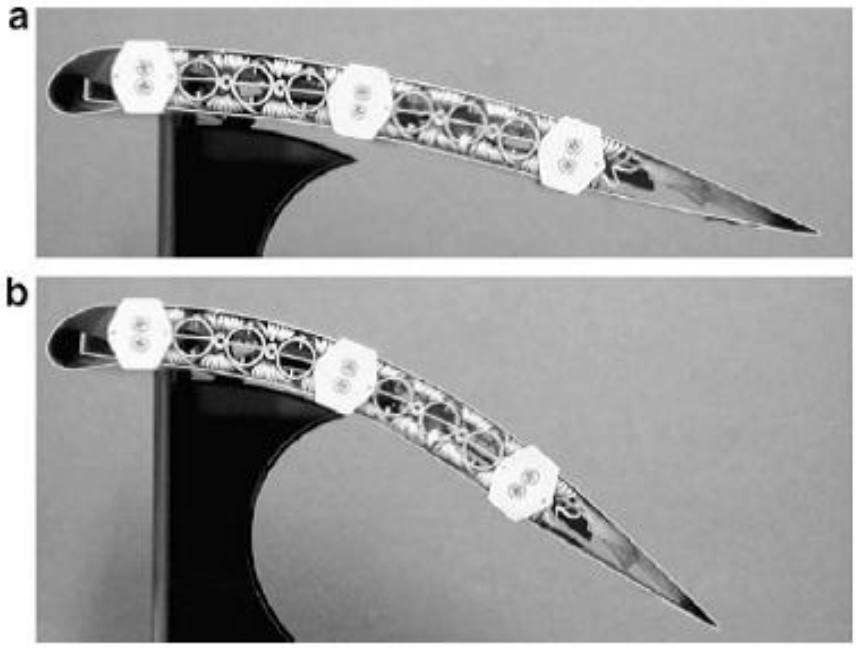

Figure 2-6 Chord-wise bending achieved by the heating of SMA strips in an antagonistic design. (a) Un-morphed and (b) morphed (Elzey DM 2003)

The development of smart materials has become the main focus of variable camber wing actuation technology today. Piezoelectric materials and Shape Memory Alloys have shown some possibilities to be used as actuators for deforming the wing profile.

2.4.2 Span Wise Bending

It was shown by NASA researchers that a hyper-elliptically swept planform wing with a cambered span, with a separate hyper-elliptical span wise profile, has aerodynamic advantage over flat wings (Lazos, 2005). Such a wing, referred to as Hyper-Elliptical Cambered Span (HECS), which inspired researchers to explore shape morphing wings capable of undergoing span camber. Wiggins et al studied the feasibility of a single-degree-of-freedom mechanism to morph a flat wing to a no-planar shape (Wiggins et al., 2004). Their scissor-like mechanism used a repeating quaternary-binary link configuration to transfer the motion of one linkage to the next. The mechanism is synthesised such that with only one input to the first linkage, in

the form of actuators displacement, the rest of the segments could adapt to the desired positions. Manzo and Garcia also investigated the shape morphing of HECS wing by using SMA tendons and DC actuators through a finger like approach(Manzo, 2006). They constructed a wing that could mimic an HECS profile by dividing the wing to five segments along the span. The main problem associated with their design was that the SMA had to be kept heated in order to carry aerodynamic loads.

2.4.3 Wing Twist Control

Morphing via variable twist, the wing is configured to optimise the twist angle to obtain low drag and high lift aerodynamic characteristics. Sofla et al (Sofla et al., 2009) reported that the gradual changes of the airfoil camber along the span can create a controllable twisting of the wing. In their design, an antagonistic wing was prototyped using shape memory alloy (SMA) actuators. An antagonistic structure is based on a pair of one-way SMA actuators as described under the chord wise bending section. Thus, the wing undergoes twisting by the asymmetric actuation of its SMA actuators.

In an alternative approach, (Abdulrahim et al., 2005) controlled the roll of a mini UAV by twisting its flexible wing. In their design, torque rods ran spanwise. These rods were rotated separately by two servo-motors mounted in the fuselage. Commanding a deflection of the servo induces the rods to rotate by acting against the wing leading edge. Their results for flight characteristics for the roll and spinning showed that the vehicle was easier to fly using morphing instead of the conventional rudder as lateral directional effector.

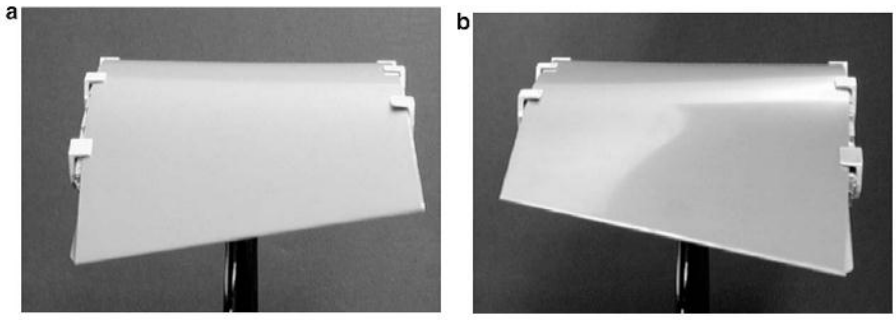

Figure 2-7 presents the twisting of a wing section using antagonistic SMA actuation (Elzey et al., 2003)

In Figure 2-7, twisting of a wing section achieved by antagonistic SMA actuation. (a) The left rib is flexed downward and right rib upward. (b) The left rib is actuated upward and the right one downward (Elzey et al., 2003).

Figure 2-8 illustrates the nominal wing and the morphed wing when each servo-motor is commanded to its equal but opposite value (Abdulrahim et al., 2005).

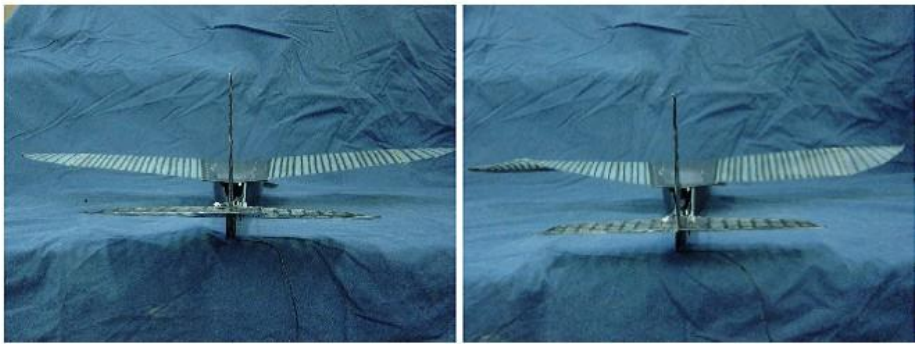

Figure 2-8 Nominal wing (left) and morphed wing (right) (Abdulrahim et al., 2005)

Moreover, adaptive aero-elastic structures offer potential solutions to achieve wing morphing through out-of-plane transformation. This approach uses the aerodynamic forces acting upon the wing to provide the necessary forces and moments to bend and twist the wing.

2.5 Airfoil Profile Adjustments

An airfoil significantly influences the aerodynamic characteristics of any aircraft. The airfoil profile adjustment is classed as altering the aerodynamic characteristics of a wing by reshaping the wings profile with no significant change to its camber. By tailoring the shape of the airfoil, the aircraft efficiency can be modified by tuning an

optimum airfoil configuration. Thus, if an airfoil section can be changed accordingly with the change in flight conditions, benefits may result that include the improvements of the Mach number, aerodynamic efficiency, aerodynamic performances such as the range, endurance, and the expansion of the flight envelope. Austin et al (Austin et al., 1994) developed a theoretical method which was experimentally validated. Their purpose was to control the static shape of flexible structures by employing internal translational actuators. In their design, 14 linear actuators were attached diagonally to form a wing rib structure. The diagonal elements are translational actuators that expand and contract to deform the airfoil. A prototype of the adaptive rib with the actuators was constructed to demonstrate the shape- control concept.

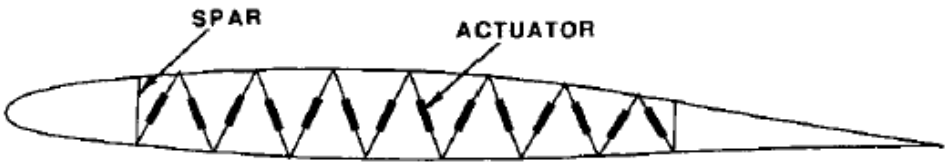

Figure 2-9 Airfoil profile control (Austin et al., 1994)

(Dong et al., 2008) designed and manufactured a changeable airfoil model using SMA springs between the wing skin and its supporting wing-box. Therefore, by changing the constraint condition of the skins, they can achieve large deformation without over- stepping their strain allowance. Shape memory alloy springs with the help of stop structures were used to actuate accurately certain points on the skins to approach the target airfoil. The wing-box consisted of rigid steel ribs and spars. The covering skin was allowed to slide over a cushion at the leading edge spar as illustrated by Figure 2-9. Cushions were used in order to avoid dislocation between the skins which were level with that of the tailing edge box. The resizing of the SMA spring length upon heating and cooling could alter the wing thickness.

2.6 Boundary Layer Local Deformation: Active Flow Control

The field of flow control using actuators to force the flow has witnessed explosive growth recently because of the ubiquitous nature of fluids in engineering systems, the community's improved understanding of fluid mechanics and the potential to

dramatically improve system performance using effective control strategies. However, the number of instances in which flow control has successfully transitioned from a prototype to a real-world aeronautical application is small (e.g., (Pugliese and Englar, 1979, Nagib et al., 2004, Shaw et al., 2006)).

The aerodynamic characteristics of low Reynolds number flows are typically vastly different than those normally seen in typical aerodynamic and aerospace applications. Slight changes in the flow speed can have large effects on the flow over a given airfoil, most notably severe changes in lift to drag ratio. An improvement of the lift to drag ratio can greatly benefit UAVs (Santhanakrishnan et al., 2005).

The key concept of boundary layer flow control is avoiding flow separation which affects the lift and drag. Figure 2-9 (English et al., 2010) is a schematic diagram of the aerodynamic flow control using fluidic actuators. The upper figure shows flow separation and loss of lift at a high angle attack. While the bottom figure shows apparent surface modification of the flow leading to flow reattachment and recovery of lift.

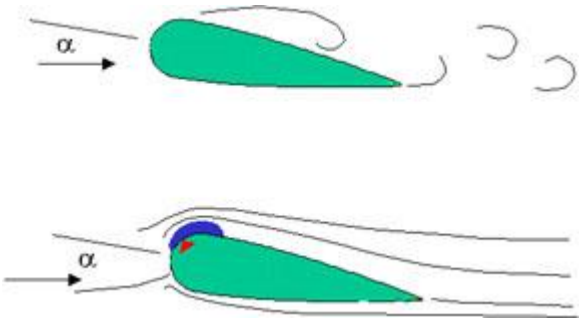

Figure 2-10 Flow separation modification (English et al., 2010)

Flow control devices can be classed as two types *passive* and *active*. Passive devices are fixed alterations on the surface of a body in a flow. Some examples of these devices are vortex generators, chevrons, fences, dimples, and riblets (Bonnet and Anthoine, 2009). While these devices improve flow characteristics, they are point-design devices; therefore, when the aircraft is in off-design flight conditions, the devices are still on the surface in the external flow and may induce adverse effects.

A later development in engineering research and development is active flow control devices. These devices have the unique ability to operate in a range of conditions and when needed to improve flow characteristics. Some examples of these devices are trailing edge flaps, blown flaps, suction or blowing through orifices, thermal riblets, synthetic jets, electrostatic and plasma interactions with flows, acoustic cavities or forcing, surface deformation, and rapid transverse strain (Joslin and Miller, 2009).

2.6.1 Fluid Injection/Suction

Synthetic jet actuators (SJAs) have emerged as an adaptable actuator for active flow control having a great potential of active control of boundary layer separation in order to reduce the drag and increase the efficiency of aerodynamic devices (Amitay et al., 2001, Gilarranz et al., 2005a, Gilarranz et al., 2005b, Glezer and Amitay, 2002). Using SJAs to control flow separation was considered as the enabling means for the next-generation of UAVs and advance air mobility systems (Pilon, 2004). Most recently wind tunnel tests have been carried out on a hump with embedded synthetic jets showing a positive effect on the decrease of the loss coefficient in the region of the measured velocities, especially at the lower velocities (Pick et al., 2013).

The synthetic jet concept consists of an exit orifice, an enclosed chamber and a method to change the pressure within the chamber so air is forced into and out of the chamber through the orifice or slot. Figure 2-11 shows the synthetic jet concept which consists of three elementary components an oscillating diaphragm, a slit or a round orifice and a cylindrical or rectangular cavity (Holman et al., 2005). The motor provides electrical to mechanical conversion and the mechanical to fluid interface transforms the mechanical energy into air flow. It is an autonomous and simple device requiring no heavy and intricate support systems (air supplies, clutter of hydraulic piping and connectors) for its operation.

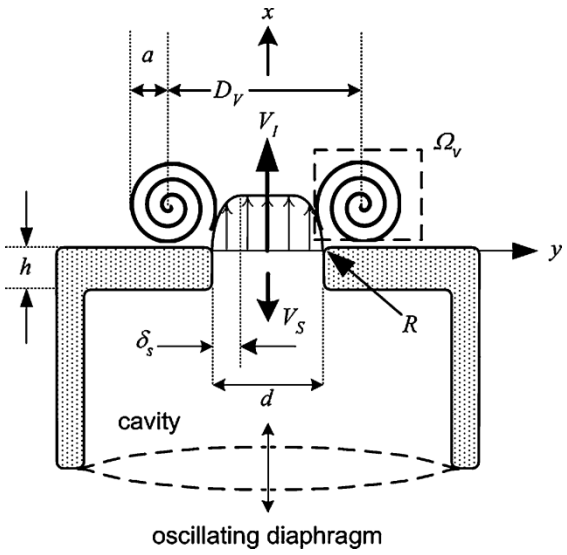

Figure 2-11 synthetic jet actuator (Holman et al., 2005)

The use of synthetic jets to control flow separation in a boundary layer is based on the idea of accelerating the transition from laminar to turbulence which is more capable of resisting laminar separation. In the most recent publication, Gilarranz et al reported their work on developing a high-power synthetic jet actuator which acted as a reciprocating air compressor with a crank system and six pistons (Gilarranz et al., 2005a). The maximum power consumption of this synthetic jet actuator was 1200W and the peak jet velocity was 124 m/s. They also reported the application of this newly developed synthetic jet actuator to flow separation control over a NACA 0015 wing in conditions with a free stream velocity of 35m/s and a Reynolds number of 8.96×10^5. Their results showed that the synthetic jet actuation successfully decreased the drag and increased the maximum lift coefficient by 80% when the angle of attack was varied from 12 to 18 degree (Gilarranz et al., 2005b). Georgia Tech demonstrated the success of synthetic jet actuators for flow separation control on a low speed, 50 degree swept wing UAV (Parekh et al., 2003, Washburn and Amitay, 2004). By applying separation control to one or the other wing, significant roll moments were achieved at angles of attack above 15 degrees. Researchers at University of Bath in the United Kingdom have looked into using synthetic jets for propulsion and enhanced aerodynamics of Micro Air Vehicles (Whitehead J., 2003).

Electrodynamic synthetic jets are attractive for low-frequency applications because of their large displacement capability, but their increased weight (due to the magnet

assembly) and heat transfer (due to heating in the resistive coil) present design challenges (Nagib et al., 2004, McCormick, 2000, Agashe et al., 2009).

2.6.2 Moving Object/Surface

Moving surface actuators can take various forms, but the most common are the piezoelectric composite flaps, electroactive dimples and balloon actuators. These are summarised below.

The piezoelectric flap actuator has been used successfully in a variety of applications, including control of separation (Seifert et al., 1998), turbulent boundary layer streaks (Jacobson and Reynolds, 1998, Jeon and Blackwelder, 2000) flow-induced cavity oscillations (Raman G, 2002, Kegerise et al., 2007a, Kegerise et al., 2007b). A cantilever composite beam configuration is commonly used. The actuator can introduce spanwise or streamwise vertical perturbations into the flow depending on the geometry and orientation of the vibrating tip with respect to the local free-stream flow (Cattafesta and Sheplak, 2011). Application of an ac voltage across the piezoceramic causes the beam to vibrate, which then interacts with the flow as illustrated in Figure 2-12. Composite beam modelling is treated in (Cattafesta et al., 2001) and an extension to a bimorph is presented in (Mathew et al., 2006).

Figure 2-12 Sample applications of piezoelectric flap actuators (Cattafesta and Sheplak, 2011)

Recent progress has been made in the micro fabrication of electroactive polymer dimples for the control of turbulent boundary layers (Arthur et al., 2006, Dearing et al., 2007). A dimple consists of an elastomer sandwiched between compliant electrodes as shown in Figure 2-13. Upon application of a voltage, an effective

mechanical pressure is produced. The induced strain in the thickness direction produces lateral expansion. The lateral strain is constrained at the boundary, which leads to out-of-plane buckling. The dimples thus produce unsteady surface depressions that interact with the near-wall turbulent structures.

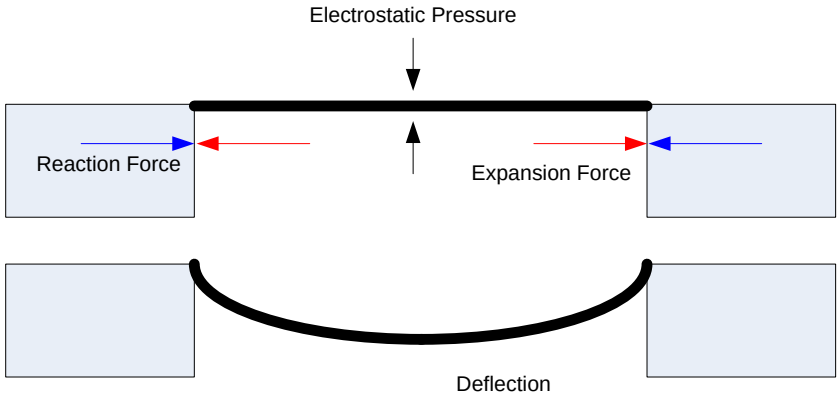

Figure 2-13 Principle operation of a dimple

Research is focusing on understanding and predicting the behaviour of the micro fabricated dimples and ultimately designing devices with the desired size, gain, and bandwidth requirements (Dearing et al., 2007).

(Raney et al., 2004, Raney et al., 2000) examined the use of distributed shape-change effector arrays for flight control on a UAV. The distributed shape-change effector arrays were modelled as a series of bumps normal to the aircraft surface which could be deployed to generate control moments as illustrated in Figure 2-14.

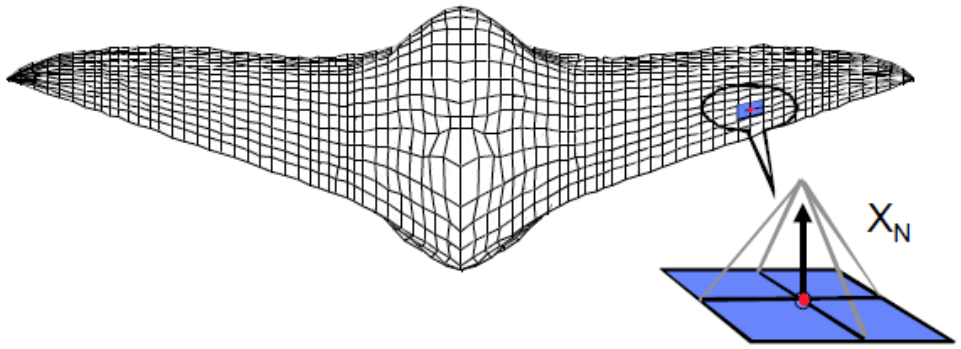

Figure 2-14 Shape-change device modelled as deflection of grid point along normal vector (David L. Raney 2000)

Analysis was done to find the favourable locations for the placement of the shape-change device arrays on UAV. Each morphing device was in an array which were either completely on or off. To produce a larger force as required the devices are turned on. The simulation results indicate that the effector suite possessed sufficient authority to stabilise and manoeuvre the example vehicle model, executing relatively low-rate rolling manoeuvres at 10 degrees per second. When substantial atmospheric disturbances were included in the simulation the device arrays did not possess sufficient authority to maintain stability of the vehicle's lateral directional.

A new type of flexible balloon actuator for active flow control has been developed with structural flexibility and perfect air-tightness even with internal high pressure gas. The balloon actuator inflates a spine-on elastic membrane by using an external gas flow as show in Figure 2-15 (Lv et al., 2012). When the balloon actuator is at rest, the top surface of the actuator matches with the surface of the airfoil. When the balloon actuator is actuated, the elastic membrane is inflated, thereby creating asymmetry on the aerodynamic body, resulting in control of the flow.

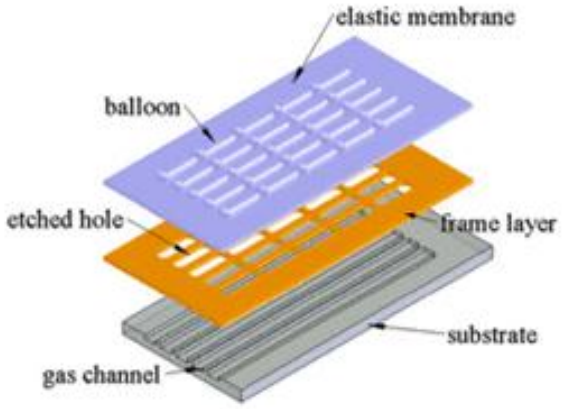

Figure 2-15 Structure of a balloon actuator (Lv et al., 2012)

The results show that the actuators can dramatically alter the flow field within the boundary layer. Flight test carried out show that the inflated balloon actuators lead to local flow separation, but due to the imbalance of localised pressure on the airfoil an induced rolling moment and the rolling angle of the UAV is changed by about 30°.

2.6.3 Plasma

Plasma actuators are becoming increasingly popular because they have no moving parts and have rapid time response and low mass. A recent extensive review on plasma devices and their applications have been carried out (Corke et al., 2007, Corke et al., 2010, Moreau, 2007). Followed by a comprehensive discussion on their efficiency and performance (Kriegseis et al., 2012).

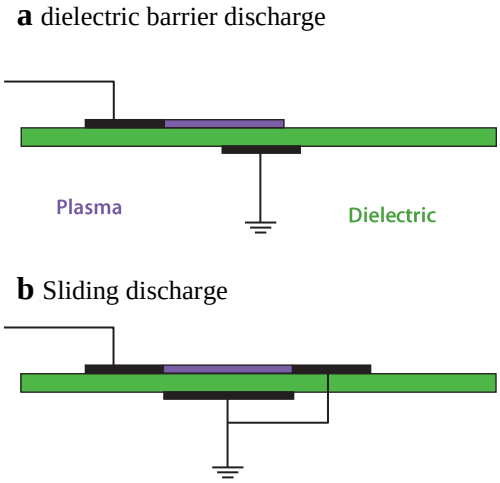

Figure 2-16 Schematics of two common plasma actuators: (a) dielectric barrier discharge (DBD), and (b) sliding discharge (Cattafesta and Sheplak, 2011)

Single dielectric barrier discharge actuators. As shown in Figure 2-16 (Cattafesta and Sheplak, 2011), an SDBD actuator consists of an asymmetric pair of electrodes separated by a dielectric material. A high-voltage ac waveform is supplied to the exposed electrode, which results in an asymmetric electric field that ionizes air molecules to form a cold plasma in which only a small fraction of air molecules are ionized. The accelerated charged particles transfer momentum to the surrounding gas adjacent to the surface via collisions with neutral particles. Considerable effort has gone into maximising the performance of SDBD actuators (Corke et al., 2010, Forte et al., 2007, Jolibois and Moreau, 2009, Thomas et al., 2009). Researchers have optimised performance via parametric studies of voltage amplitude, frequency, waveform, slew rate, dielectric material and thickness, electrode geometry, multiple actuator arrays, and even the use of a plasma synthetic jet (Santhanakrishnan and Jacob, 2007). A general recommendation is to use thicker dielectrics (several millimetres) with low dielectric constant for improved efficiency.

Collectively, these efforts suggest that other approaches are required to significantly increase performance. Options include multiple barrier (Benard et al., 2009, Durscher R, 2010) and sliding discharge actuators (Corke et al., 2010, Moreau et al., 2008), and local arc filament actuators (Samimy et al., 2004, Utkin et al., 2007). (Benard et al., 2009) describe a multiple dielectric barrier device in which the third electrode acts as a shield between two successive DBDs, resulting in a near-constant electric wind velocity above the multi-DBD actuator. (Narayanaswamy et al., 2010) have designed a pulsed-plasma synthetic or sparkjet generated via an electrical discharge in a small cavity. Their device generates peak velocities of approximately 250 meters per second at frequencies up to 5 kHz.

2.7 Morphing Concept Suitable for X-RAE1 UAV

The field of shape morphing aircraft has attracted the attention of hundreds of research groups during the past century and with a significant increase in the last decade due to the advances in material fabrication. Although many interesting concepts have been synthesised, only a handful of such reconfigurable planes have been ever produced of which were for supersonic flight. This chapter has presented the importance of low speed UAV morphing and a critical review of current research advances. In the range of low speed, small aircraft no commercial product exists. Although several conceptual designs of small or low speed aircraft have made it to the wind tunnel testing stage, only very limited number of such shape morphing prototypes have ever been fabricated or flight tested. Shape morphing has been shown to be beneficial and produce a vast improvement in performance for low speed UAVs, but complexities arise with using shape morphing. One key fundamental effect is the weight increase, which has an adverse effect on performance.

Compared to supersonic aircraft, the small or low speed planes require more dramatic wing variations for a noticeable and practical change in their aerodynamic properties. This points us to the complexity of the development of low speed UAV, which is the large weight penalty for an addition of actuation systems capable of causing wing variations to the overall allowed weight. To address the above

challenge, any successful conceptual design for shape morphing of low speed/small aircraft should:

- Undergo large geometry change
- Use smart materials for actuation
- Use the smart material actuators for supporting part of the aerodynamic loads
- Have integrated and distributed actuators to avoid transmission mechanisms
- Use advance light weight composites for the fixed structure and the skin.

By reviewing wing morphing concepts the use of smart materials for low speed UAVs can be seen as most desirable solution. With the vast variety of smart materials it can be concluded that the most used types of smart material for low speed UAVs are shape memory alloys followed by piezoelectric materials. A list of the most common smart material types, in descending order and the type of stimulus required to affect the smart material is listed in Table 2-2.

Smart Material	**Stimulus**
Shape-memory alloys	Thermal
Piezoelectric	Electrical
Magnetostrictive	Magnetic
Electrorestrictive	Electrical

Table 2-2 Order of used smart materials for low speed UAVs

The concept of flow control uses smart materials which are made of light weight composites such as shape memory alloys. The key concept of flow control is to affect the flow-field round the UAV which has an impact on the aerodynamics and in turn can be used to reduce drug or produce a control force. The geometry change provided by a single flow control devices is considered small but when combined into an array of devices as a skin round the UAV all working synchronously together they will have a greater effect. By applying CFD analysis an investigation of the effect an embedded smart effector array on a UAV will be carried out. The UAV X-RAE1 (Trebble, 1985a) will be used as a test bed for this research due to its classification as a low speed UAV. The full specification of the X-RAE1 can be found in the appendices.

2.8 Summary

A review of wing morphing technologies that can be applied to low speed UAVs has been critically analysed and classified into four major types. These being planform alternation, airfoil adjustment, out of plane transformation and boundary layer local deformations. Due to the characteristics of boundary layer local deformations it has been selected as the type of wing morphing technique to be investigated on an experimental UAV X-RAE1. One major contribution for the selection of boundary layer local deformations i.e. flow control is the use of smart materials for actuation to control the flow round the UAV by impacting on the aerodynamics properties of the wing and in turn increasing the lift force or reducing the drag. The weight penalty for using smart materials for actuation is assumed to be considerably lower compared to conventional actuation systems.

CHAPTER

3

Aircraft Mechanics Review

This Chapter gives a general outline of aircraft motion, control surfaces and airfoil geometry followed by a brief presentation of the derivation of the equations of motion and their linearisation to be implemented for the X-RAE1 UAV.

3.1 Flight Vehicle Motions

Objects are defined by three spatial dimensions and one time dimension, moving in two ways. An object translates, or changes location, from one point to another and an object rotates, or changes its altitude. In general, the motion of any object involves both translation and rotation. The translations are in direct response to external forces. The rotations are in direct response to external torques or moments.

The motion of an aircraft is particularly complex because the rotations and translations are coupled together; a rotation affects the magnitude and direction of the forces which affect translations.

The motion of an aircraft can be summarised by three translational motions and three rotational motions as shown in Figure 3-1. The translational motions are forward and backward translation across the longitudinal axis (*x*-axis), left and right translation across the lateral axis (*y*- axis), up and down translation across the vertical axis (*z*-axis) with the direction of the arrows indicating positive motion in each of the axis respectively.

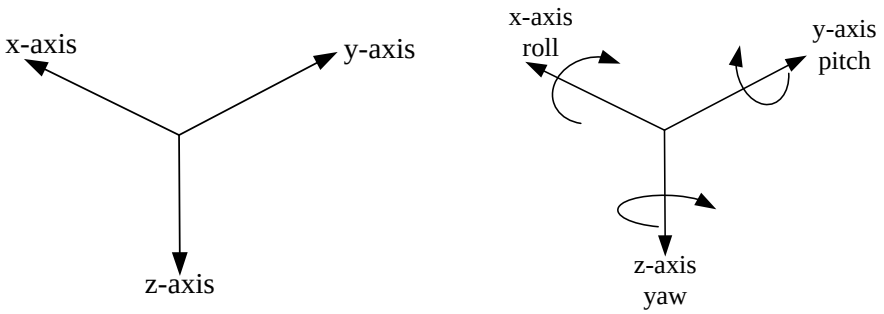

Figure 3-1 The three translational movements and the three rotational motions

The three rotational motions are *pitch*, *roll* and *yaw*. Pitch is a rotational motion in which the aircraft turns around its lateral axis (*y*-axis) by raising or lowering the nose of the aircraft. The angle in which the aircraft pitches is called the *pitch angle* given by the symbol θ. A positive pitch angle is when the aircraft nose pitches up. Roll is a rotational motion in which the aircraft turns around its longitudinal axis (*x*-axis) by raising one wing higher as the other wing dips lower. The angle in which the aircraft rolls is called the roll angle given by the symbol ϕ. A positive roll angle is when the aircraft rolls to the right, i.e. the right wing of the aircraft points downwards. Yaw is a rotational motion in which the aircraft turns around its vertical axis (*z*-axis) by moving the nose of the aircraft to the pilot's left or right. The angle in which the aircraft yaws is called the yaw angle given by the symbol ψ. A positive yaw angle is when the aircraft yaws to the right, i.e. the nose of the aircraft points to the right.

3.2 Aircraft Reference Geometry

The description of the geometric layout of an aircraft is an essential part of the mathematical modelling process. It is convenient to divide the aircraft geometry into a set of non-dimensional reference parameters (McCormick, 1995). These are defined and illustrated in Figure 3-2 below.

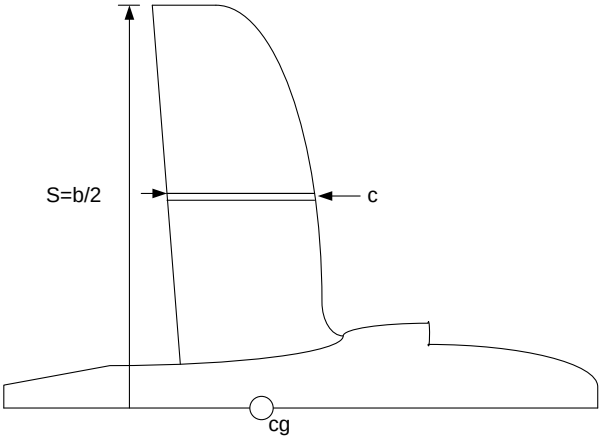

Figure 3-2 Reference Geometry

S is the reference area of the gross plan area of the wing, including that part within the fuselage and is denoted $S = bc$. Where b is the wing span and c is the standard mean chord of the wing. The aspect ratio of the aircraft wing is a measure of its spanwise slenderness and is denoted A and is defined as b/c. The centre of gravity cg of an aircraft is usually located on the reference chord. Its position is a fraction of c; the cg for the X-RAE1 is located 0.34c from the leading edge which is 0.121 meters.

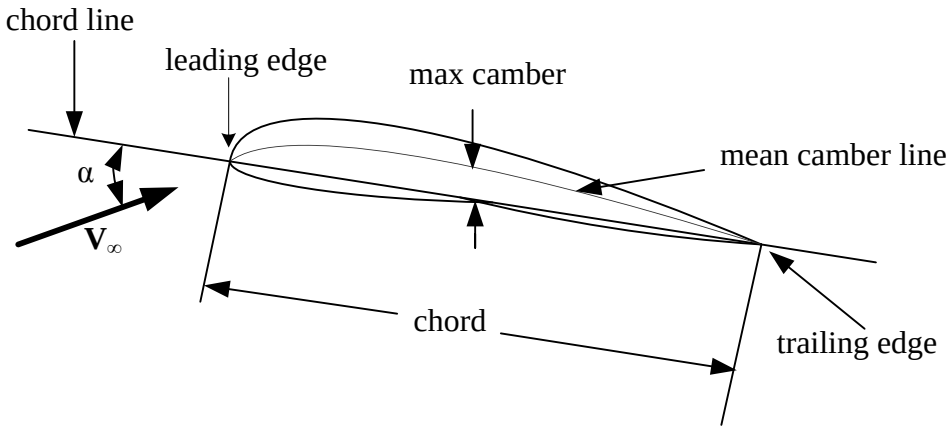

Figure 3-3 Airfoil Cross-Section

A labelled cross-sectional view of airfoil is shown in Figure 3-3 (Yechout and Morris, 2003). The common definitions of airfoil geometry are:

1. A straight line, passing through the leading and trailing edge, is called the *chord line*. The straight line distance between the leading and trailing edge is the *chord*.
2. The *mean camber* line is the locus of points halfway between the upper and lower surfaces, as measured perpendicular to the mean camber line itself.
3. The *max camber* is the maximum distance between the mean camber line and the chord line, as measured perpendicular to the chord line.
4. The *thickness* is the distance between the upper surface and lower surface, as measured perpendicular to the mean camber line.
5. The *angle of attack* alpha (α) is the angle between the chord line and the free stream velocity $\mathbf{V}_{\infty}$.
6. *Dihedral angle* is the angle that the wing makes with the local horizontal.
7. *Downwash* is the pressure differences across the wing surfaces causing spoilage around the wing tips. This causes a local induced angle of attack which reduces lift.

3.3 Aircraft Control Surfaces

Flight vehicles use control surfaces for stabilisation and manoeuvrability. The main control surfaces of an aircraft are illustrated in Figure 3-4. The *starboard* side of the flight vehicle is the right side (Hull, 2007).

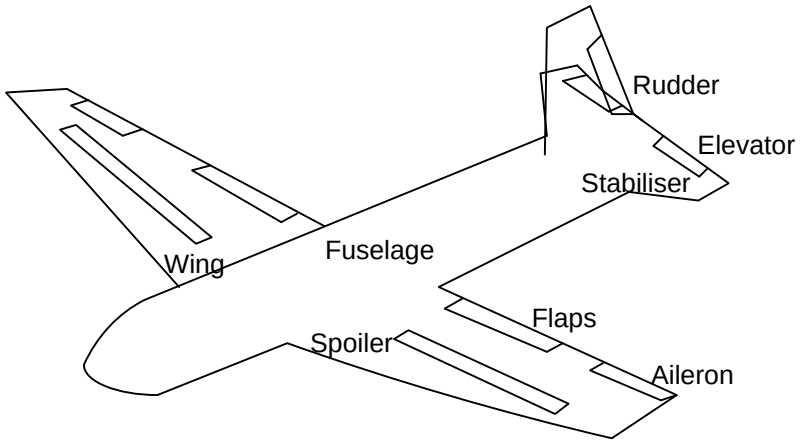

Figure 3-4 Aircraft control surfaces

The tail of the aircraft is made from a *horizontal stabiliser* and a *vertical stabiliser*. The vertical stabiliser is a fixed wing section that provides stability to the plane preventing pitching. Connected to the horizontal stabiliser are two *elevators*. The elevators work in pairs and are used to control the position of the nose of the aircraft, which simultaneously controls the angle of attack. When the elevator is down it produces more lift make the aircraft pitch down.

The vertical stabiliser controls the direction of flight making the plane fly straight, by preventing yaw motion of the nose. Part of vertical stabiliser is the *rudder* which allows the pilot to control the yaw. When the rudder is moved to the left there is a side force pushing to the right of the rudder making the nose yaw to the left.

The control surfaces attached to the wing are the *ailerons*, *flaps* and *spoilers*. The ailerons produce a rolling motion which allows the plane to turn. They are small hinged sections on the outboard portion of the wing. When the right aileron is deflected up the left aileron deflects down. This makes the plane bank to the right, one wing goes up and the other down. The flaps increase the area of the wing and the camber of the airfoil. This allows the plane to get off the ground more quickly and land more slowly. The spoilers also help with the landing and open upwards increasing drag to help the aircraft to stop.

Sign conventions have been created to describe the positive deflection of the control surfaces. The three control deflections are listed below:

1. Positive elevator deflection (η) is trailing edge down. It will typically produce a negative (nose down) pitching moment.
2. Positive aileron deflection (ξ) is trailing edge down on either aileron.
3. Positive rudder deflection (ζ) is trailing edge left. Will typically result in a negative (nose left) yawing moment.

3.4 Rigid Aircraft Equations of Motion

The equations of motion of a rigid body and the assumptions upon which they are based are briefly presented in this section. Suitable systems of axes for the following analysis are defined and the process of converting from one system to another with different orientation is set forth using Euler angles. Finally, the general origin of the forces and moments acting on a flying vehicle is discussed and they are incorporated within the equations of motion. This is based on standard text books such as (Babister, 1980, Blakelock, 1991, Cook, 2007, Etkin and Reid, 1996, Stengel, 2004).

Aircraft equations of motion are obtained by applying Newton's 2nd law to a rigid aircraft. Newton's 2nd law states that the summation of the applied forces acting on the aircraft is equal to the time rate of change of linear momentum and the summation of the applied moments acting on the aircraft is equal to the time rate of change of angular momentum.

3.4.1 Assumptions

When deriving the equations of motion of an aircraft the following restrictive assumptions are made to help derive the equations.

1. The body is assumed to be rigid during the motions considered. Any deformations of the structure are not taken into account neither the dynamics of any moving element with respect to the airframe apart from the static deflection characteristics of the control surfaces.
2. The mass of the body and the mass distribution is assumed to be constant during the time-interval in which its motions are studied. Therefore, the motion of the aircraft can be described by a translation of its centre of gravity and the rotation about it.
3. The earth is assumed to be fixed in space, i.e. its rotation is neglected and the curvature of the Earth is neglected.
4. The aircraft has a plane of symmetry
5. The atmosphere is assumed still and not moving with respect to earth.

3.4.2 Aircraft Axis Systems

There are three axis systems which will be used to develop the equations of motion. These are the *body axis* system fixed to the aircraft, the *earth axis* system, which will be assumed to be an inertial axis system fixed to the earth, and the *stability axis* system, which is a body fixed system defined with respect to the relative wind. Each of these systems is useful as they provide a convenient system for defining a particular vector, such as, the aerodynamic forces, the weight vector, or the thrust vector.

Based on the above mentioned assumptions suitable reference frames can be defined where Newton's laws can be applied.

- *Earth-fixed axes:* The earth axis system is a right-handed orthogonal system which is considered to be fixed in space. The z_E-axis points downwards, parallel to the local direction of gravity. The x_E-axis is directed to the north, the y_E-axis to the east.

- *Body-fixed axes:* This is a right-handed orthogonal reference system which has its origin O_B in the centre of gravity of the aircraft. The $x_B O_B z_B$ plane coincides with the aircraft's plane of symmetry. The x_B-axis is directed toward the nose of the aircraft, the y_B-axis points to the right wing ('starboard'), and the z_B-axis points toward the bottom of the aircraft Figure 3-5.

- *Stability axes:* The stability axis system is rotated relative to the body axis system through the angle of attack. The *x* axis points in the direction of the projection of the relative wind onto the *xz* plane of the aircraft. The origin is at the aircraft centre of gravity. The *y* axis is out the right wing and coincident with the *y* axis of the body axis system. The *z* axis is orthogonal and points downward in accordance with the right-hand rule.

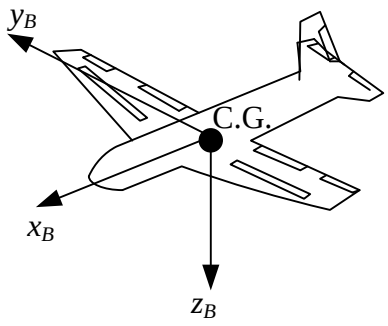

Figure 3-5 body fixed axes

3.4.3 Relationship between the Systems of Axes

The orientation of one system of axes with respect to another one needs to be defined. As most of the analysis is limited to perturbations about straight symmetric flight, the Euler angles are considered as the most appropriate for this purpose. It can be proved that three angular displacements Ψ Θ Φ in that order are necessary and sufficient to give the relative orientation of any two systems of axes, as seen in Figure 3-6 (Abzug and Larrabee, 2005). In flight mechanics literature, the Euler angles are usually referred to as:

Ψ *: yaw angle*
Θ *: pitch angle*
Φ *: roll angle*

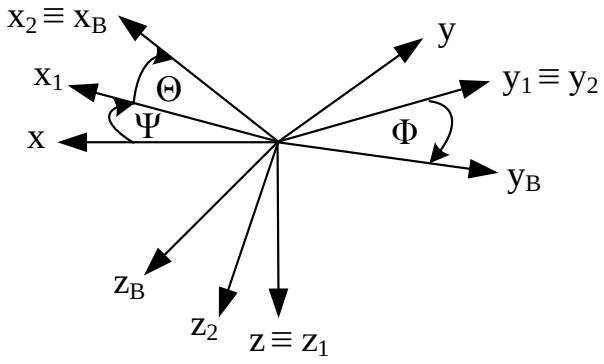

Figure 3-6 Euler angles

The components of any vector along the axes of displaced system can be determined if the Euler transformation ($\mathbf{R}_{ELR}$) is applied to its components with reference to the initial system, where $\mathbf{R}_{ELR}$ is the orthogonal transformation given bellow (Yechout and Morris, 2003):

$$\mathbf{R}_{ELR} = \begin{pmatrix} \cos\psi\cos\theta & \sin\psi\cos\theta & -\sin\theta \\ \cos\psi\sin\theta\sin\phi - \sin\psi\cos\phi & \sin\psi\sin\theta\sin\phi + \cos\psi\cos\phi & \cos\theta\sin\phi \\ \cos\psi\sin\theta\cos\phi + \sin\psi\sin\phi & \sin\psi\sin\theta\cos\phi - \cos\psi\sin\phi & \cos\theta\cos\phi \end{pmatrix} \quad (3.1)$$

Figure 3-7 shows the relationship between the axes systems, the Euler angles are used to rotate the aircraft earth axis system into coincide with the body axis system. The Stability axis to body axes is accomplished by rotating the stability axis system through a positive angle of attack α .

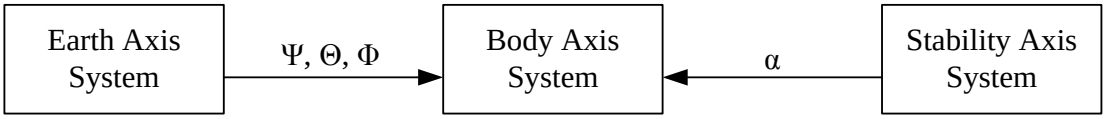

Figure 3-7 Axis Systems Euler Transformations

3.4.4 Aircraft Force Equations

The generalised equations of motion derived from first principles (Cook, 2007, Yechout and Morris, 2003). The formulation of the aerodynamic, gravitational and thrust moments and forces are presented in the following section.

Newton's 2nd law states that the time rate of change of linear momentum is equal to the summation of the applied forces acting on the aircraft centre of gravity.

$$\left[\frac{d(mv)}{dt}\right]_{inertial} = \mathbf{F} \quad (3.2)$$

While Newton's 2nd law is only valid with respect to an inertial reference frame, the equations can be expressed in the body axis system. If the equations are expressed in the body axis system, the fact that a system is rotating with respect to an inertial reference frame must be taken into account, this is accomplished using Equation 2.3 which shows how the rate of change of a vector **a** in an inertial system is related to the rate of change of **a** in a body fixed system.

$$\dot{\mathbf{a}}_{Inertial} = \dot{\mathbf{a}}_{Body} + \mathbf{\Omega}_{Body} \times \mathbf{a}_{Body} \tag{3.3}$$

The velocity vector in the body axis system $\mathbf{V_T}$ is defined as:

$$\mathbf{V_T} = U\mathbf{i} + V\mathbf{j} + W\mathbf{k} \tag{3.4}$$

where *U, V, W* are the coordinates of $\mathbf{V_T}$ with respect to the body axes respectively. Also the aircraft angular rate in the body axis system $\mathbf{\Omega}$ is defined as:

$$\mathbf{\Omega} = P\mathbf{i} + Q\mathbf{j} + R\mathbf{k} \tag{3.5}$$

where *P, Q, R* are the roll, pitch, and yaw rates respectively expressed in the body axis. Then applying Equation 2.3 for the rate of change of $\mathbf{V_T}$ we have:

$$\begin{bmatrix} \dot{U} \\ \dot{V} \\ \dot{W} \end{bmatrix}_{inertial} = \begin{bmatrix} \dot{U} \\ \dot{V} \\ \dot{W} \end{bmatrix}_{Body} + \begin{vmatrix} \mathbf{i} & \mathbf{j} & \mathbf{k} \\ P & Q & R \\ U & V & W \end{vmatrix}_{Body} \tag{3.6}$$

By multiplying the inertial acceleration in the body axis system by the mass of the aircraft yields the following three force equations:

$$\begin{aligned} m(\dot{U} + QW - RV) &= F_x \\ m(\dot{V} + RU - PW) &= F_y \\ m(\dot{W} + PV - QU) &= F_z \end{aligned} \tag{3.7}$$

3.4.5 Aircraft Moment Equations

The three moment equations are determined by applying Newton's 2nd law in a manner similar to the three force equations. Newton's 2nd law states that the time rate of change of angular momentum of the aircraft is equal to the applied moments acting on the aircraft. **H** is the angular momentum of the aircraft and has the following components:

$$\begin{aligned} H_x &= PI_x - QI_{xy} - RI_{xz} \\ H_y &= QI_y - RI_{yz} - PI_{xy} \\ H_z &= RI_z - PI_{xz} - QI_{yz} \end{aligned} \tag{3.8}$$

where I_x, I_y and I_z are the moments of inertia about the corresponding body axes and I_{xy}, I_{yz} and I_{xz} are the products of inertia. As the aircraft has the *xz* plane as a plane of symmetry $I_{xy} = I_{yz} = 0$. By applying Equation 3.3 for the rate of change of the angular momentum **H** we have the following relationship.

$$\left[\frac{d\mathbf{H}}{dt}\right]_{Inertial} = \left[\frac{d\mathbf{H}}{dt}\right]_{Body} + \mathbf{\Omega}_{Body} \times \mathbf{H}_{Body} \tag{3.9}$$

This gives the three moment equations of motion in the body axis system, where the left hand side represents the response of the aircraft and the right-hand side consists of the applied moments.

$$\begin{aligned} \dot{P}I_x - \dot{R}I_{xz} + QR(I_z - I_y) - PQI_{xz} &= L_A = L \\ \dot{Q}I_y + PR(I_x - I_z) + (P^2 - R^2)I_{xz} &= M_A + M_T = M \\ \dot{R}I_z - \dot{P}I_{xz} + PQ(I_y - I_x) + QRI_{xz} &= N_A = N \end{aligned} \tag{3.10}$$

The applied moments consist of the aerodynamic and thrust rolling, pitching, and yawing moments, L_A, M_A, N_A and M_T. There are no moments due to gravity because the weight vector acts through the centre of gravity and the moment arms are zero. Any moments because of rotating masses (such as jet engines) on or within the aircraft have been neglected.

3.4.6 External Forces and Moments

The external forces and moments are generally:

1. Gravity forces and moments
2. Aerodynamic forces and moments
3. Thrust forces and moments

Gravity Forces and Moments

The gravity forces can be evaluated by the projection of the gravitational acceleration *g* along the body axes, using Euler transformations $\mathbf{R}_{ELR}$ Therefore:

$$\begin{bmatrix} F_{G_x} \\ F_{G_y} \\ F_{G_z} \end{bmatrix} = mg. \begin{bmatrix} -\sin\Theta \\ \cos\Theta\sin\Phi \\ \cos\Theta\cos\Phi \end{bmatrix} \tag{3.11}$$

In this equation, *g* is the magnitude of the local acceleration of gravity, Θ is the pitch angle of the vehicle and Φ is the roll angle of the vehicle.

As the angles Φ and Θ are not generally the integrals of *P* and *Q*, new motion quantities have to be introduced, by relating the three body axis system rates, *P*, *Q* and *R* to the three Euler rates $\dot{\Psi}$, $\dot{\Theta}$, $\dot{\Phi}$ and. Each of the three Euler rates can be conveniently displayed in one of the axis systems used in transforming a vector from the earth axis system to the body axis system. By applying these translations the following equations are produced:

$$\begin{aligned} \dot{\Phi} &= P + Q\tan\Theta\sin\Phi + R\tan\Theta\cos\Phi \\ \dot{\Theta} &= Q\cos\Phi - R\sin\Phi \\ \dot{\Psi} &= (Q\sin\Phi + R\cos\Phi)/\cos\Theta \end{aligned} \tag{3.12}$$

The above differential equations have to be added to the equations of motion. The moments due to gravity are zero as the body-fixed axes are assumed to have their origin at the centre of gravity of the flying vehicle.

Aerodynamic Forces & Moments

For simulation purposes it is more convenient to express aerodynamic problems in the flight- path axis using true airspeed $\mathbf{V_T}$, angle of attack α, and sideslip angle β instead of *U*, *V* and *W* in the body-axis.

$$\alpha = \tan^{-1}\frac{W}{U}$$
$$\beta = \sin^{-1}\frac{V}{V_{\mathbf{T}}} \tag{3.13}$$

Figure 3-8 shows the angle of attack (α) and the angle of sideslip (β). The angle of attack (α) is the angle between the chord line and the free stream velocity, or relative wind. Whereas the angle of sideslip (β) is the angle between the relative wind and the *x*-body axis in the *xy* plane.

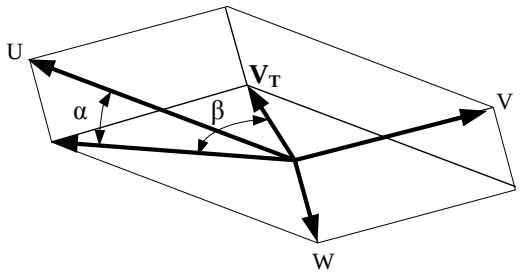

Figure 3-8 Angle of Attack and Angle of Sideslip

The relative motion between the UAV and the atmosphere produce the aerodynamic forces and moments of the UAV. As the atmosphere is assumed to be still, the relative wind velocity is $\mathbf{V_T}$ (where $\mathbf{V_T}$ is the velocity of the vehicle w.r.t. earth). It can be proved that the aerodynamic forces can be expressed in the form:

$$F = \frac{1}{2}\rho V_T^2 S C_F \tag{3.14}$$

Where :

ρ : is the air density

V_T : the magnitude of the relative velocity of the body w.r.t. air

S : a reference area of the body (wing area)

C_F : a dimensionless coefficient depending on the properties of the air and the airframe, the geometry of the air frame and the relative motion between the air and the airframe.

Aerodynamic moments can also be expressed in a similar way. The aerodynamic forces are assumed to consist of three components: *Lift L*, *drag D* and *side force Y*. Lift and drag act on the longitudinal plane normal and parallel respectively to the velocity vector in symmetric flight whereas side force acts along the *y* body axis. The three aerodynamic moments are yaw, pitch and roll (Anderson, 2011, McClamroch, 2011).

Table 3-1 shows the three aerodynamic forces and three aerodynamic moments where *b* is the wing span and *c* the mean aerodynamic chord of the wing.

Aerodynamic forces	**Aerodynamic moments**
$L = \frac{1}{2}\rho V_T^2 S C_L$	$L_A = \frac{1}{2}\rho V_T^2 S b C_l$
$D = \frac{1}{2}\rho V_T^2 S C_D$	$M_A = \frac{1}{2}\rho V_T^2 S c C_m$
$Y = \frac{1}{2}\rho V_T^2 S C_y$	$N_A = \frac{1}{2}\rho V_T^2 S b C_n$

Table 3-1 Aerodynamic Forces and Moments

Thrust Forces and Moments

The thrust is assumed to act on the longitudinal plane *xz* along a thrust line with eccentricity $e_{\mathbf{T}}$ from the origin of the body axes and all the gyroscopic effects are neglected. Then the equations below can be derived from Figure 2.7.

$$
\begin{aligned}
F_{T_x} &= T\cos\varepsilon_T \\
F_{T_z} &= -T\sin\varepsilon_T \\
M_T &= Te_T
\end{aligned}
\tag{3.15}
$$

Thrust produces a forward force in the x-axis, a downward force in the *z*-axis and a pitching moment is also produced in the *y*-axis due to the eccentricity e_T of the thrust line. The rolling moment due to the torque moment of the engine is assumed negligible and is not taken into account in the following analysis.

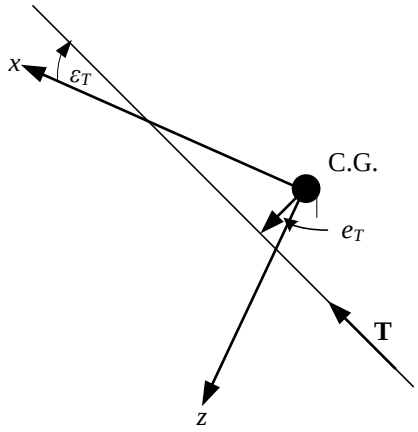

Figure 3-9 Thrust Configuration

3.4.7 Complete Set of the Equations of Motion

As the gravitational forces are proportional to the mass of the vehicle it is convenient to combine them with the inertial ones. Then the equations of motion become:

$$
\begin{aligned}
&m(\dot{U} + QW - RV + g\sin\Theta) = F_{A_x} + F_{T_x} = X \\
&m(\dot{V} + RU - PW - g\cos\Theta\sin\Phi) = F_{A_y} = Y \\
&m(\dot{W} + PV - QU - g\cos\Theta\cos\Phi) = F_{A_z} + F_{T_z} = Z \\
&\dot{P}I_x - \dot{R}I_{xz} + QR(I_z - I_y) - PQI_{xz} = L_A = L \\
&\dot{Q}I_y + PR(I_x - I_z) + (P^2 - R^2)I_{xz} = M_A + M_T = M \\
&\dot{R}I_z - \dot{P}I_{xz} + PQ(I_y - I_x) + QRI_{xz} = N_A = N \\
&\dot{\Phi} = P + Q\tan\Theta\sin\Phi + R\tan\Theta\cos\Phi \\
&\dot{\Theta} = Q\cos\Phi - R\sin\Phi \\
&\dot{\Psi} = (R\cos\Phi + Q\sin\Phi)/\cos\Theta
\end{aligned}
\tag{3.16}
$$

These equations constitute the six degrees of freedom equations of the motion of a rigid flying vehicle.

3.5 Linearisation of the Equations of Motion

The equations of motion as they have been presented in the previous section are in general dynamically and aerodynamically non-linear. In this section, they are linerarised and also decomposed into two motions longitudinal and lateral by assuming small perturbations around the operating point of the flying vehicle and certain aerodynamic properties. The motion of the aerodynamic stability and control derivatives is also introduced and discussed.

3.5.1 Longitudinal and Lateral Equations of Motion

The six aircraft equations of motion (EOM) can be grouped into two sets of three equations. These are three longitudinal EOM and the three lateral directional EOM. This is convenient in that it requires only three equations to be solved simultaneously for many flight conditions.

The three longitudinal EOM consist of the *x* force, z force and *y* moment equations. This is the motion of those movements where the aircraft would only move within

that *xz* plane, that is translation in the *x* direction, translation in the *z* direction and rotation about the *y* axis.

$$
\begin{aligned}
m(\dot{U} + QW - RV + g\sin\Theta) &= F_{Ax} + F_{Tx} \\
m(\dot{W} + PV - QU - g\cos\Theta\cos\Phi) &= F_{Az} + F_{Tz} \\
\dot{Q}I_y + PR(I_x - I_z) + (P^2 - R^2)I_{xz} &= M_A + M_T
\end{aligned}
\tag{3.17}
$$

The lateral EOM consist of the *y* force, *x* moment, z moment equations. This is the motion out of the *xz* plane that is translation in the *y* direction, roll about the *x*-axis and yaw about the *z*-axis.

$$
\begin{aligned}
m(\dot{V} + RU - PW - g\cos\Theta\sin\Phi) &= F_{Ay} = Y \\
\dot{P}I_x - \dot{R}I_{xz} + QR(I_z - I_y) - PQI_{xz} &= L_A = L \\
\dot{R}I_z - \dot{P}I_{xz} + PQ(I_y - I_x) + QRI_{xz} &= N_A = N
\end{aligned}
\tag{3.18}
$$

Equations (2.17) and (2.18) are not decoupled as such but they maybe decoupled under certain flight and geometry conditions after linearisation.

3.5.2 The Perturbed Equations of Motion

Assuming small perturbations around the operating point, or the trimmed conditions of the flying vehicle, and certain aerodynamic properties, the perturbed equations of motion can be obtained by performing the differentials on both sides of the six degrees of freedom equations of motion (Milonidis, 1987). If the differential of each motion quantity is designated by its lower case equivalent (i.e. $dU = u$, etc.), the perturbed equations of motion become:

$$m[\dot{u} + W_0 q + Q_0 w - V_0 r - R_0 v + (g\cos\Theta_0)\theta] = dX$$

$$m[\dot{v} + U_0 r + R_0 u - W_0 p - P_0 w - (g\cos\Theta_0\cos\Phi_0)\phi + (g\sin\Theta_0\sin\Phi_0)\theta] = dY$$

$$m[\dot{w} + V_0 p + P_0 v - U_0 q - Q_0 u + (g\cos\Theta_0\sin\Phi_0)\phi + (g\sin\Theta_0\cos\Phi_0)\theta] = dZ$$

$$\dot{p}I_x - \dot{r}I_{xz} + (Q_0 r + R_0 q)(I_z - I_y) - (P_0 q + Q_0 p)I_{xz} = dL$$

$$\dot{q}I_y + (P_0 r + R_0 p)(I_x - I_z) - (2R_0 r - 2P_0 p)I_{xz} = dM$$

$$\dot{r}I_z - \dot{p}I_{xz} + (P_0 q + Q_0 p)(I_y - I_x) + (Q_0 r + R_0 q)I_{xz} = dN$$

$$\dot{\phi} = p + q\tan\Theta_0\sin\Phi_0 + r\tan\Theta_0\cos\Phi_0 + [(Q_0\cos\Phi_0 - R_0\sin\Phi_0)\tan\Theta_0]\phi +$$
$$[(Q_0\sin\Phi_0 + R_0\cos\Phi_0)(1+\tan^2\Theta_0)]\theta$$

$$\dot{\theta} = q\cos\Phi_0 - r\sin\Phi_0 - (Q_0\sin\Phi_0 + R_0\cos\Phi_0)\phi$$

$$\dot{\psi} = r\cos\Phi_0/\cos\Theta_0 + q\sin\Phi_0/\cos\Theta_0 + [(Q_0\cos\Phi_0 - R_0\sin\Phi_0)/\cos\Theta_0]\phi + \quad (3.19)$$
$$[(Q_0\sin\Phi_0 + R_0\cos\Phi_0)\tan\Theta_0/\cos\Theta_0]\theta$$

In the above equations the zero subscripts denote steady state or trimmed conditions about which the small perturbations are performed.

If the aerodynamic coefficients are assumed to be depended on the present values of their variables and that symmetric reactions can be caused by symmetric disturbances (whereas asymmetric disturbances can cause only asymmetric reactions), the differentials of the aerodynamic forces and moments are the following:

$$
\begin{aligned}
dX &= \overset{\circ}{X}_u u + \overset{\circ}{X}_{\dot{u}} \dot{u} + \overset{\circ}{X}_w w + \overset{\circ}{X}_{\dot{w}} \dot{w} + \overset{\circ}{X}_q q + \overset{\circ}{X}_{\dot{q}} \dot{q} + \overset{\circ}{X}_\eta \eta + \overset{\circ}{X}_{\dot{\eta}} \dot{\eta} + \overset{\circ}{X}_{\delta_T} \delta_T \\
dY &= \overset{\circ}{Y}_v v + \overset{\circ}{Y}_{\dot{v}} \dot{v} + \overset{\circ}{Y}_p p + \overset{\circ}{Y}_{\dot{p}} \dot{p} + \overset{\circ}{Y}_r r + \overset{\circ}{Y}_{\dot{r}} \dot{r} + \overset{\circ}{Y}_\xi \xi + \overset{\circ}{Y}_{\dot{\xi}} \dot{\xi} + \overset{\circ}{Y}_\zeta \zeta + \overset{\circ}{Y}_{\dot{\zeta}} \dot{\zeta} \\
dZ &= \overset{\circ}{Z}_u u + \overset{\circ}{Z}_{\dot{u}} \dot{u} + \overset{\circ}{Z}_w w + \overset{\circ}{Z}_{\dot{w}} \dot{w} + \overset{\circ}{Z}_q q + \overset{\circ}{Z}_{\dot{q}} \dot{q} + \overset{\circ}{Z}_\eta \eta + \overset{\circ}{Z}_{\dot{\eta}} \dot{\eta} + \overset{\circ}{Z}_{\delta_T} \delta_T \\
dL &= \overset{\circ}{L}_v v + \overset{\circ}{L}_{\dot{v}} \dot{v} + \overset{\circ}{L}_p p + \overset{\circ}{L}_{\dot{p}} \dot{p} + \overset{\circ}{L}_r r + \overset{\circ}{L}_{\dot{r}} \dot{r} + \overset{\circ}{L}_\xi \xi + \overset{\circ}{L}_{\dot{\xi}} \dot{\xi} + \overset{\circ}{L}_\zeta \zeta + \overset{\circ}{L}_{\dot{\zeta}} \dot{\zeta} \\
dM &= \overset{\circ}{M}_u u + \overset{\circ}{M}_{\dot{u}} \dot{u} + \overset{\circ}{M}_w w + \overset{\circ}{M}_{\dot{w}} \dot{w} + \overset{\circ}{M}_q q + \overset{\circ}{M}_{\dot{q}} \dot{q} + \overset{\circ}{M}_\eta \eta + \overset{\circ}{M}_{\dot{\eta}} \dot{\eta} + \overset{\circ}{M}_{\delta_T} \delta_T \\
dN &= \overset{\circ}{N}_v v + \overset{\circ}{N}_{\dot{v}} \dot{v} + \overset{\circ}{N}_p p + \overset{\circ}{N}_{\dot{p}} \dot{p} + \overset{\circ}{N}_r r + \overset{\circ}{N}_{\dot{r}} \dot{r} + \overset{\circ}{N}_\xi \xi + \overset{\circ}{N}_{\dot{\xi}} \dot{\xi} + \overset{\circ}{N}_\zeta \zeta + \overset{\circ}{N}_{\dot{\zeta}} \dot{\zeta}
\end{aligned}
\tag{3.20}
$$

$$
\text{where } \overset{\circ}{X}_u = \frac{\partial X}{\partial u}, \overset{\circ}{X}_{\dot{u}} = \frac{\partial X}{\partial \dot{u}}, \ldots, \overset{\circ}{N}_{\dot{\zeta}} = \frac{\partial X}{\partial \dot{\zeta}}
$$

The partial derivatives of the aerodynamic forces and moments with respect to the motion quantities are called *stability derivatives* whereas the partial derivatives with respect to the control deflections and settings are called *control derivatives*.

If quasisteady flow is assumed all the derivatives with respect to the time rates of the variables can be neglected apart from those with respect to *w* and *v* rates. These derivatives are retained to model the downwash and sidewash effects, i.e. the dependence of the flow at the tail on the time history of the motion of the wing (Milonidis, 1987).

3.5.3 Example of Linearisation

As an example of linearisation when steady, straight, level and symmetric flight is assumed, i.e.:

$$
\begin{aligned}
&V_0 = 0 \\
&P_0 = Q_0 = R_0 = 0 \\
&\Phi_0 = \Psi_0 = 0
\end{aligned}
\tag{3.21}
$$

Under the quasisteady assumption, the longitudinal and lateral perturbed equations of motion are simplified to:

Longitudinal

$$
\begin{aligned}
&m[\dot{u} + W_0 q + (g\cos\Theta_0)\theta] = \overset{o}{X}_u u + \overset{o}{X}_w w + \overset{o}{X}_{\dot{w}} \dot{w} + \overset{o}{X}_q q + \overset{o}{X}_\eta \eta + \overset{o}{X}_{\delta_T} \delta_T \\
&m[\dot{w} - U_0 q + (g\sin\Theta_0)\theta] = \overset{o}{Z}_u u + \overset{o}{Z}_w w + \overset{o}{Z}_{\dot{w}} \dot{w} + \overset{o}{Z}_q q + \overset{o}{Z}_\eta \eta + \overset{o}{Z}_{\delta_T} \delta_T \\
&\dot{q} I_y = \overset{o}{M}_u u + \overset{o}{M}_w w + \overset{o}{M}_{\dot{w}} \dot{w} + \overset{o}{M}_q q + \overset{o}{M}_\eta \eta + \overset{o}{M}_{\delta_T} \delta_T \\
&\dot{\theta} = q
\end{aligned}
\tag{3.22}
$$

Lateral

$$
\begin{aligned}
&m[\dot{v} + U_0 r - W_0 P - (g\cos\Theta_0)\phi] = \overset{o}{Y}_v v + \overset{o}{Y}_p p + \overset{o}{Y}_r r + \overset{o}{Y}_\xi \xi + \overset{o}{Y}_\zeta \zeta \\
&\dot{p} I_x - \dot{r} I_{xz} = \overset{o}{L}_v v + \overset{o}{L}_p p + \overset{o}{L}_r r + \overset{o}{L}_\xi \xi + \overset{o}{L}_\zeta \zeta \\
&\dot{r} I_z - \dot{p} I_{xz} = \overset{o}{N}_v v + \overset{o}{N}_p p + \overset{o}{N}_r r + \overset{o}{N}_\xi \xi + \overset{o}{N}_\zeta \zeta \\
&\dot{\phi} = p + r\tan\Theta_0
\end{aligned}
\tag{3.23}
$$

Under these flight conditions the linear longitudinal and lateral equations of motion are completely decoupled. Finally the linerarised equations of motion are absolutely valid only for infinitesimal disturbances they have been proved very useful and widely applicable even when the disturbances are of much larger magnitude and their rates are kept in “reasonably” small values.

3.6 Longitudinal and Lateral Stability

Longitudinal stability and control is concerned with the aircraft’s pitching motion. Lateral stability and control relates to the rolling motion. Directional stability and control relates to an airplane's yawing motion. Lateral and directional stability are closely interrelated and, therefore, the two are referred to as lateral stability (Zipfel, 2007).

3.6.1 Longitudinal Stability

An aircraft in trimmed state implies that the aircraft is in equilibrium and there are no moments tending to pitch the airplane about its centre of gravity. Pitch equilibrium is

achieved by the horizontal tail as it supplies the balancing moment which is controlled by the elevator. If the airplane is statically stable in a longitudinal sense, then if disturbed away from the trim angle of attack, moments are generated that tend to return the airplane to the equilibrium.

Dynamic longitudinal stability is concerned with the motion of a statically stable aircraft. There are two primary forms of longitudinal oscillations of interest with regard to an aircraft attempting to return to an equilibrium trimmed flight condition after being disturbed. The first form is the phugoid mode of oscillation which is a long period, slow oscillation of the aircraft's flight path Figure 3-10.The pilot generally can control this oscillation himself although the more highly damped it is, the greater the drag is.

The second oscillation is a short- period variation of the angle of attack as shown in Figure 3-11 Short-period longitudinal oscillation
. Usually, this oscillation damps out very quickly. However, with its natural short period, the oscillation may worsen if a pilot attempts to damp it out by use of a control surface because of the pilot's slow reaction time where he may get "out of phase" with the oscillation, and thus, induce dynamical instability that may eventually lead to destructive forces.

Figure 3-10 Phugoid longitudinal oscillation

Figure 3-11 Short-period longitudinal oscillation

3.6.2 Lateral Stability

In equilibrium condition, an airplane flies so that the yaw angle is zero. To have static directional stability, a positive yawing moment should be generated if the airplane is disturbed to a negative yaw angle or alternatively by convention, a positive sideslip angle ß and a negative yawing moment generated for a negative sideslip angle excursion. The fuselage and the vertical tail are the two most influential components in directional stability. When an airplane is in a disturbed condition at a sideslip angle ß, in general the fuselage alone will generate a moment that tends to increase the disturbance; that is, it is unstable. The vertical tail is the main component of static directional stability.

An airplane is said to possess lateral static stability if after undergoing a disturbance that rolls it to some bank angle ϕ, it generates forces and moments that tend to reduce the bank angle and restore the equilibrium flight condition.

As mentioned earlier, lateral and directional stability are interrelated. Briefly stated, the motions of an airplane are such that a roll motion causes a yaw motion and a yaw motion causes a roll motion. Thus, cross-coupling exists between the directional static stability and lateral static stability and gives rise to the three important dynamic motions observed: directional divergence, spiral divergence, and Dutch roll as shown if Figure 3-12.

Directional divergence is a result of a directionally unstable airplane. When the airplane yaws or rolls into a sideslip so that side forces on the airplane are generated, the yawing moments that arise continue to increase the sideslip.

Spiral divergence is characterised by an airplane that is very stable directionally but not very stable laterally; for example, a large finned airplane with no dihedral. In this case when the airplane is in a bank and side slipping, the side force tends to turn the plane into the relative wind. The outer wing travels faster, generates more lift, and the airplane will roll to still a higher bank angle. No lateral stability is present to negate this roll. The bank angle increases and the airplane continues to turn into the sideslip in an ever-tightening spiral.

Dutch roll is a motion exhibiting characteristics of both directional divergence and spiral divergence. The lateral stability is strong, whereas the directional stability is weak. If a sideslip disturbance occurs, as the airplane yaws in one direction, the airplane rolls away in a countermotion. The airplane wags its tail from side to side.

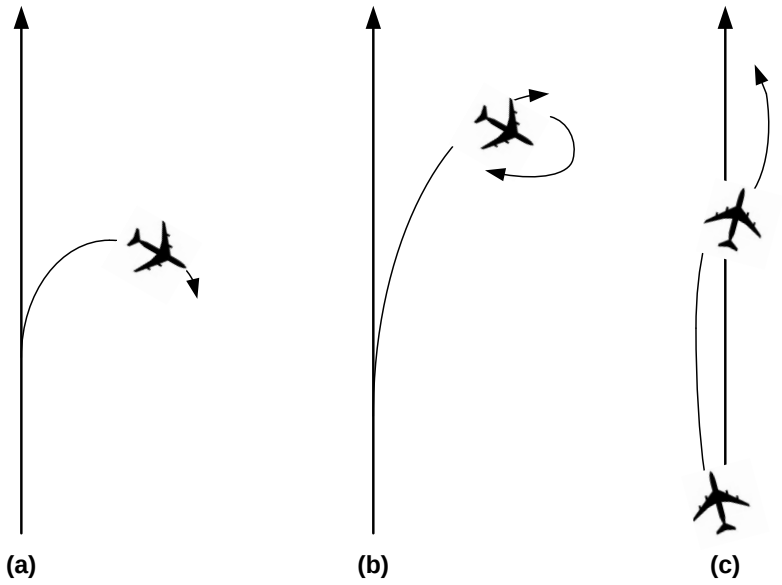

Figure 3-12 Possible flight paths due to dynamic effects (a) spiral divergence; (b) directional divergence; (c) Dutch roll

3.7 Aerodynamic Stability and Control Derivatives

The definitions, the origin and the equations - when applicable of the aerodynamic derivatives are given in this section (Smetana, 1984). All derivatives are assumed to be expressed in stability axes and the compressibility and slipstream effects are neglected.

Analysing each of the partial derivative terms, so that they may be expressed with common longitudinal aerodynamic coefficients such as C_L, C_D and C_m. This is done by analysing a perturbation in angle of attack about the body fixed stability axis.

Longitudinal Derivatives

Definition	Origin	Equation
$\overset{o}{X}_u$	Variation of drag and thrust with u	$-\rho V_T S C_D + \frac{\partial T}{\partial V_T}$
$\overset{o}{Z}_u$	Variation of normal force with u	$-\rho V_T S C_L$
$\overset{\circ}{M}_u$	Variation of pitch and thrust with u	$-\rho V_T S c C_m + e\frac{\partial T}{T\,\partial V_T}$

Table 3-2 Derivatives due to change in forward velocity

Definition	Origin	Equation
$\overset{o}{X}_w$	Lift and drag variations along the x-axis	$\frac{1}{2}\rho V_T S (C_L - \frac{\partial C_D}{\partial \alpha})$
$\overset{o}{Z}_w$	Variation mainly of lift with incidence	$-\frac{1}{2}\rho V_T S (C_D - \frac{\partial C_L}{\partial \alpha})$
$\overset{o}{M}_w$	Static longitudinal stability	$\frac{1}{2}\rho V_T S c \frac{\partial C_m}{\partial \alpha}$

Table 3-3 Derivatives due to change in incidence

Definition	Origin	Equation
$\overset{o}{X}_{\dot{w}}$	Downwash lag on drag (usually negligible)	$-\frac{1}{4}\rho S c (\frac{\partial C_D}{\partial (\frac{\dot{\alpha} c}{2V_T})})$
$\overset{o}{Z}_{\dot{w}}$	Downwash lag mainly on lift of tail	$-\frac{1}{4}\rho S c (\frac{\partial C_L}{\partial (\frac{\dot{\alpha} c}{2V_T})})$
$\overset{o}{M}_{\dot{w}}$	Downwash lag on pitching moment	$\frac{1}{4}\rho S c^2 (\frac{\partial C_m}{\partial (\frac{\dot{\alpha} c}{2V_T})})$

Table 3-4 Derivatives due to downward linear acceleration

Definition	Origin	Equation
X_q^o	Effect of pitch rate on drag (usually negligible)	$-\frac{1}{4}\rho V_T Sc\left(\frac{\partial C_D}{\partial\left(\frac{qc}{2V_T}\right)}\right)$
Z_q^o	Effect of pitch rate on lift (tail and wing contribution)	$-\frac{1}{4}\rho V_T Sc\left(\frac{\partial C_L}{\partial\left(\frac{qc}{2V_T}\right)}\right)$
M_q^o	Effect of pitch rate on pitching moment (damping in pitch)	$\frac{1}{4}\rho V_T Sc^2\left(\frac{\partial C_m}{\partial\left(\frac{qc}{2V_T}\right)}\right)$

Table 3-5 Derivatives due to rate of pitch

Definition	Origin	Equation
X_η^o	Effect of elevator deflection on drag (usually negligible)	$-\frac{1}{2}\rho V_T{}^2 S\frac{\partial C_D}{\partial\eta}$
Z_η^o	Effect of elevator deflection on lift	$-\frac{1}{2}\rho V_T{}^2 S\frac{\partial C_L}{\partial\eta}$
M_η^o	Effect of elevator deflection on pitching moment	$\frac{1}{2}\rho V_T{}^2 Sc\frac{\partial C_m}{\partial\eta}$

Table 3-6 Derivatives due to elevator deflection

Definition	Origin	Equation
$X_{\delta_T}^o$	Variation of thrust along x-axis	$\frac{\partial T}{\partial\delta_T}$
$Z_{\delta_T}^o$	Variation of thrust with throttle along z-axis(usually neglected)	
$M_{\delta_T}^o$	Variation of pitching moment with throttle	$\frac{\partial T}{\partial\delta_T}e_T$

Table 3-7 Derivatives due to change in throttle settings

Lateral Derivatives

Definition	Origin	Equation
Y_v^o	Variation of side force with sideslip angle. Mainly from fin and body.	$\frac{1}{2}\rho V_T S \frac{\partial C_y}{\partial \beta}$
L_v^o	Rolling moment due to sideslip known as combination of wind dihedral effect and fin	$\frac{1}{2}\rho V_T S \frac{\partial C_l}{\partial \beta}$
N_v^o	"Weathercock" or static directional derivative. Main contribution from fin and wing-body.	$\frac{1}{2}\rho V_T Sb \frac{\partial C_n}{\partial \beta}$

Table 3-8 Derivatives due to sideslip

Definition	Origin	Equation
Y_p^o	Change of side force due to rolling velocity. Fin is the main contributor.	$\frac{1}{4}\rho V_T Sb \frac{\partial C_y}{\partial(\frac{pb}{2V_T})}$
L_p^o	The roll damping derivative. Wing is the dominant factor when tail is of conventional size.	$\frac{1}{4}\rho V_T Sb^2 \frac{\partial C_l}{\partial(\frac{pb}{2V_T})}$
N_p^o	Change in yawing moment from rolling velocity. Wing and fin the main contributors.	$\frac{1}{4}\rho V_T Sb^2 \frac{\partial C_n}{\partial(\frac{pb}{2V_T})}$

Table 3-9 Derivatives due to rate of roll

Definition	Origin	Equation
Y_r^o	Variations in side force due to yawing velocity. Fin is the dominant contributor.	$\frac{1}{4}\rho V_T Sb \frac{\partial C_y}{\partial(\frac{rb}{2V_T})}$
L_r^o	Rolling moment due to variations in yawing velocity. Quite important for spiral stability. Major contributors win and fin	$\frac{1}{4}\rho V_T Sb^2 \frac{\partial C_l}{\partial(\frac{rb}{2V_T})}$

N_r^o	Yaw damping derivative. Contributions from wing, fuselage and fin.	$\frac{1}{4}\rho V_T S b^2 (\frac{\partial C_n}{\partial (\frac{rb}{2V_T})})$

Table 3-10 Derivatives due to rate of yaw

Definition	Origin	Equation
Y_ξ^o	Side force due to aileron deflection. Usually negligible.	$\frac{1}{2}\rho V_T{}^2 S \frac{\partial C_y}{\partial \xi}$
L_ξ^o	Rolling moment due to aileron deflection known as aileron defectiveness.	$\frac{1}{2}\rho V_T{}^2 S b \frac{\partial C_l}{\partial \xi}$
N_ξ^o	Yawing moment due to aileron deflection it is cause from the difference between drag on up and down ailerons.	$\frac{1}{2}\rho V_T{}^2 S b \frac{\partial C_n}{\partial \xi}$
Y_ζ^o	Change in side force due to rudder deflection.	$\frac{1}{2}\rho V_T{}^2 S \frac{\partial C_y}{\partial \zeta}$
L_ζ^o	Rolling moment produced from rudder deflection(minor importance)	$\frac{1}{2}\rho V_T{}^2 S b \frac{\partial C_l}{\partial \xi}$
N_ζ^o	Variations in yawing moment with a change in rudder deflection known as rudder effectiveness.	$\frac{1}{2}\rho V_T{}^2 S b \frac{\partial C_n}{\partial \xi}$

Table 3-11 Derivatives due to control deflections

By dividing the force derivatives by the mass of the aircraft and the moment derivatives by the corresponding moment of inertia, normalised aerodynamic stability and control derivatives can be obtained, i.e.:

$$X_u \triangleq \frac{X_u^o}{m} = \frac{1}{m}\frac{\partial X}{\partial u}, M_u \triangleq \frac{M_u^o}{I_y} = \frac{1}{I_y}\frac{\partial M}{\partial u}, \ldots \tag{3.24}$$

Note:

The derivatives due to $\dot{v}$ usually arise from sidewash lags that produce angle of attach variations at the vertical tail. As only little is known for these aerodynamic derivatives, they are usually neglected in the usual formulation of the rigid body

equations. However, there are cases where $\overset{o}{N}_{\dot{v}}$ affects significantly the dutch roll damping and has to be accounted for, but the difficulty is that there is no good way of estimating $\overset{o}{N}_{\dot{v}}$ or of knowing a priori for which configurations is important. Another reason for forces and moments to arise due to rate of change in side velocity is aero elastic effects. These distortion effects are considered negligible for our analysis as the airframe is assumed to be rigid (McRuer et al., 1973).

3.8 Summary

An overview of the fundamental areas of aircraft mechanics which will be used in chapter four to derive the mathematical model and simulate the X-RAE1 UAV has been given. This encapsulates the breakdown of aircraft motion into pitch, roll and yaw. The non-dimensional reference parameters of the aircraft geometry and the control surfaces in addition to the three axis systems and their translation between each other. This is followed by a brief presentation of the derivation of the equations of motion and their linearisation.

CHAPTER

4

The Mathematical Modelling of the X-RAE1 UAV

The UAV being used for this research is the X-RAE1; a remote controlled flight vehicle. The concepts and principles presented in chapter three are used in the development of the six degrees of freedom model for the X-RAE1. A combination of static wind-tunnel tests and ESDU data sheets is used for the formulation of the aerodynamic characteristics of the UAV. A linear and a non-linear model is then presented followed by the dynamics for straight level flight for the X-RAE1.

4.1 The Six Degrees of Freedom Mathematical Model of X-RAE1

X-RAE1 is a small low cost experimental UAV. The primary purpose of the six degrees of freedom mathematical model is to provide baseline data for flight control system analysis and design. The model is dynamically nonlinear but as it is intended to provide simulation data for flight regimes well below stall, the aerodynamic characteristics of it are assumed linear.

The modelling work is based primarily to static wind-tunnel testing of a full-scale unpowered model at RAE Farnborough. The data provided the basis for the derivation of the longitudinal aerodynamic characteristics of the UAV (static and rotational) and they constitute an improved/corrected version of the initial derivation by E Milonidis (Milonidis, 1987). The lateral aerodynamics are based on ESDU data sheets and fundamental theoretical concepts as wind-tunnel or any other kind of data were not available (Milonidis, 1987). A general arrangement of X-RAE1 and some

of its specifications are shown in Figure 4-1and Table 4-1 (Milonidis, 1987), (Trebble, 1985b).

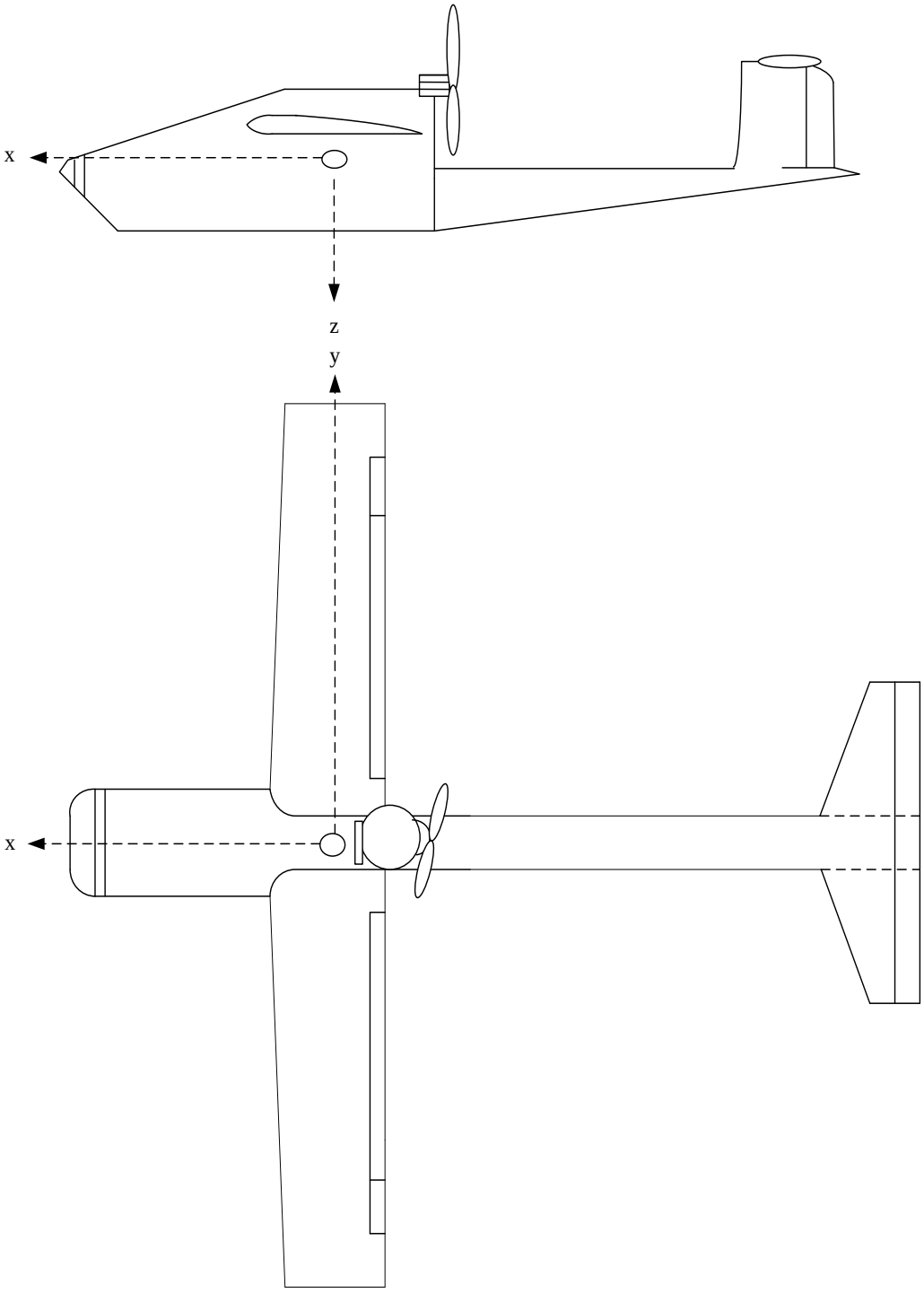

Figure 4-1 X-RAE1 Layout

Length (l_b)	2.1 *m*
Wing Area (*S*)	0.9307 m^2
Wing Span (*b*)	2.638 m^2
Mean Aerodynamic Chord (*C*)	0.353 *m*
Tail Area (S_t)	0.2576 m^2
Distance of the centre of gravity from the leading edge of the mean aerodynamic chord	0.34*c*= 0.121 *m*
Typical Weight (*mg*)	18.5 *Kg*
Typical Payload	2 *Kg*
Speed Range	40 to 68 *Kts*
Engine	Webra '91' 1.5cc two stroke delivering approximately 1.9kwat 14000 RPM and driving a 14 inch dia. x 6 inch pitch propeller.

Table 4-1 X-RAE1 Specifications

4.2 Aerodynamic Forces

The aerodynamic forces are assumed to consist of three components: *lift L*, *drag D* and *side force Y*. Lift and drag act on the longitudinal plane normal and parallel respectively to the velocity vector in symmetric flight whereas side force acts along the *0y* body axis. Any aerodynamic quantity with subscripts is assumed to be expressed in stability axes.

Lift is mainly produced by the lifting surfaces - wing and tail - and by the deflection of the elevator. Lift is expressed in terms of the lift coefficient as:

$$L = \frac{1}{2}\rho V_T^2 S C_L \tag{4.1}$$

$C_L = C_L(\alpha, \dot{\alpha}, q, \eta)$ represents the total aircraft lift coefficient and will be assumed a linear function of the angle of attack α, the time rate of the angle of attack $\dot{\alpha}$, the pitching rate q and the elevator deflection η i.e. :

$$C_L = C_{L_0} + C_{L\alpha}\alpha + C_{L_{\dot{\alpha}}}\left(\frac{\dot{\alpha}c}{2V_T}\right) + C_{L_q}\left(\frac{qc}{2V_T}\right) + C_{L_\eta}\eta \tag{4.2}$$

A full derivation of $C_{L_\alpha}, C_{L_{\dot{\alpha}}}, C_{L_q}$ *and* C_{L_η} from wind-tunnel data (Trebble, 1985b) can be found in Appendix A.1. Modified and corrected from (Milonidis, 1987) to include the modified wing with rounded tips data. The values of the aerodynamic derivatives are shown in Table 4.2.

Drag is derived by a similar formula as lift, namely:

$$D = \frac{1}{2}\rho V_T{}^2 S C_D \tag{4.3}$$

Wing and body are the main contributors and C_D can be estimated from wind – tunnel data as:

$$C_D = C_{D_0} + kC_{L_w}{}^2 \tag{4.4}$$

Where C_{D_0} is the zero-lift is drag and $kC_{L_w}{}^2$ is the drag induced by the lift produced by the wing-body combination.

$C_{L\alpha} = 4.97 \ / \text{rad}$	$C_{D_0} = 0.02245$	$C_{m_\alpha} = -1.24 \ / \text{rad}$
$C_{L_{\dot{\alpha}}} = 2.86 \ / \text{rad}$	$k = 0.0520$	$C_{m_{\dot{\alpha}}} = -9.56 \ / \text{rad}$
$C_{L_q} = 5.25 \ / \text{rad}$		$C_{m_q} = -21.27 \ / \text{rad}$
$C_{L_\eta} = 0.48 \ / \text{rad}$		$C_{m_\eta} = -1.62 / \text{rad}$

Table 4-2 Longitudianl Aerodynamic Derivatives

Side Force is expressed as follows:

$$Y = \frac{1}{2}\rho V_T{}^2 S C_y \tag{4.5}$$

Where $C_y = C_y(V, P, R, \zeta)$ is a linear function of its variables i.e.:

$$C_y = \frac{1}{V_T}Y_v V + \frac{b}{V_T}Y_p P + \frac{b}{V_T}Y_r R + Y_\zeta \zeta \tag{4.6}$$

The main contribution to the ***side force*** arises from the rudder deflection with sideslip and yaw rate also having some effect. Side force due to roll rate is almost negligible. The aerodynamic derivatives Y_v, Y_p, Y_r and Y_ζ in stability axes are given in Table 4-3. ESDU data sheets are mainly used for the estimation of the side force derivatives and can be found in Appendix A.2 (Milonidis, 1987).

$Y_{v_S} \triangleq \frac{\partial Y}{\partial v} / \frac{1}{2}\rho V_T S$	-0.3054
$Y_{p_S} \triangleq \frac{\partial Y}{\partial \rho} / \frac{1}{2}\rho V_T Sb$	$0.078 C_L^{(1)} - 0.3133[\frac{11.32\cos\alpha - 110.19\sin\alpha}{263.8} - 0.18 - \frac{\partial \sigma_\alpha}{\partial(\frac{pb}{V_T})}]^{(2)}$
$Y_{r_S} \triangleq \frac{\partial Y}{\partial r} / \frac{1}{2}\rho V_T Sb$	$-0.0109 + 0.2164(109.51\cos\alpha + 8.87\sin\alpha) / 263.8$
$Y_\zeta \triangleq \frac{\partial Y}{\partial v} / \frac{1}{2}\rho V_T^2 S$	0.1184

Table 4-3 Side Force Aerodynamic Derivatives

1) Lift coefficient.
2) Sidewash term due to body.

4.3 Aerodynamic Moments

The main contributors to the ***pitching moment*** are the wing and the tail. The equation for this is:

$$M_A = \frac{1}{2}\rho V_T^2 S c C_m \tag{4.7}$$

Where:

$$C_m = C_{m_0} + C_{m_\alpha}\alpha + C_{m_{\dot\alpha}}(\frac{\dot\alpha c}{2V_T}) + C_{m_q}(\frac{qc}{2V_T}) + C_{m_\eta}\eta \tag{4.8}$$

$C_{m_0}, C_{m_\alpha}, C_{m_{\dot\alpha}}, C_{m_q}$ and C_{m_η} are derived from wind-tunnel data and their values are recalled in Table 3.2.

The ***rolling moment*** is assumed that depends on the lateral motion quantities *V, P, R* and on the aileron deflection mainly, whereas rudder deflection contributes only a very small amount. The equation for rolling moment is as follows:

$$L_A = \frac{1}{2}\rho V_T{}^2 SbC_l \tag{4.9}$$

where :

$$C_l = \frac{1}{V_T}L_v V + \frac{b}{V_T}L_p P + \frac{b}{V_T}L_r R + L_\xi \xi + L_\zeta \zeta \tag{4.10}$$

All the derivatives are estimated from ESDU data sheets and their values are given in Table 4-4 and can be found in Appendix A.3 (Milonidis, 1987).

$L_{v_S} \triangleq \frac{\partial L}{\partial v} / \frac{1}{2}\rho V_T Sb$	$-0.0005\alpha_b{}^{(1)} - 0.0119 - 0.0016 C_L{}^{(2)} - 0.1969(8.87\cos\alpha - 109.51\sin\alpha)/263.8$
$L_{p_S} \triangleq \frac{\partial L}{\partial p} / \frac{1}{2}\rho V_T Sb^2$	$-0.2457 + -Y_{pF_s}{}^{(3)}\ (11.32\cos\alpha - 110.91\sin\alpha)/263.8$
$L_{r_S} \triangleq \frac{\partial L}{\partial r} / \frac{1}{2}\rho V_T Sb^2$	$-0.00189 + 0.1243 C_L{}^{(2)} + Y_{rF_s}{}^{(4)}\ (8.87\cos\alpha - 109.51\sin\alpha)/263.8$
$L_{\xi_S} \triangleq \frac{\partial L}{\partial \xi} / \frac{1}{2}\rho V_T{}^2 Sb$	-0.2291
$L_\zeta \triangleq \frac{\partial L}{\partial \xi} / \frac{1}{2}\rho V_T{}^2 Sb$	0.00398

Table 4-4 Rolling Moments Derivatives

1) Body incidence measured from its zero lift value.
2) Wing lift coefficient.
3) Contribution of fin to side force derivative due to rate of roll.
4) Contribution of fin to side force derivative due to rate of yaw.

The ***yawing moment*** is derived by an analogous way to the rolling moment. The rudder deflection is now more important than the aileron deflection. The expression for the yawing moment is:

$$N_A = \frac{1}{2}\rho V_T{}^2 SbC_n \tag{4.11}$$

where :

$$C_n = \frac{1}{V_T}N_v V + \frac{b}{V_T}N_p P + \frac{b}{V_T}N_r R + N_\xi \xi + N_\zeta \zeta \tag{4.12}$$

The values of the aerodynamic derivatives are recalled in Table 4-5 and can be found in Appendix A.4 (Milonidis, 1987).

$N_{v_S} \triangleq \frac{\partial N}{\partial v} / \frac{1}{2}\rho V_T Sb$	$-0.0363 + 0.1969$ $(109.51\cos\alpha - 8.87\sin\alpha)/263.8$
$N_{p_s} \triangleq \frac{\partial N}{\partial p} / \frac{1}{2}\rho V_T Sb^2$	$-0.034 C_L{}^{(1)} + 1.23\frac{\partial C_D{}^{'(2)}}{\partial \alpha} - Y_{pF_s}{}^{(3)}$ $(110.91\cos\alpha - 11.32\sin\alpha)/263.8$
$N_{r_s} \triangleq \frac{\partial N}{\partial r} / \frac{1}{2}\rho V_T Sb^2$	$-0.0022 - 0.1261 C_{D_0}{}^{(4)} - 0.009 C_L^{2\,(5)} -$ $Y_{rF_s}{}^{(6)}\ (109.51\cos\alpha - 8.87\sin\alpha)/263.8$
$N_{\xi_s} \triangleq \frac{\partial N}{\partial \xi} / \frac{1}{2}\rho V_T{}^2 Sb$	$0.0195 C_L{}^{(5)}$
$N_\zeta \triangleq \frac{\partial N}{\partial \zeta} / \frac{1}{2}\rho V_T{}^2 Sb$	-0.0492

Table 4-5 Yawing Moment Derivatives

1) Lift coefficient.
2) Viscous drag derivative with respect to angle of attack (per degree)
3) Contribution of fin to side force derivative due to rate of roll.
4) Wing drag at zero lift.
5) Wing lift coefficient.
6) Contribution of fin to side force derivative due to rate of yaw.

4.4 Thrust Forces and Moments

Thrust forces and moments are produced by one 12 inch diameter by 6 inch pitch two blade propeller. The propeller axis lies on the longitudinal plane of the UAV and is parallel to the body *x*-axis. Due to the lack of data a simplified model is used based on performance computation instead of momentum theory. The resulting thrust force is given by equation (4.13) and can be found in Appendix A.1 (Milonidis, 1987, Von Mises, 1959).

$$T = k_1 \delta_T - k_2 V_T^2 \tag{4.13}$$

where:

k_1 = 26.7154 Watts sec /m

k_2 = 0.0055 Watts (m/sec)$^{-3}$

δ_T = throttle setting (from zero to one)

A pitching moment is also produced due to the eccentricity e_T of the thrust line:

$$M_T = T e_T \qquad (e_T = -0.16m) \tag{4.14}$$

The rolling moment due to the torque moment M_{br} of the engine is assumed negligible and is not taken into account in the following analysis.

4.5 Moments and Products of Inertia

The moments and products of inertia of the X-RAE1 were used from previous research carried on the X-RAE1 (AlSwailem, 2003):

$$\begin{aligned} I_x &= 5.00 \ kgr\,m^2 \\ I_y &= 2.10 \ kgr\,m^2 \\ I_z &= 5.80 \ kgr\,m^2 \\ I_{xz} &= 0.17 \ kgr\,m^2 \end{aligned} \tag{4.15}$$

4.6 The Equations of Motion of X-RAE1

After the evaluation of the aerodynamic and thrust forces and moments acting on the airframe the equations of motion of X-RAE1 can be developed. The following aspects are taken into account for their derivation:

1. All the derivatives given in stability axes have to be transformed to body axes.
2. The aerodynamic coefficients C_L, C_D and C_m are estimated with reference to the point O_A on the centre line chord of the wing at distance 0.34c from the leading edge of the mean aerodynamic chord whereas the centre of gravity of the airframe is assumed to be the centroid of the equivalent cross-section at O_A as shown in Figure 4-2.

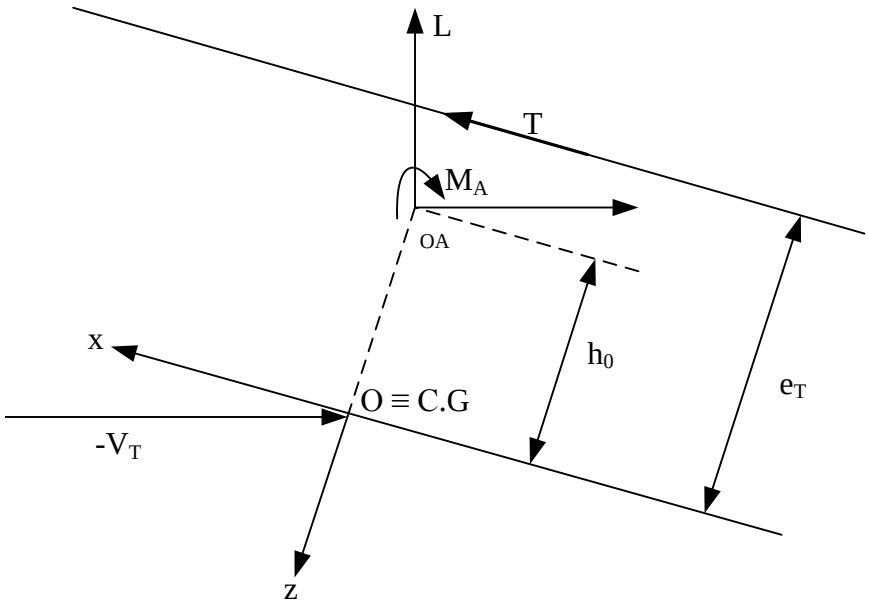

Figure 4-2 Pitching moment reference point

If $q = \frac{1}{2}\rho V_T^2$, the equations of motion of X-RAE1 in body axis become:

$$\dot{U} = RV - QW - g\sin\Theta + [\mathrm{q}\,S(C_L\sin\alpha - C_D\cos\alpha) + T]/m$$

$$\dot{V} = PW - RU + g\cos\Theta\sin\Phi + (\mathrm{q}\,SC_y)/m$$

$$\dot{W} = QU - PV + g\cos\Theta\cos\Phi + [\mathrm{q}\,S(-C_L\cos\alpha - C_D\sin\alpha)]/m$$

$$\dot{P}I_x = \dot{R}I_{xz} - QR(I_z - I_y) + PQI_{xz} + qSbC_l$$

$$\dot{Q}I_y = PR(I_z - I_x) - (P^2 - R^2)I_{xz} + qScC_m + qS(C_L\sin\alpha - C_D\cos\alpha)h_0 + Te_T \quad (4.16)$$

$$\dot{R}I_z = -\dot{P}I_{xz} + PQ(I_y - I_x) + QRI_{xz} + qScC_n$$

$$\dot{\Phi} = P + Q\tan\Theta\sin\Phi + R\tan\Theta\cos\Phi$$

$$\dot{\Theta} = Q\cos\Phi - R\sin\Phi$$

$$\dot{\Psi} = (R\cos\Phi - Q\sin\Phi)/\cos\Theta$$

where:

$$V_T = (U^2 + W^2 + V^2)^{\frac{1}{2}},\ \alpha = \tan^{-1}\frac{W}{U} \text{ and } \dot{\alpha} = \frac{\dot{W}U - \dot{U}W}{U^2 + W^2}$$

The above equations of motion can be used for different trimmed conditions (i.e. the initial conditions) to develop a linearised model of the UAV X-RAE1.

4.7 Trim Conditions

For straight horizontal and level flight with velocity V_{T_0}, the X-RAE1 has to have specific combination of control surfaces deflections, throttle settings and the angle of attack required for sustained flight at V_{T_0} m/sec . These values are known as the trim conditions, which are calculated below.

The trimmed values of the motion quantities become:

$$\begin{aligned} U_0 &= V_{T_0} \cos\alpha_0 \\ W_0 &= V_{T_0} \sin\alpha_0 \\ Q_0 &= 0 \\ \Theta_0 &= \alpha_0 \\ V_0 &= P_0 = R_0 = 0 \\ \Phi_0 &= \Psi_0 = 0 \end{aligned} \tag{4.17}$$

The lateral conditions can be easily obtained by setting the aileron and rudder at their zero value positions. Then the longitudinal equations are the following:

$$\begin{aligned} F_x &= M\dot{U} = -mg\sin\alpha + \bar{q}S(C_L \sin\alpha - C_D \cos\alpha) + T \\ F_z &= M\dot{W} = mg\cos\alpha + \bar{q}S(C_L \cos\alpha + C_D \sin\alpha) \\ M &= \dot{Q}I_y = \bar{q}ScC_M + Te_T + \bar{q}S(C_L \sin\alpha - C_D \cos\alpha)h_0 \end{aligned} \tag{4.18}$$

where:

$$\begin{aligned} C_L &= C_{L_0} + C_{L_\alpha}\alpha + C_{L_\eta}\eta \\ C_D &= C_{D_0} + kC_{L_W}^2 \\ C_{L_W} &= CL_{W_0} + CL_{W_\alpha}\alpha \\ C_M &= C_{M_0} + C_{M_\alpha}\alpha + C_{M_\eta}\eta \end{aligned} \tag{4.19}$$

For equilibrium:

$$\begin{aligned} \dot{U} = \dot{W} &= 0 \\ M &= 0 \end{aligned}$$

Eliminating thrust T from equations (4.2) gives:

$$T = \frac{qSc}{e_T}C_M - qS(C_L \sin\alpha - C_D \cos\alpha) + \frac{h_0}{e_T} \tag{4.20}$$

$$\begin{aligned} F_x &= -mg\sin\alpha + qS(1 - \frac{h_0}{e_T})(C_L \sin\alpha - C_D \cos\alpha) - \frac{qSc}{e_T}C_M \\ F_z &= mg\cos\alpha - qS(C_L \cos\alpha + C_D \sin\alpha) \end{aligned} \tag{4.21}$$

The system of equations (4.5) is non-linear and it is solved numerically for the unknown vector $\mathbf{x} = [\alpha \;\; \eta]^T$ using the Newton-Raphson method.

$$\mathbf{x}_{n+1} = \mathbf{x}_n - \mathbf{J}^{-1}\begin{bmatrix} F_X \\ F_Z \end{bmatrix} \tag{4.22}$$

where **J** is the Jacobian

$$\mathbf{J} = \begin{bmatrix} \dfrac{\partial F_X}{\partial \alpha} & \dfrac{\partial F_X}{\partial \eta} \\ \dfrac{\partial F_Z}{\partial \alpha} & \dfrac{\partial F_Z}{\partial \eta} \end{bmatrix} \tag{4.23}$$

and

$$\begin{aligned}
\frac{\partial F_X}{\partial \alpha} &= (1-\frac{h_0}{e_T})qS[(C_{L_\alpha} - C_D)\sin\alpha + (C_L - C_{D_\alpha})\cos\alpha] \\
&\quad - mg\cos\alpha - \frac{qSc}{e_T}C_{m_\alpha} \\
\frac{\partial F_X}{\partial \eta} &= (1-\frac{h_0}{e_T})qSC_{L_\eta}\sin\alpha - \frac{qSc}{e_T}C_{m_\eta} \\
\frac{\partial F_Z}{\partial \alpha} &= qS[(C_L - C_{D_\alpha})\sin\alpha + (C_{L_\alpha} - C_{D_\alpha})\cos\alpha] - mg\sin\alpha \\
\frac{\partial F_Z}{\partial \eta} &= qSC_{L_\eta}\sin\alpha
\end{aligned} \tag{4.24}$$

Newton-Raphson method is a numerical method and the solution depends on the initial condition of the unknown vector. In our case the initial solution vector is derived through "a priory" designer knowledge based on the assumption that Weight is equal to lift with zero elevator deflection at the steady-state flight. Using equations (4.19) this will produce an initial vector

$$\mathbf{x}_0 = [-0.0985 \;\; 0]^T \tag{4.25}$$

for a nominal velocity V_{T_0} of 30 m/sec. Newton-Raphson provides the following trim conditions:

Angle of attack	$\alpha_0 = -0.0867$ rad
Elevator	$\eta_0 = -0.0054$ rad
Aileron	$\xi_0 = 0.0$ rad
Rudder	$\zeta_0 = 0.0$ rad
Throttle	$\delta_T = 0.6854$ or 68.54%

These results were tested against an initial vector $\mathbf{x}_0 = [0 \;\; 0]^T$ which provided exactly the same outcome. The linear model program has been created in Matlab and responses generated directly from the Simulink model.

4.7.1 The Linearised Model of X-RAE1 at 30m/sec

The longitudinal linear model at 30m/s

By rearranging Equations (3.22) the state space model of the linearised longitudinal equations of motion of the X-RAE1 can be obtained (Milonidis, 1987):

$$\begin{bmatrix} \dot{u} \\ \dot{w} \\ \dot{q} \\ \dot{\theta} \end{bmatrix} = \begin{bmatrix} x_u & x_w & x_q & a_1 g \\ z_u & z_w & z_q & a_2 g \\ m_u & m_w & m_q & a_3 g \\ 0 & 0 & 1 & 0 \end{bmatrix} \begin{bmatrix} u \\ w \\ q \\ \theta \end{bmatrix} + \begin{bmatrix} x_\eta & x_{\delta_T} \\ z_\eta & z_{\delta_T} \\ m_\eta & m_{\delta_T} \\ 0 & 0 \end{bmatrix} \begin{bmatrix} \eta \\ \delta_T \end{bmatrix} \tag{4.26}$$

where:

$$x_u = X_u + Z_u X_{\dot{w}} / (1 - Z_{\dot{w}})$$
$$x_w = X_w + Z_w X_{\dot{w}} / (1 - Z_{\dot{w}})$$
$$x_q = X_q - W_0 + (Z_q + U_0) X_{\dot{w}} / (1 - Z_{\dot{w}})$$
$$a_1 = -\cos\theta_0 - (\sin\theta_0) X_{\dot{w}} / (1 - Z_{\dot{w}})$$
$$x_\eta = X_\eta + Z_\eta X_{\dot{w}} / (1 - Z_{\dot{w}})$$
$$x_{\delta_T} = X_{\delta_T} + Z_{\delta_T} X_{\dot{w}} / (1 - Z_{\dot{w}})$$
$$z_u = Z_u / (1 - Z_{\dot{w}})$$
$$z_w = Z_w / (1 - Z_{\dot{w}})$$
$$z_q = (Z_q + U_0) X_{\dot{w}} / (1 - Z_{\dot{w}})$$
$$a_2 = -(\sin\theta_0) / (1 - Z_{\dot{w}})$$
$$z_\eta = Z_\eta / (1 - Z_{\dot{w}})$$
$$z_{\delta_T} = Z_{\delta_T} / (1 - Z_{\dot{w}})$$

$$m_u = M_u + Z_u M_{\dot{w}} / (1 - Z_{\dot{w}})$$
$$m_w = M_w + Z_w M_{\dot{w}} / (1 - Z_{\dot{w}})$$
$$m_q = M_q + (Z_q + U_0) M_{\dot{w}} / (1 - Z_{\dot{w}})$$
$$a_3 = -(\sin\theta_0) M_{\dot{w}} / (1 - Z_{\dot{w}})$$
$$m_\eta = M_\eta + Z_\eta M_{\dot{w}} / (1 - Z_{\dot{w}})$$
$$m_{\delta_T} = M_{\delta_T} + Z_{\delta_T} M_{\dot{w}} / (1 - Z_{\dot{w}})$$

The aerodynamic stability and control derivatives for a trimmed flight at 30 m/sec are evaluated for the linear longitudinal motion in appendix A.1. Their normalised values in body axes are shown in Table 4-6.

$X_u = -0.142$	$Z_u = -1.049$	$M_u = -0.208$
$X_w = -0.233$	$Z_w = -4.545$	$M_w = -3.463$
$X_{\dot{w}} = -0.001$	$Z_{\dot{w}} = -0.015$	$M_{\dot{w}} = -0.161$
$X_q = -0.068$	$Z_q = -0.806$	$M_q = -10.753$
$X_\eta = -1.153$	$Z_\eta = -13.262$	$M_\eta = -139.253$
$X_{\delta_T} = 1.444$	$Z_{\delta_T} = 0.0$	$M_{\delta_T} = -2.036$

Table 4-6 Normalised longitudinal derivatives at 30 m/sec -Body Axis

Substituting the normalised longitudinal derivatives into the longitudinal state space model gives:

$$\begin{bmatrix} \dot{u} \\ \dot{v} \\ \dot{q} \\ \dot{\theta} \end{bmatrix} = \begin{bmatrix} -0.142 & -0.227 & 2.493 & -9.771 \\ -1.033 & -4.476 & 28.639 & 0.837 \\ -0.042 & -2.744 & -15.351 & -0.134 \\ 0 & 0 & 1 & 0 \end{bmatrix} \begin{bmatrix} u \\ w \\ q \\ \theta \end{bmatrix} + \begin{bmatrix} -1.136 & 1.444 \\ -13.060 & 0 \\ -137.157 & -2.036 \\ 0 & 0 \end{bmatrix} \begin{bmatrix} \eta \\ \delta_T \end{bmatrix} \quad (4.27)$$

The eigenvalues of the longitudinal system of equations for nearly all aircrafts in most flight conditions are two sets of complex numbers. Therefore the modes of motion are two oscillations:

- *The short period* a relatively high frequency (ω_{sp}) oscillation with heavy damping (ζ_{sp}) primarily consisting of variations in α and β with forward velocity remaining almost constant.
- *The phugoid* a relatively small frequency (ω_{ph}) oscillation with very light damping (ζ_{ph}) characterised by variations in *u* and θ with α about constant.

The characteristic equation of the longitudinal system is:

$$p(s) = s^4 + 19.9694s^3 + 150.122s^2 + 12.146s + 26.238$$

And the eigenvalues of it are:

Short Period: $-9.953 \pm j7.044$

Phugoid: $-0.032 \pm j0.419$

The corresponding natural frequencies and damping ratios of the longitudinal dynamics are given in Table 4-7.

	Natural frequency	Damping
Short period	$\omega_{n_{sp}} = 12.1934\ rad/\sec$	$\zeta_{sp} = 0.8163$
Phugoid	$\omega_{n_{ph}} = 0.4202\ rad/\sec$	$\zeta_{ph} = 0.0762$

Table 4-7 Longitudinal modes of X-RAE1 at 30 m/s

Due to the light damping ration ζ_{ph} (almost close to zero) there is a need to control the phugoid mode to avoid low frequency oscillations Although the short period is heavily damped it is also a good control strategy to make it fast so the transient effects mainly on the pitching rate *q* will die out rapidly.

The lateral linear model at 30 m/sec

The state space model of the linearised lateral equations of motion of the X-RAE1 is:

$$\begin{bmatrix} \dot{v} \\ \dot{p} \\ \dot{r} \\ \dot{\phi} \end{bmatrix} = \begin{bmatrix} Y_v & Y_p + W_0 & Y_r - U_0 & g\cos\theta_0 \\ l_v & l_p & l_r & 0 \\ n_v & n_p & n_r & 0 \\ 0 & 1 & \tan\theta_0 & 0 \end{bmatrix} \begin{bmatrix} v \\ p \\ r \\ \phi \end{bmatrix} + \begin{bmatrix} Y_\xi & Y_\zeta \\ l_\xi & l_\zeta \\ n_\xi & n_\zeta \\ 0 & 0 \end{bmatrix} \begin{bmatrix} \xi \\ \zeta \end{bmatrix}$$

Where :

$$\mathrm{D} = \frac{I_x I_z - I_{xz}^2}{I_x I_z} \qquad \mathrm{n}_v = (N_v + (\frac{I_{xz}}{I_z} L_v))/\mathrm{D} \qquad l_\xi = (L_\xi + (\frac{I_{xz}}{I_x} N_\xi))/\mathrm{D}$$

$$l_v = (L_v + (\frac{I_{xz}}{I_x} N_v))/\mathrm{D} \qquad \mathrm{n}_p = (N_p + (\frac{I_{xz}}{I_z} L_p))/\mathrm{D} \qquad l_\zeta = (L_\zeta + (\frac{I_{xz}}{I_x} N_\xi))/\mathrm{D}$$

$$l_p = (L_p + (\frac{I_{xz}}{I_x} N_p))/\mathrm{D} \qquad \mathrm{n}_r = (N_r + (\frac{I_{xz}}{I_z} L_r))/\mathrm{D} \qquad n_\xi = (N_\xi + (\frac{I_{xz}}{I_z} L_\xi))/\mathrm{D}$$

$$l_r = (L_r + (\frac{I_{xz}}{I_x} N_r))/\mathrm{D} \qquad n_\zeta = (N_\zeta + (\frac{I_{xz}}{I_z} L_\zeta))/\mathrm{D}$$

(4.28)

The normalised stability and control derivatives of the lateral motion at 30 m/sec are given in Table 4-8. Detailed determination of their values can be found in appendix A.2.

$Y_v = -0.2823$	$L_v =$ -0.222	$N_v =$ 0.365
$Y_p = 0.120$	$L_p =$ -5.708	$N_p =$ -0.011
$Y_r = 0.180$	$L_r =$ 1.708	$N_r = -$ -0.996
$Y_\xi = 0.0$	$L_\xi =$ -61.595	$N_\xi = 6.471$
$Y_\zeta = 3.863$	$L_\zeta = 1.267$	$N_\zeta =$ -13.511

Table 4-8 Normalised Lateral Derivatives at 30 m/sec - Body Axes

Substituting the normalised longitudinal derivatives into the longitudinal state space model gives:

$$\begin{bmatrix} \dot{v} \\ \dot{p} \\ \dot{r} \\ \dot{\phi} \end{bmatrix} = \begin{bmatrix} -0.282 & -2.479 & -29.707 & 9.770 \\ -0.188 & -5.726 & 1.532 & 0 \\ 0.357 & -0.177 & -0.933 & 0 \\ 0 & 1 & -0.087 & 0 \end{bmatrix} \begin{bmatrix} v \\ p \\ r \\ \phi \end{bmatrix} + \begin{bmatrix} 0 & 3.863 \\ -61.436 & 0.808 \\ 4.670 & -13.487 \\ 0 & 0 \end{bmatrix} \begin{bmatrix} \xi \\ \zeta \end{bmatrix} \quad (4.29)$$

The eigenvalues of the lateral system of motion are usually a set of two real and two complex numbers which constitute the three modes of the lateral motion:

- *The Dutch roll* primarily consists of sideslip and yaw. The damping and natural frequency of the *dutch roll* vary with aircraft and flight conditions where the damping may become very light.
- *The roll subsidence* is the one degree of freedom rolling response to aileron deflection. Usually a small time constant is required.
- *The spiral divergence* is a combination of an increase in yaw and roll angle and the aircraft eventually falls into a high-speed spiral dive.

The characteristic polynomial of the lateral system matrix is:

$$p(s) = s^4 + 6.943s^3 + 17.714s^2 + 66.907s - 2.155$$

And the eigenvalues of it are the following:

Dutch Roll: $-0.549 \pm j3.344$

Roll Subsidence: -5.877

Spiral Divergence: 0.032

The corresponding natural frequencies and damping ratios and time constants of the lateral modes are given in Table 4-9.

Dutch roll	Roll subsidence	Spiral divergence
$\omega_{n_d} = 3.389\, rad/\sec$ $\zeta_d = 0.162$	$T_r = 0.170 \sec s$	$T_s = 31.25 \sec s$

Table 4-9 Lateral modes of X-RAE1 at 30 m/s

The dutch roll mode is of reasonable short period and lightly damped so an attempt should be made to overcome its oscillations. The unstable spiral mode has very large time constant $(T_s = 31.25 \sec s)$ and can be easily tolerated by the pilot. As a stable spiral mode may be usually achieved at the expense of a less well damped dutch roll it does not seem advisable to be controlled by the flight control system.

The validity of the linear longitudinal model was checked by comparing the longitudinal response to a pulse of 0.005 rad and duration of 1 sec of the elevator

with that generated by the non-linear model at the same flight conditions. The validity of the linear lateral model due to a similar aileron deflection was compared. The responses shown in Figure 4-3 and Figure 4-4 show an almost identical match over the duration of the simulation for all the states, hence confirming the validity for small perturbation analysis.

Nonlinear responses	Linear responses
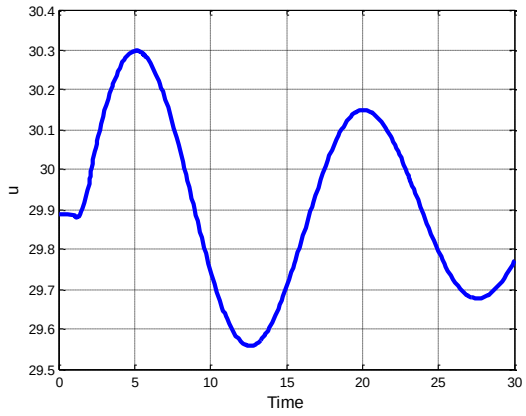	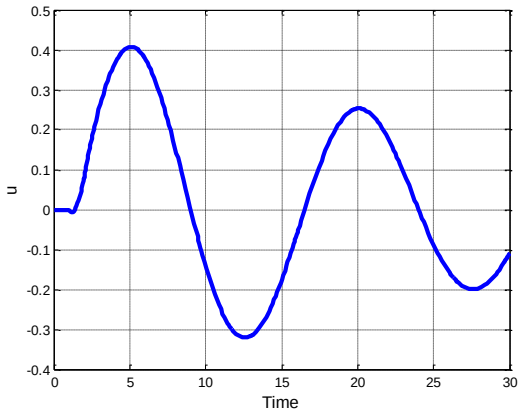
Forward velocity *u* response to elevator deflection	
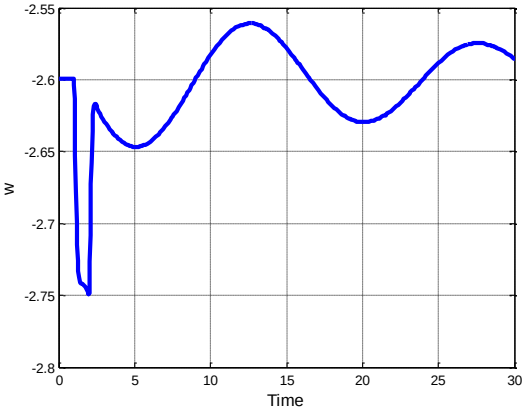	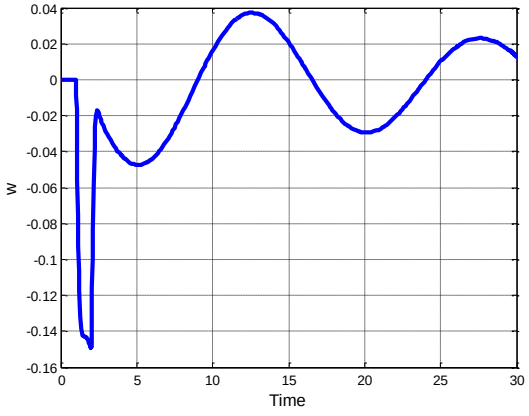
Downward velocity *w* response to elevator deflection	
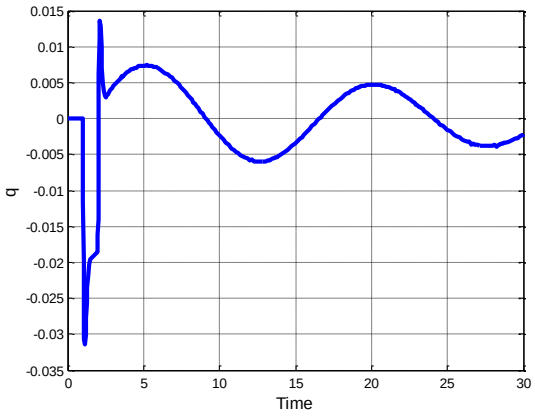	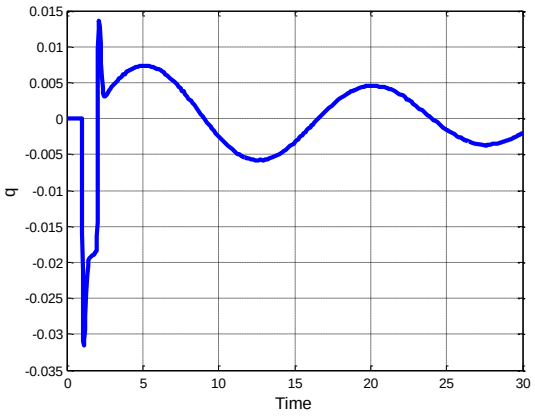
Pitching rate *q* response to elevator deflection	

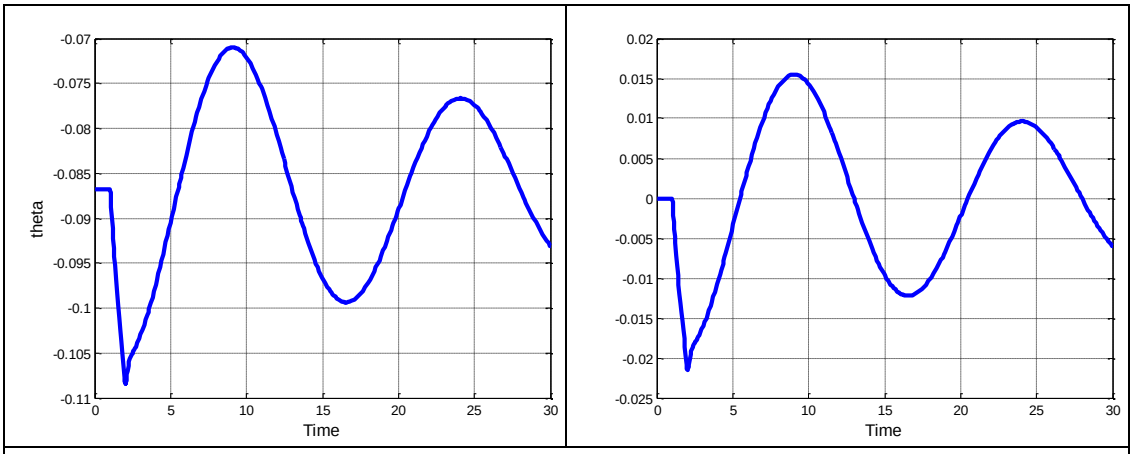

Pitch angle θ response to elevator deflection

Figure 4-3 nonlinear and linear responses comparsion due to elevator deflection of amplitude 0.005 rad and duration of 1 second

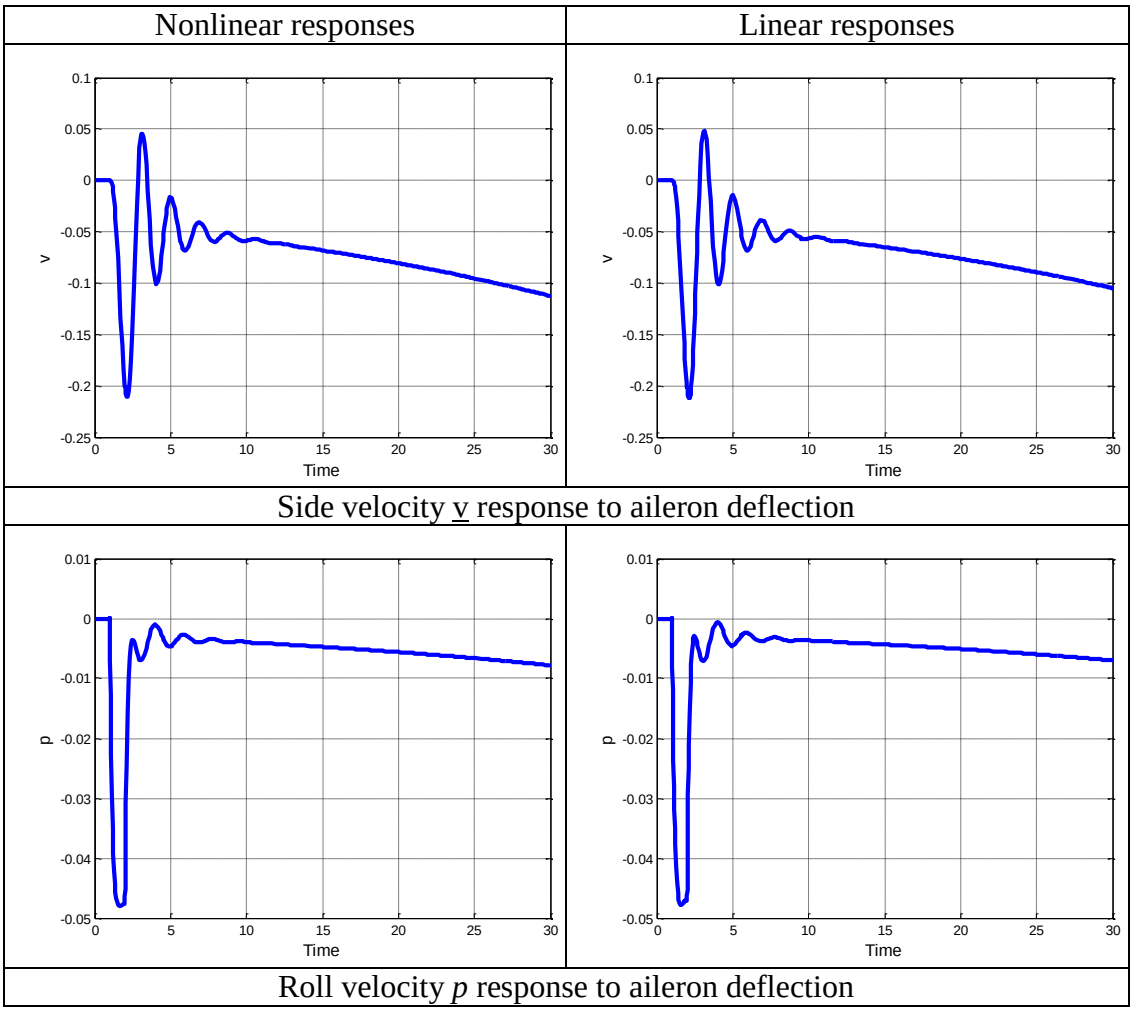

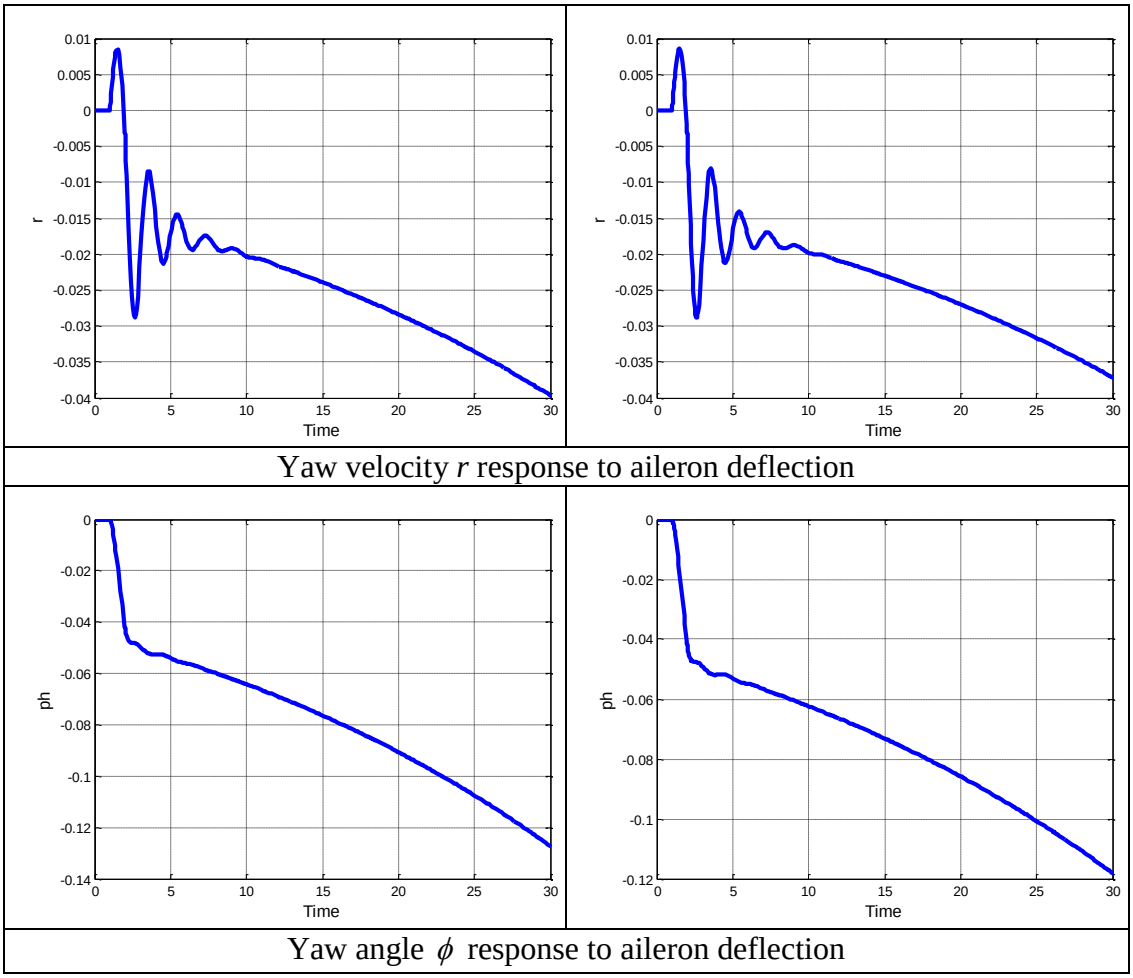

Figure 4-4 nonlinear and linear responses comparison due to aileron deflection of amplitude 0.005 rad and duration of 1 second

4.7.2 The Linearised Model of X-RAE1 at a Range of Velocities

Following the same analysis in section 4.7.1 the trim conditions at different velocities of the X-RAE1 are presented below:

The linearised model of X-RAE1 at 22m/sec

At trim conditions the control deflections and the throttle setting for steady, straight, symmetric flight at 22 m/sec are as follows:

Angle of attack $\alpha_0 = -0.0206$

Elevator $\eta_0 = -0.0607$ rad

Aileron $\xi_0 = 0.0$ rad

Rudder $\zeta_0 = 0.0$ rad

Throttle $\delta_T = 0.5413$ or 54.13%

The longitudinal linear model matrix at 22 m/sec is:

$$\begin{bmatrix} \dot{u} \\ \dot{v} \\ \dot{q} \\ \dot{\theta} \end{bmatrix} = \begin{bmatrix} -0.086 & 0.161 & -0.437 & -9.805 \\ -0.947 & -3.335 & 21.083 & 0.199 \\ 0.198 & -2.140 & -11.317 & -0.032 \\ 0 & 0 & 1 & 0 \end{bmatrix} \begin{bmatrix} u \\ w \\ q \\ \theta \end{bmatrix} + \begin{bmatrix} -0.145 & 1.444 \\ -7.048 & 0 \\ -73.936 & -2.036 \\ 0 & 0 \end{bmatrix} \begin{bmatrix} \eta \\ \delta_T \end{bmatrix} \quad (4.30)$$

And the eigenvalues of it are:

Short Period: $-7.3396 \pm j5.4004$

Phugoid: $-0.0289 \pm j0.5628$

The lateral linear model matrix at 22 m/sec is:

$$\begin{bmatrix} \dot{v} \\ \dot{p} \\ \dot{r} \\ \dot{\phi} \end{bmatrix} = \begin{bmatrix} -0.207 & -0.293 & -21.858 & 9.805 \\ -0.126 & -4.258 & 1.509 & 0 \\ 0.257 & -0.610 & -0.677 & 0 \\ 0 & 1 & 0.021 & 0 \end{bmatrix} \begin{bmatrix} v \\ p \\ r \\ \phi \end{bmatrix} + \begin{bmatrix} 0 & 2.076 \\ -33.257 & 0.435 \\ 1.327 & -7.253 \\ 0 & 0 \end{bmatrix} \begin{bmatrix} \xi \\ \zeta \end{bmatrix} \quad (4.31)$$

And the eigenvalues of it are the following:

Dutch Roll: $-0.4788 \pm j2.5758$

Roll Subsidence: -4.283

Spiral Divergence: 0.0936

The linearised model of X-RAE1 at 26m/sec

At trim conditions the control deflections and the throttle setting for steady, straight, symmetric flight at 26 m/sec are as follows:

Angle of attack $\alpha_0 = -0.0613$

Elevator $\eta_0 = -0.0261$ rad

Aileron $\xi_0 = 0.0$ rad

Rudder $\zeta_0 = 0.0$ rad

Throttle $\delta_T = 0.5924$ or 59.24%

The longitudinal linear model matrix at 26 m/sec is:

$$\begin{bmatrix} \dot{u} \\ \dot{v} \\ \dot{q} \\ \dot{\theta} \end{bmatrix} = \begin{bmatrix} -0.114 & -0.048 & 1.528 & -9.789 \\ -0.982 & -3.901 & 24.870 & 0.591 \\ 0.063 & -2.438 & -13.335 & -0.095 \\ 0 & 0 & 1 & 0 \end{bmatrix} \begin{bmatrix} u \\ w \\ q \\ \theta \end{bmatrix} + \begin{bmatrix} -0.603 & 1.444 \\ -9.827 & 0 \\ -103.113 & -2.036 \\ 0 & 0 \end{bmatrix} \begin{bmatrix} \eta \\ \delta_T \end{bmatrix} \quad (4.32)$$

And the eigenvalues of it are:

Short Period: $-8.6453 \pm j6.2107$

Phugoid: $-0.0299 \pm j0.4785$

The lateral linear model matrix at 26 m/sec is:

$$\begin{bmatrix} \dot{v} \\ \dot{p} \\ \dot{r} \\ \dot{\phi} \end{bmatrix} = \begin{bmatrix} -0.245 & -1.454 & -25.794 & 9.788 \\ -0.158 & -4.986 & 1.504 & 0 \\ 0.307 & -0.374 & -0.804 & 0 \\ 0 & 1 & -0.061 & 0 \end{bmatrix} \begin{bmatrix} v \\ p \\ r \\ \phi \end{bmatrix} + \begin{bmatrix} 0 & 2.902 \\ -46.268 & 0.607 \\ 2.871 & -10.130 \\ 0 & 0 \end{bmatrix} \begin{bmatrix} \xi \\ \zeta \end{bmatrix} \quad (4.33)$$

And the eigenvalues of it are the following:

Dutch Roll: $-0.5018 \pm j2.9540$

Roll Subsidence: -5.0874

Spiral Divergence: 0.0542

The linearised model of X-RAE1 at 34m/sec

At trim conditions the control deflections and the throttle setting for steady, straight, symmetric flight at 34 m/sec are as follows:

Angle of attack $\alpha_0 = -0.1037$

Elevator $\eta_0 = 0.0081$ rad

Aileron $\xi_0 = 0.0$ rad

Rudder $\zeta_0 = 0.0$ rad

Throttle $\delta_T = 0.8100$ or 81%

The longitudinal linear model matrix at 34 m/sec is:

$$\begin{bmatrix} \dot{u} \\ \dot{v} \\ \dot{q} \\ \dot{\theta} \end{bmatrix} = \begin{bmatrix} -0.169 & -0.387 & 3.376 & -9.756 \\ -1.095 & -5.057 & 32.403 & 1.000 \\ -0.130 & -3.056 & -17.368 & -0.160 \\ 0 & 0 & 1 & 0 \end{bmatrix} \begin{bmatrix} u \\ w \\ q \\ \theta \end{bmatrix} + \begin{bmatrix} -1.744 & 1.444 \\ -16.748 & 0 \\ -176.066 & -2.036 \\ 0 & 0 \end{bmatrix} \begin{bmatrix} \eta \\ \delta_T \end{bmatrix} \quad (4.34)$$

And the eigenvalues of it are:

Short Period: $-11.2625 \pm j7.8924$

Phugoid: $-0.0341 \pm j0.3747$

The lateral linear model matrix at 34 m/sec is:

$$\begin{bmatrix} \dot{v} \\ \dot{p} \\ \dot{r} \\ \dot{\phi} \end{bmatrix} = \begin{bmatrix} -0.320 & -3.414 & -33.613 & 9.754 \\ -0.218 & -6.474 & 1.582 & 0 \\ 0.407 & -0.008 & -1.064 & 0 \\ 0 & 1 & -0.104 & 0 \end{bmatrix} \begin{bmatrix} v \\ p \\ r \\ \phi \end{bmatrix} + \begin{bmatrix} 0 & 4.962 \\ -78.765 & 1.038 \\ 6.723 & -17.324 \\ 0 & 0 \end{bmatrix} \begin{bmatrix} \xi \\ \zeta \end{bmatrix} \quad (4.35)$$

And the eigenvalues of it are the following:

Dutch Roll: $-0.6083 \pm j3.7412$

Roll Subsidence: -6.6587

Spiral Divergence: 0.0188

The eigenvalues for the longitudinal modes at different velocities are shown in Figure 4-5. It can be seen that the phugoid mode remains almost invariant to velocity change. The short period mode has an almost invariant damping coefficient with respect to velocity variations and an increasing natural frequency.

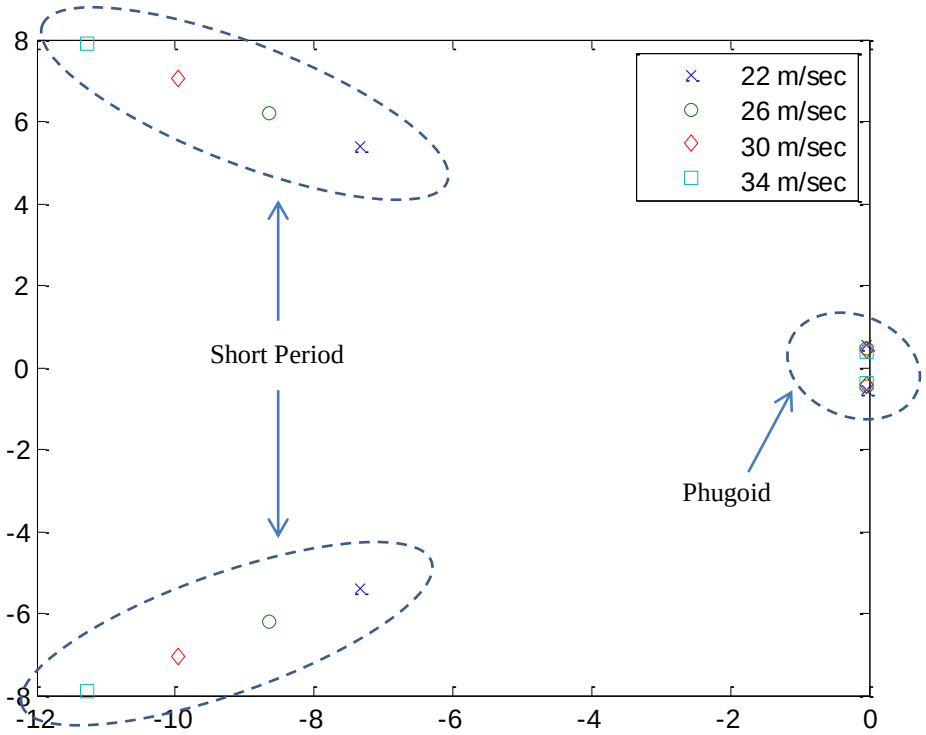

Figure 4-5 Longitudinal Eigenvalues Plot at Different Velocities

The eigenvalues for the lateral modes at different velocities in shown in Figure 4-6. The dutch roll mode decay is almost invariant to velocity variation, while the frequency of oscillation is increasing with velocity. The roll subsidence mode becomes substantially faster with increase in velocity and the third mode spiral divergence is almost invariant to velocity changes.

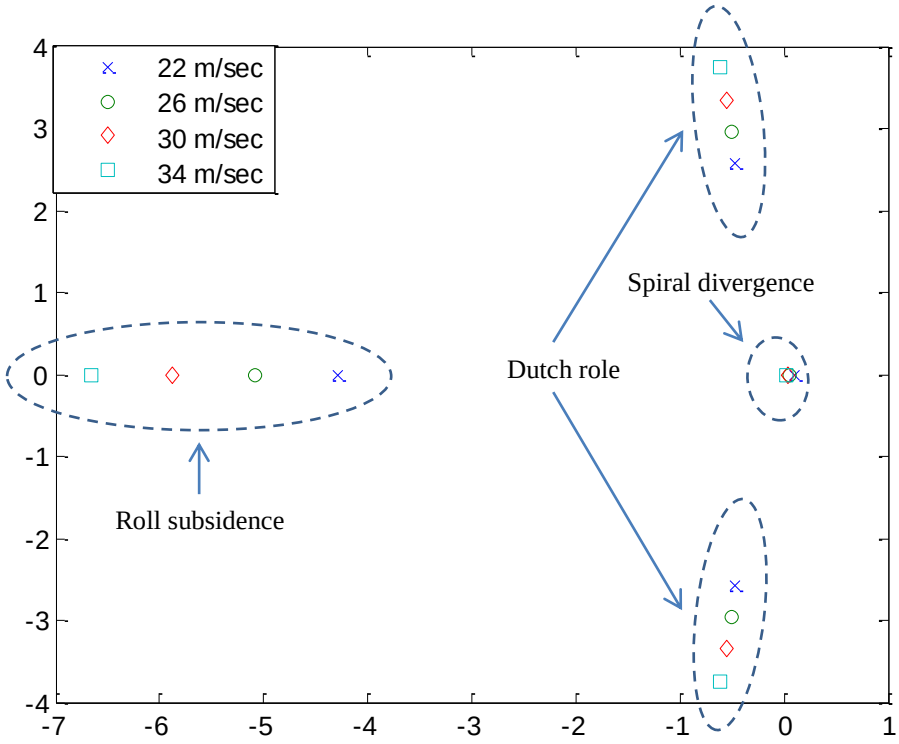

Figure 4-6 Lateral Eigenvalues Plot at Different Velocities

4.8 Summary

Using the concepts and principles presented in chapter three an improved mathematical model of the X-RAE1 UAV has been implemented. A combination of static wind-tunnel tests and ESDU data sheets facilitated the formation of the aerodynamic characteristics of the UAV which in turn was used to develop the linearised model for straight level flight at different velocities. The validity of the longitudinal and lateral models were checked by comparing the linearised responses against the non-linear models. The linearised models were used to assess the UAVs trim, stability and control properties at different velocities and also to design the flight control system in chapter five.

CHAPTER

5

Flight Control Design

Many techniques are available for MIMO robust control design which has been developed in the last few decades. Typically, these techniques rely on advanced optimisation and modelling methodologies (including modelling of uncertainty and robust control) and produce advantages over classical methods by achieving improved performance, efficiency, and tight design simplification utilising available technology. In this chapter, an introduction to control design of multivariable systems and the various trade-offs set by the designer is initially given. This is followed by a brief survey of available control design techniques, in particular the two techniques LQR and H∞ optimisation with Loop Shaping Design Procedure (LSDP) (McFarlane and Glover, 1992). These two methods are used to design simple control schemes for a linearised model of the X-RAE1 UAV corresponding to various flight conditions. The effectiveness and limitations of the two design methods is finally discussed based on the obtained sets of simulation results.

It should be noted that the models used throughout this chapter both for control and simulation purposes arise from linearisation and as such do not address the manoeuvrability capabilities of the design.

5.1 Trade-offs in MIMO Feedback Design

The shaping of multivariable frequency-response characteristics requires a generalisation of the classical definition of gain of SISO systems. This is achieved by manipulating the frequency-response characteristics singular values of the (matrix) transfer functions of the open or closed-loop system. By multivariable transfer function shaping, therefore, we mean the frequency-shaping of singular values of appropriately-specified transfer functions such as the open-loop transfer function or possibly one or more closed-loop transfer functions (e.g. sensitivity, complementary sensitivity, control sensitivity, etc.).

In February 1981, the IEEE Transactions on Automatic Control published a Special Issue on Linear Multivariable Control Systems, the first six papers of which were on the use of singular values in the analysis and design of multivariable feedback systems. The paper by Doyle and Stein (Doyle and Stein, 1981) was particularly influential: it was primarily concerned with the fundamental question of how to achieve the benefits of feedback in the presence of unstructured uncertainty, and through the use of singular values it showed how the classical loop-shaping ideas of feedback design could be generalised to multivariable systems.

The one degree-of-freedom configuration shown in Figure 5-1 shows the plant G and controller K interconnection is driven by reference commands r output disturbances d, and measurement noise n. y are the outputs to be controlled, and u are the control signals.

By defining the sensitivity and complementary sensitivity functions $S = (I + GK)^{-1}$ and $T = GK\left(I + GK\right)^{-1} = I - S$, respectively. Then, we have the following important relationship:

$$y(s) = T(s)r(s) + S(s)d(s) - T(s)n(s) \tag{5.1}$$

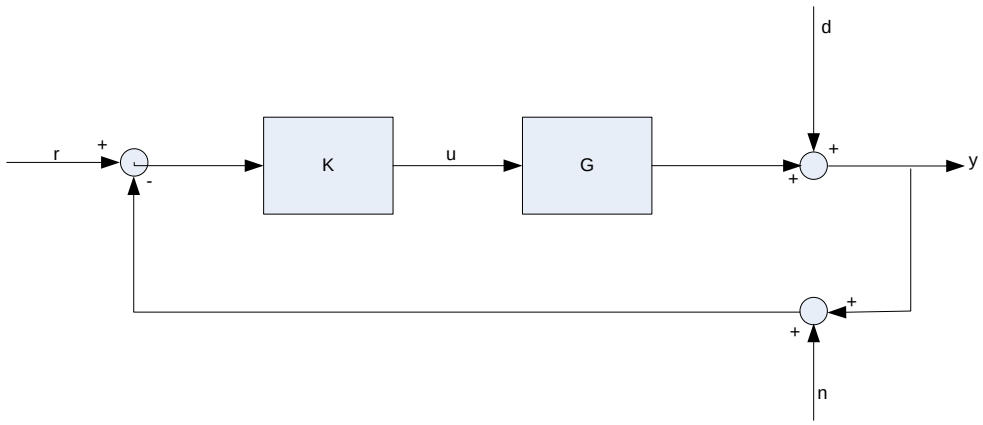

Figure 5-1 One Degree-of-Freedom Feedback Configuration

This relationship determines several closed-loop objectives, which must be satisfied in addition to the requirement that K stabilises G, namely:

1. For disturbance rejection in a specific frequency range (typically a low-frequency interval $[0, \omega_l]$, the largest singular value of $S(j\omega)$ should be made "small" in that range.

2. For noise attenuation in a specific frequency range (typically a high-frequency interval $[\omega_h, \infty)$, the largest singular value of $T_0(j\omega)$ should be "small" in that range. This is equivalent to fast "roll-off" of the open-loop frequency response characteristics.

3. For reference tracking up to a certain frequency ω_0, the smallest singular value of $T_0(j\omega)$ should be approximately 1 up to that frequency.

4. For control energy reduction in a specific frequency range the largest singular value of the control-sensitivity function $KS(j\omega)$ should be "small" in that range.

5. If the unstructured uncertainty in the plant model $G_\Delta(s)$ is represented by an additive perturbation, i.e. $G_\Delta(s) = G(s) + W_1(s)\Delta(s)W_2(s)$, $\|\Delta(s)\|_\infty \leq 1$ (in which $W_1(s)$ and $W_2(s)$ are suitable weighting functions), then a further closed-loop objective which guarantees robust stability is:

$\|W_2(s)K(s)S(s)W_1(s)\|_\infty < 1$. Thus, in the frequency range where the gain of the uncertainty is "large", the gain of the control-sensitivity function should be sufficiently small to guarantee robust stability in the face of additive perturbations.

6. If the uncertainty is modelled by an output-multiplicative perturbation (for example uncertainty arising in the sensor dynamics), $G_\Delta(s) = (I + W_1(s)\Delta(s)W_2(s))G_0(s)$, where $\|\Delta(s)\|_\infty < 1$, then robust stability is guaranteed (subject to nominal closed-loop stability) if $\|W_2(s)\mathrm{T}_0 W_1(s)\|_\infty < 1$, where $T_0(s) = GK(I + GK)^{-1}$. Alternatively, if the uncertainty is modelled by an input-multiplicative perturbation (for example uncertainty arising in the actuator dynamics), $G_\Delta(s) = G(s)(I + W_1(s)\Delta(s)W_2(s))$, where $\|\Delta(s)\|_\infty < 1$, then robust stability is guaranteed (subject to nominal closed-loop stability) if $\|W_2(s)T_i W_1(s)\|_\infty < 1$, where $T_i(s) = KG(I + KG)^{-1}$.

The closed-loop requirements 1 to 6 cannot all be satisfied simultaneously over all frequencies. Feedback design is therefore a trade-off over frequency of conflicting objectives. This is not always as difficult because the frequency ranges over which the objectives are important can be quite different. For example, disturbance rejection is typically a low frequency requirement, while noise mitigation is often only relevant at higher frequencies. In terms of open-loop gain:

1. For disturbance rejection we need to make $\underline{\sigma}(GK)$ large; valid for frequencies at which $\underline{\sigma}(GK) \gg 1$.

2. For noise attenuation we should make $\bar{\sigma}(GK)$ small; valid for frequencies at which $\bar{\sigma}(GK) \ll 1$.

3. For reference tracking we should make $\underline{\sigma}(GK)$ large; valid for frequencies at which $\underline{\sigma}(GK) \gg 1$.

4. For control energy reduction we should make $\bar{\sigma}(GK)$ small; valid for frequencies at which $\bar{\sigma}(GK) \ll 1$.

5. For robust stability to an additive perturbation we should make $\bar{\sigma}(GK)$ small; valid for frequencies at which $\bar{\sigma}(GK) \ll 1$.

6. For robust stability to a multiplicative output perturbation we should make $\bar{\sigma}(GK)$ small; valid for frequencies at which $\bar{\sigma}(GK) \ll 1$.

From Figure 5-2, it follows that the control engineer must design K so that $\bar{\sigma}(GK)$ and $\underline{\sigma}(GK)$ avoid the shaded regions. That is, for good performance, $\underline{\sigma}(GK)$ must be made to lie above a performance boundary for all ω up to ω_l, and for robust stability $\bar{\sigma}(GK)$ must be forced below a robustness boundary for all types of uncertainty models that apply to the design situation . An additional complication of the design is that the transition between the high-gain and low-gain region (in the "cross-over" region) should not be very fast, as this tends to decrease the phase-margin of the design as a result of Bode's hain-phase integral relation (Skogestad and Postlethwaite, 2005).

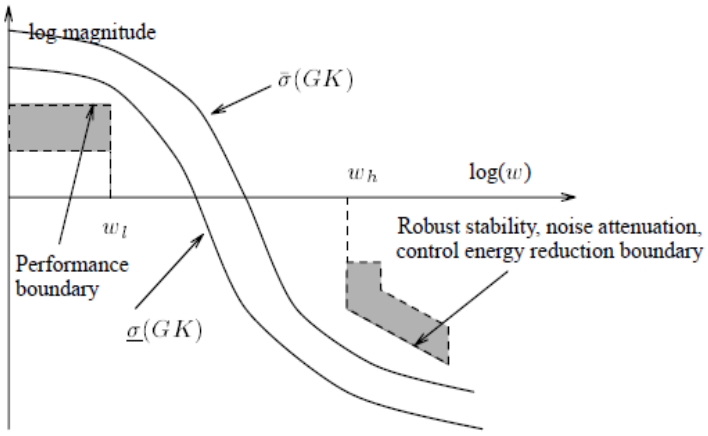

Figure 5-2 Design Trade-Offs for the Multivariable Loop Transfer Function GK (Skogestad and Postlethwaite, 2005)

5.2 Design Techniques

The following section outlines a number of widely-used techniques such as, pole-placement, Linear-Quadratic Regulator (LQR), Linear Quadratic Gaussian (LQG) control and H_∞ optimal control.

5.2.1 Pole Placement

As the locations of the poles of a system strongly affect its dynamic (transient) response, one way of modifying the characteristics of the system (under state-feedback) is to place the poles of the closed loop system at desired locations. The technique is called pole placement. It can be shown that if the system is controllable, the poles of the closed-loop system can be placed at arbitrary locations (provided they are symmetric with respect to the real axis). This is a very strong result which shows that under controllability the designer has complete freedom in modifying system's dynamics. Of course, this does not take into account constraints on the magnitude/energy of the required control signal and other practical considerations.

To illustrate the procedure, assume that $u(t) = r(t) - Kx(t)$, where r is a reference input, $u\ t$ is the control input and K is a gain (state-feedback) matrix. Under closed-loop control,

$$\dot{x}(t) = Ax(t) + Bu(t) = Ax(t) + B(r(t) - Kx(t)) = (A - BK)x(t) + Br(t) \qquad (5.2)$$

and hence the closed-loop dynamics are now described by the eigenvalues of $A - BK$. Thus the aim is thus to pick K so that the eigenvalues of $A - BK$ have the desired properties. If, for example, we want to stabilise A, we need to pick K so that $A - BK$ is stable (all eigenvalues have negative real part). If, in addition, we want to increase the damping of the system, all eigenvalues of $A - BK$ must be placed in the highly-damped region of the left-half plane. A standard procedure for obtaining the required gain matrix for SISO system is via Ackermann's formula (Antsaklis and Michel, 1997):

$$K = [0...01]\Gamma_c^{-1}\Phi_d(A) \tag{5.3}$$

where,

$$\Gamma_c = \begin{bmatrix} B & AB & \dots & A^{N-1}B \end{bmatrix} \tag{5.4}$$

and $\Phi_d(s)$ denotes the required characteristic polynomial of the closed-loop system evaluated at $s = A$. Note that Γ_c is assumed to be invertible, i.e. (A, B) must be controllable, and $N = dim(A)$.

5.2.2 Eigen-Structure Assignment

Eigen-structure Assignment is basically an extension of pole-placement method. It allows the designer to assign the closed-loop eigenvalues (poles) and to assign the eigenvectors or parts of them, within certain limits. Through the assignment of eigenvectors, the zeros of the transfer functions can be influenced and coupling and decoupling of states and modes can be addressed directly. Although the standard technique takes performance and decoupling into account, it does not address robustness. Eigen-structure assignment is most useful as a tool within a fuller design environment, hence allowing the attainment of good performance, decoupling and robustness in the resulting control system.

5.2.3 Multi-Objective Parameter Synthesis

Multi-objective parameter synthesis (MOPS) is a general technique which complements a chosen control law synthesis technique (Joos, 1997). Having chosen an application-specific control law structure with parameterisation, or having chosen a general control synthesis technique with its analytically given parameterisation, the free design parameters (e.g. the weights) are computed by a min-max parameter optimisation set up. The designer formulates this set up by specifying the design goals as a set of well-defined computational criteria, which can be a function of stability parameters (e.g. eigenvalues), and time- and frequency response characteristics (e.g. step-response overshoot and settling time, control rates, bandwidth, stability margins etc.). Using this multi-

criteria formulation all the various conflicting design goals are taken care of individually, nonetheless are compromised concurrently by a weighted min-max parameter optimisation. In particular, robust-control requirements with respect to variations in structured parameter sets and operating conditions can be taken care of by a multi- model formulation which encompasses the worst-case design conditions.

5.2.4 Quantitative Feedback Theory

Quantitative Feedback Theory (QFT) is a graphical classical frequency domain control system design methodology that was developed by (Horowitz and Baños, 2001). It is based on the Nichols chart and uses a TDF structure for the controller. The method is restricted to compensating a single loop at a time, while worst-case disturbance/uncertainty-modelling assumptions are made for other loops. The method typically results in low-order diagonal feedback controllers.

5.2.5 Linear Quadratic Regulator (LQR)-Optimal Control

Optimal control methods are control design techniques which provide "the best possible" (optimal) solution to an optimisation problem. Thus, in pole placement the aim is normally to stabilise a system, whereas in optimal control the objective is to optimise a performance index (while still keeping the system stable).

LQR (Linear quadratic regulator) is an optimisation method involving a quadratic objective function, corresponding to the weighted energy of all regulated and control variables. In the case of active control design, this formulation gives the designer sufficient flexibility to include all relevant design objectives, related to the state and control variables.

Assume that the plant to be controlled has a state space realisation:

$$\dot{x}(t) = Ax(t) + Bu(t)$$
$$y(t) = Cx(t) + Du(t)$$

The objective in LQR is to select the control input $u\ t$ that minimises the performance index:

$$J_{lqr} = \lim_{T\to\infty} \int_0^T (x^T Qx + u^T Ru)dt \tag{5.5}$$

over all control signals $u\ t$.

In the above formulation it is required to minimise a performance index consisting of (weighted) energy terms involving the state-variables and the control signals. Thus the performance index balances transient-performance requirements ("fast" state-variables' decay) with control-effort constraints (control energy remains "small"). Normally, the matrices *Q* and *R* represent design parameters which shift the emphasis between these two (typically conflicting) objectives. High values in the elements of *Q* (relative to those of *R*) places more emphasis on system performance (dynamic response), and vice-versa.

In practical designs *Q* is often selected as a non-negative diagonal matrix whose elements reflect the "cost" of each individual state and their chosen values are adjusted according to simulation results and the state feedback gains of the design. Similarly *R* is also chosen normally as a diagonal matrix with positive elements which are selected according to the pick values or energies of the corresponding control signals. For a detailed methodology for the choice of these weights see (Maciejowski, 1989).

The standard assumptions of the general LQR problem are as follows:

1. The weighting matrices satisfy $Q = Q^T \geq 0$ and $R = R^T > 0$;
2. The pair (*A*,*B*) is stabilisable; and,
3. The pair (*A*,*Q*) is detectable.

Under these assumptions, the optimal controller is obtained in the form $u(t) = -K_c x(t)$, where K_c is the optimal state-feedback gain, given by:

$$K_c = R^{-1} B^T P_c \tag{5.6}$$

and P_c is the stabilising solution of the algebraic Riccati equation:

$$A^T P_c + P_c A - P_c B R^{-1} B^T P_c + Q = 0 \tag{5.7}$$

Here "stabilising" refers to the solution for which the closed-loop "*A*" matrix $A_c = A - BR^{-1}B^T P_c$ is asymptotically stable. It can be shown that under the stated conditions P_c is unique, symmetric and positive semi-definite matrix. Apart from stabilising the system, it may be shown that LQR controllers are also guaranteed to have good gain and phase stability margins (Maciejowski, 1989).

5.2.6 Linear Quadratic Gaussian (LQG) Control

The main assumption of LQR is that all state-variables are measurable, which clearly is unrealistic in practice. This is removed by using LQG control (Linear-Quadratic-Gaussian), which is a generalisation of LQR and poses the design problem in a stochastic framework.

In LQG external disturbances are modelled as (filtered) white noise signals, while the objective function to be minimised is a stochastic version of the one used in LQR control. LQG removes the LQR assumption that all states are measurable; instead noisy measurements are assumed, and the overall problem decomposes to two separate sub-problems involving optimal estimation of the state-variables and optimal regulation ("separation" or "certainty-equivalence" principle). This is especially convenient for the designer, since the regulator part of the design remains unaffected. The optimal estimator ("Kalman filter") gives rise to a dynamic

controller and is essentially an optimal observer, achieving a balance between the effects of disturbance and sensor-noise signals.

LQG control is a well-established design method, which has been applied successfully in many application domains. Computationally, it is easy to implement (requiring the off-line solution of two algebraic Riccati equations), while the weighting functions can be "tuned" in a systematic way to shift the emphasis between the various objectives included in the quadratic cost function. As mentioned earlier, LQR provides the design automatically with excellent stability margins. Unfortunately, these are no longer guaranteed when the Kalman filter is implemented, although various techniques are available to partially recover them and inject some measure of robustness into the design (Loop Transfer Recovery) (Maciejowski, 1989).

The state space equation describing the plant is similar to the LQR formulation, with the addition of two white noise terms, representing process and measurement noise:

$$\begin{aligned} \dot{x}(t) &= Ax(t) + Bu(t) + Ew(t) \\ y(t) &= Cx(t) + Du(t) + v(t) \end{aligned} \tag{5.8}$$

Here $w(t)$ and $v(t)$ are zero-mean stochastic processes, uncorrelated in time (white noise) with known covariance matrices. The initial state is also assumed to be a random vector, with known mean and covariance matrix, and uncorrelated with both $w(t)$ and $v(t)$. The stochastic version of the problem is to find the optimal control signal which minimises the performance index:

$$J_{lqg} = E\left\{\int_0^\infty (x^T Qx + u^T Ru)dt\right\} \tag{5.9}$$

Where $E(\cdot)$ denotes statistical expectation, under the standard assumptions of stabilisability of (A,B), detectability of (A,C) and positive semi-definiteness (positive-definiteness) of Q (R). The problem is divided into two sub-problems: the

first sub-problem is to obtain the optimal estimator, which minimises the root mean-square value of the state-estimation error, i.e.

$$\min E\{(x-\hat{x})^T(x-\hat{x})\} \tag{5.10}$$

This is solved by the Kalman filter (Davis and Vinter, 1985):

$$\frac{d\dot{\hat{x}}}{dt} = A\hat{x} + Bu + L(y - C\hat{x} - Du) \tag{5.11}$$

in which L is the optimal Kalman gain, defined from the solution of an algebraic Riccati equation involving the covariance matrices of v and w; this is actually of the dual form to the algebraic Riccati equation used in the solution of the LQR problem. The second sub-problem involves the solution to the optimal regulator's gain and is identical to the solution of the LQR problem (with all stochastic terms removed). The separation (certainty equivalence) principle guarantees that this decomposition into two separate sub-problems still gives the overall optimal solution to the original problem.

A drawback of this theory is that it may have poor stability margins (the excellent stability margins guaranteed for the LQR controller no longer apply) and therefore several design modifications have been introduced to improve the system robustness (loop-transfer recovery (Maciejowski, 1989)). Furthermore, since the Kalman filter replicates the dynamics of the plant, the general issue of model uncertainty and robustness becomes critical. Note that all uncertainties are represented in LQG as noise signals affecting the process dynamics or the measurements, which may not be realistic in practice. Despite these limitations LQG methods have a sound mathematical foundation and have proved effective in many practical designs; overall they produce very good results that are difficult to obtain with classical control methods.

The LQG problem is equivalent to the so-called "H_2 optimal control problem". The aim of this problem is to find a proper real-rational controller $K\ s$ that stabilises the

plant $G(s)$ internally and minimises the H_2 norm of the transfer matrix $T_{zw}(s)$ between *w* (disturbances) and *z* (regulated signals). The formulation and solution of the H_2 problem is different from LQR but essentially the *two problems are identical***.**

5.2.7 H_∞ Optimal Control: Mixed Sensitivity Problem

The Mixed Sensitivity problem is a standard formulation of the general H_∞ optimisation problem. The problem is to design a feedback controller which minimises the ∞-norm of an augmented matrix consisting of the closed-loop sensitivity function S_o and the control sensitivity function $K\ s$, each suitably weighted by input and output weighting functions

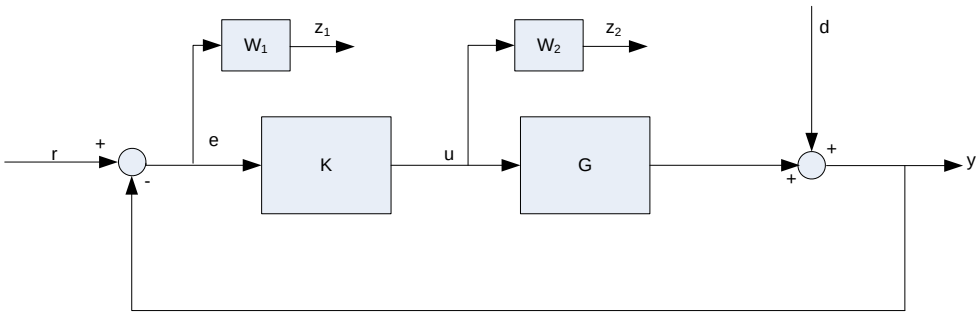

Figure 5-3 H_∞ Mixed Sensitivity Closed-Loop Feedback System with Weights

Figure 5-3 shows a closed loop feedback system with reference input r , output y , output disturbance d , error signal e , control signal *u* and the weights W_1 and W_2 . To achieve small tracking error, good transient behaviour and (sufficiently) high bandwidth the output sensitivity needs to be small at low frequencies which can be achieved by designing K to have high gain at these frequencies. Conversely, the high-frequency open loop gain should "roll-off" at high frequencies to limit the closed-loop bandwidth, and thus reduce sensor noise amplification and meet robust-stability requirements. In order to meet the low and high frequency conditions, the design will incorporate frequency dependent weights. These

weights W_1 and W_2 can be chosen to give the bounds on the terms S_o and KS_o required to achieve the required high and low frequency gains. In fact W_1 needs to be a low pass filter whilst W_2 needs to be a high pass filter. Broadly speaking, W_1 and W_2 determine the performance and robustness properties, respectively. Weight selection can be made to account for model uncertainty. If model uncertainty is unspecified, then the weight selection is broadly defined by relative stability and nominal performance requirements. The H_∞ optimisation can then be solved to find a stabilising controller K which is proper and minimises the peak of the largest singular value (over frequency) of the transfer function from the exogenous inputs to the regulated signals, which achieves the desired frequency shaping of the closed-loop characteristic responses. The optimal H_∞ optimisation solution is obtained by an iterative process over pre-specified upper and lower bounds.

5.2.8 H_∞ Loop-Shaping

H_∞ loop-shaping is another standard design paradigm of the general H_∞ optimisation problem. It was developed by McFarlane and Glover (McFarlane and Glover, 1992). Loop-shaping is an intuitive method for designing robust controllers which mimics classical design, as the notions of classical loop-shaping readily carry through. The designer can achieve closed loop requirements, such as disturbance and noise rejection, by shaping directly the open-loop gains. An important feature of H_∞ loop-shaping is that it enables the designer to push for the best achievable closed loop performance subject to a required level of robustness. This is because the designer has control over the cross-over frequencies of the loop gain singular values.

In general, when setting up a robust control problem a decision has to be made about the type of uncertainty to be used. This can be difficult as it requires good knowledge of the system model. Robust stability to coprime factor uncertainty, on which the method is based on, requires few assumptions to be made about the open-loop stability of the perturbed system model. Coprime factor uncertainty is a general type of uncertainty-model similar to the single-input single-output (SISO) uncertainty measures of gain and phase

margins. When there is little detailed knowledge about the uncertainty present in a system model, H_∞ loop-shaping is a good method for designing robust controllers.

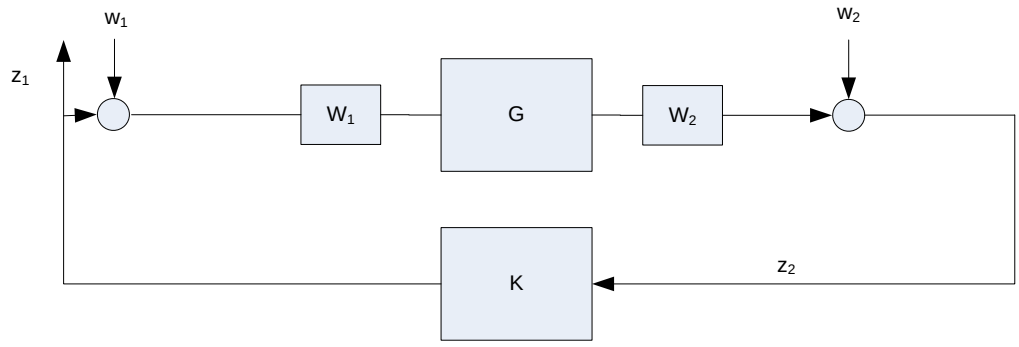

Figure 5-4 H_∞ Loop-Shaping Standard Block Diagram

Performance is specified by shaping the singular values of the system model G with weights W_1 and W_2 as shown in Figure 5-4. Usually integral actions introduced via either W_1 or W_2 to enforce zero sensitivity at zero frequency and thus zero steady-state error to step references or asymptotic rejection of step disturbances. The frequency characteristics of the weights also need to ensure that the gain roll-off rate near the crossover frequency is sufficiently small to ensure an adequate phase margin. For a detailed design methodology see (Skogestad and Postlethwaite, 2005). It is ensured that there are no left half plane pole/zero cancellations between controller K and the shaped model $G_s = W_1 G W_2$. This is because K can be written as an exact observer plus state feedback. Hence H_∞ loop-shaping controllers can be gain scheduled. Left half plane pole/zero cancellations are undesirable as they can limit the achievable robust performance. In addition, with loop-shaping the cost function minimised automatically enforces some levels of robust stability, while the solution requires no iterations.

5.3 X-RAE1 Longitudinal Control System Design

Two techniques have been selected to be implemented and compared. These are LQR and H_∞ optimisation with Loop-Shaping Design Procedure (LSDP), which was proposed by Glover and McFarlane (McFarlane and Glover, 1992, McFarlane and Glover, 1989). The two methods selected are popular in aero applications. The first (LQR) emphasises the trade-off between performance and robustness using control versus state weighting via the performance index *J*. The later, H_∞ loop shaping, mimics classical loop-shaping control and can deal directly with the effects of unstructured uncertainty in the model. Both design methods share the following characteristics:

- Reliance on powerful mathematical theory
- Systematic and simple application procedures
- Good history of real applications
- Clear and logical design steps that are similar to classical methods
- Developed and applied by leading British professionals for the last decade
- Well-developed tools and published literature
- Modified and extended for different application situations

The flight controller is assessed for a step height demand from the steady state flight condition. The target design specifications are:

- Asymptotic steady state error less than 10%, ideally zero
- Rising time less than 1 second
- Overshoot less that 10%
- Settling time within 5 seconds
- Realistic elevator deflection and throttle setting
- Small deviation of these characteristics for all velocities in the operating range (25 m/sec – 35 m/sec)

The design of the longitudinal controller will be applied to the X-RAE1 UAV during straight flight at 30 m/s. The longitudinal model of X-RAE1 can be represented by the following perturbed linear state-space equations:

$$\begin{aligned} \dot{x}(t) &= Ax(t) + Bu(t) \\ y(t) &= Cx(t) + Du(t) \end{aligned} \tag{5.12}$$

$$\begin{bmatrix} \dot{u} \\ \dot{w} \\ \dot{q} \\ \dot{\theta} \\ \dot{h} \end{bmatrix} = \begin{bmatrix} -0.1420 & -0.2270 & 2.4928 & -9.7709 & 0 \\ -1.0331 & -4.4763 & 28.6389 & 0.8367 & 0 \\ -0.0419 & -2.7441 & -15.3512 & -0.1343 & 0 \\ 0 & 0 & 1.0000 & 0 & 0 \\ 0 & -1.0000 & 0 & 29.8872 & 0 \end{bmatrix} \begin{bmatrix} u \\ w \\ q \\ \theta \\ h \end{bmatrix} + \begin{bmatrix} -1.1357 & 1.4441 \\ -13.0599 & 0 \\ -137.1565 & -2.0355 \\ 0 & 0 \\ 0 & 0 \end{bmatrix} \begin{bmatrix} \eta \\ \delta_T \end{bmatrix}$$

$$y = \begin{bmatrix} 1 & 0 & 0 & 0 & 0 \\ 0 & 0 & 1 & 0 & 0 \\ 0 & 0 & 0 & 1 & 0 \\ 0 & 0 & 0 & 0 & 1 \end{bmatrix} \begin{bmatrix} u \\ w \\ q \\ \theta \\ h \end{bmatrix} \tag{5.13}$$

Where the five states and two inputs are defined as:

u is the forward velocity

w is the downward velocity

q is the pitch rate

θ is the pitch angle

h is the height

η is the elevator deflection

δ_T is the throttle setting

5.3.1 H_∞ Loop-Shaping Design

The main objective of LSDP is to produce a controller that guarantees robust stability against normalised coprime factor uncertainty. This form of uncertainty was used by McFarlane and Glover (McFarlane and Glover, 1992, McFarlane and Glover, 1989) to obtain an exact solution to the robust stabilisation problem. With this method, the designer shapes the model G with pre- and post-weighting filters to achieve performance objectives, similar to classical control. Next, a robust stabilisation problem is solved for the shaped plant, resulting in a feedback controller. The final controller used in the design is obtained by absorbing the plant weights by the feedback controller.

Thus, LSDP is a two stage process. First, the open-loop system nominal linear model is augmented by pre- and post-compensators (weights) to give a desired shape to the singular values of the open-loop frequency response, i.e. high gain at low frequency for good command tracking and low gain at high frequency for noise and disturbance rejection. The nominal model G and shaping functions W_1, W_2 are then combined to form the shaped model, G_S where $G_S = W_2 G W_1$ (Adams, 1994).

The resulting shaped system is then "robustly" stabilised with respect to the left coprime factor uncertainty using H_∞ optimisation and the stabilising central controller, K_∞ is synthesised. The final feedback controller K is then constructed by combining K_∞ with the shaping functions W_1 and W_2.

Scaling and feedback selection can be included in to G according to the desired output decoupling as illustrated in Figure 5-5. At the input, the system model is scaled according to relative actuators usage and capability, where B_S is the input scaling matrix. J_x is the output feedback selection matrix and allows the designer to select the required states for feedback prior to the output scaling C_S.

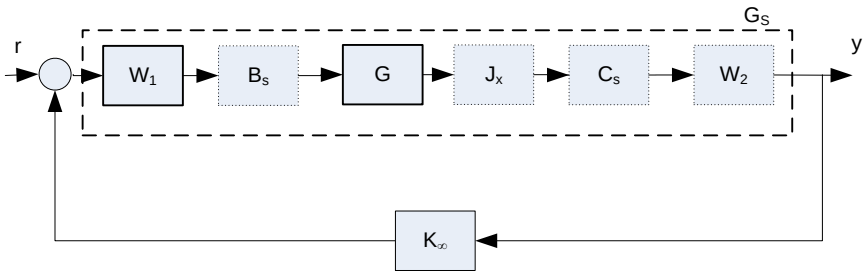

Figure 5-5 Scaled and Shaped System Model G_S

For the X-RAE1 model no input or output scaling and no post-weight W_2 is used. This is accomplished by setting B_S to I_{2x2} and J_x, C_S W_2 to I_{4x4} correspondingly. Feedback selection is present, but is encapsulated in G, where the download velocity w state is filtered out.

The pre-weight W_1 includes integrators to boost the low frequency gain. This ensures zero stead-state tracking error, disturbance rejection and output decoupling.

$$W_1 = \frac{s+1}{s} I_{2x2} \tag{5.14}$$

Figure 5-6 shows how W_1 has altered the open loop system G singular values by increasing the slope by 20db/decade at low frequencies due to the introduction of the extra integral action. At high frequencies the singular values characteristics of shaped and unshaped plants are almost identical.

The resulting sub-optimal robust stability margin is $\varepsilon = 0.252$ and $\gamma = 3.97$, which is just on the margin of success $\varepsilon > 0.25$ or $\gamma > 4$ (Skogestad and Postlethwaite, 2005).

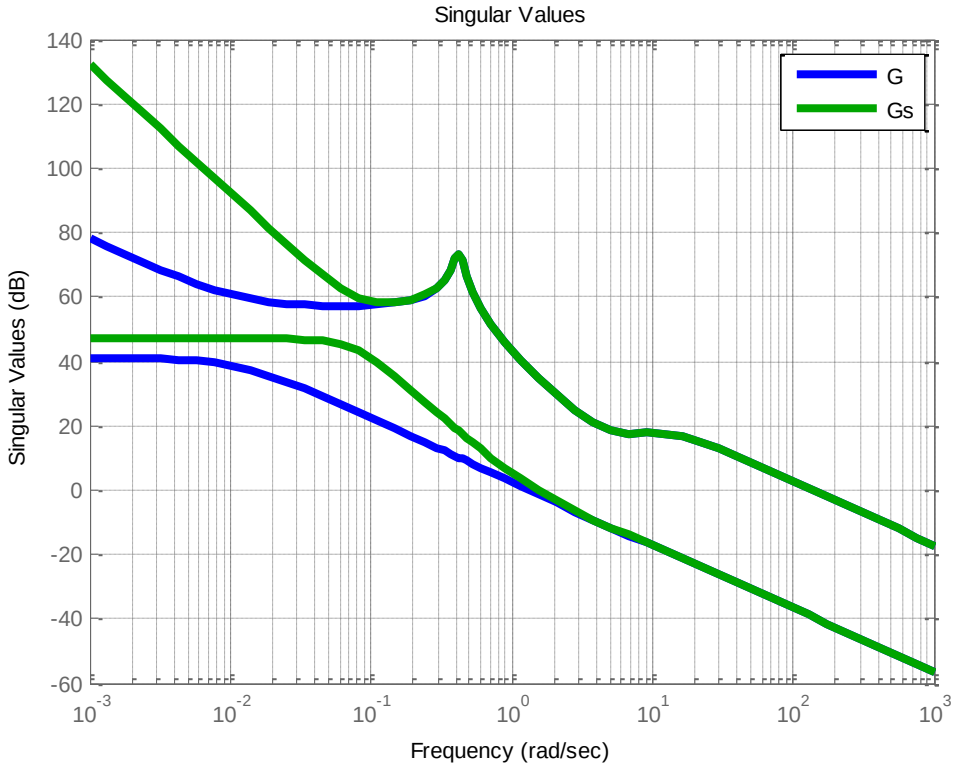

Figure 5-6 Controller effect on the open loop system G

The controller can be implemented in several ways, in the forward path, in the feedback path, or in observer form. The constant prefilter K_{pr} in Figure 5-7 ensures a steady state unity gain between r and y and is given by:

$$K_{pr} = K_{\infty}(0)W_2(0) = K_{\infty}(0) \tag{5.15}$$

Where $K_{\infty}(0)$ is the DC gain of the H_{∞} controller.

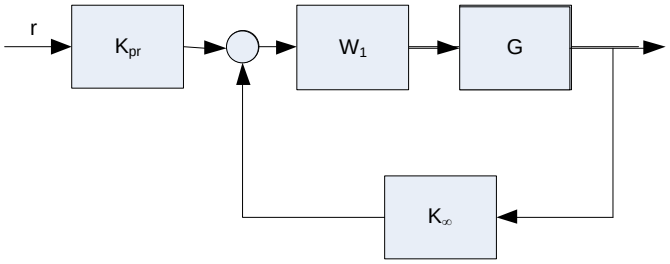

Figure 5-7 Robust controller implementation

5.3.2 LQR Design

The LQR design was based on the equations 5-12 and 5-13. To achieve asymptotic regulation with respect to the height variable the state vector was redefined as $\hat{x} = x - x_{ss}$ where $x_{ss} = \begin{bmatrix} 0 & 0 & 0 & 0 & 1 \end{bmatrix}^T$. The corresponding objective function is

$$J_{lqr} = \lim_{T \to \infty} \int_0^T (\hat{x}^T \hat{x} + u^T u) dt \tag{5.16}$$

minimised over all control signals $u\ t$.

This is schematically shown in Figure 5-8

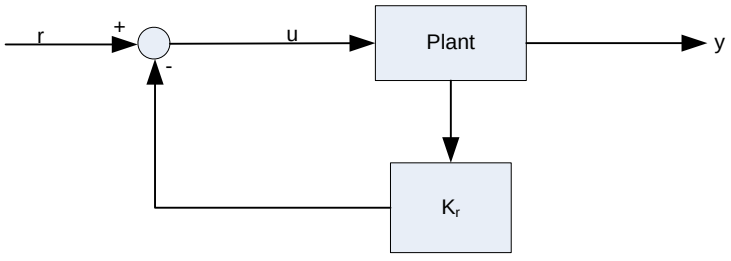

Figure 5-8 LQR Feedback loop

5.4 Comparison Between LQR and H_∞ Control

Both H_∞ and LQR design are very fast, with settling times 2 and 3 seconds correspondingly in the height response. This leads to a significantly large undershoots in the elevator deflection and a also large overshoots in the throttle settings which would be an undesirable practice.

It should be noted however that the model does not include both sensor and actuator dynamics. Sensors and actuators are typically second order under damped systems. Including these dynamics of these devices in the model will limit the effective bandwidth of the system and would result in smother and slower responses and will make the design feasible.

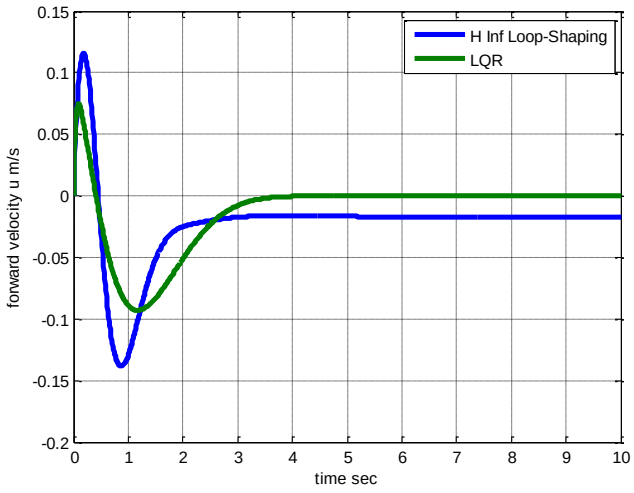

Figure 5-9 H_∞ and LQR responses for forward velocity at 30m/s

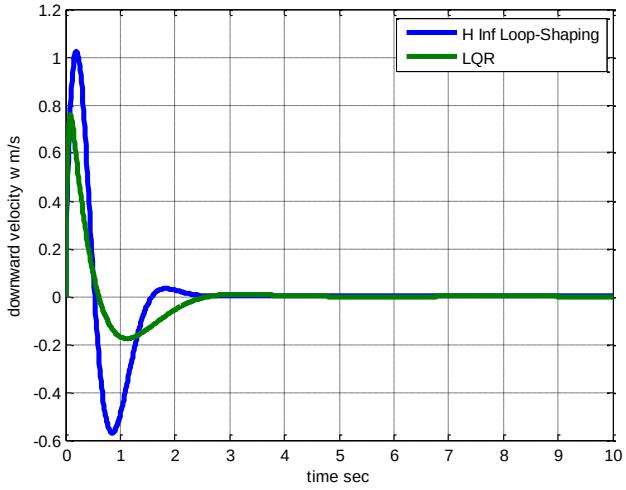

Figure 5-10 H_∞ and LQR responses for downward velocity at 30m/s

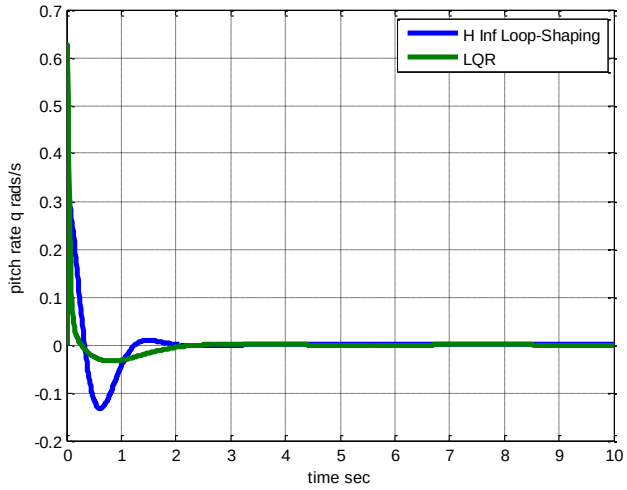

Figure 5-11 H_∞ and LQR responses for pitch rate at 30m/s

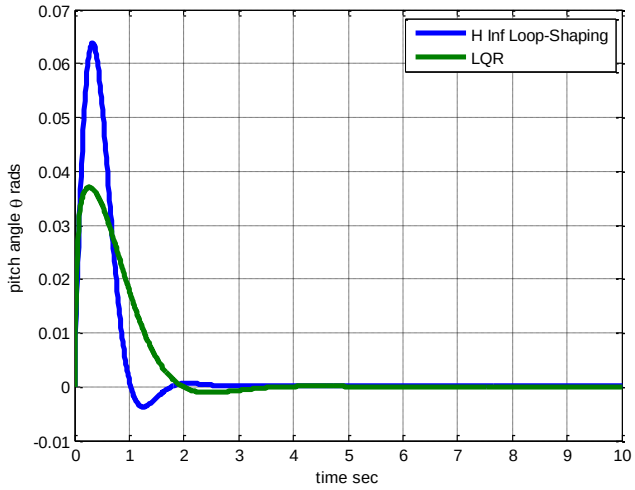

Figure 5-12 H_∞ and LQR responses for pitch angle at 30m/s

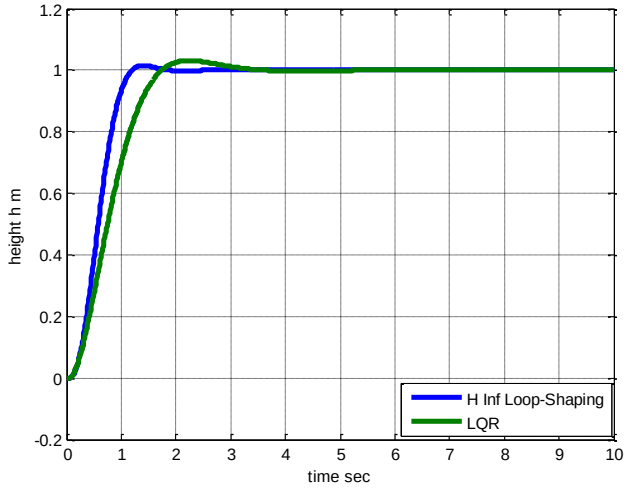

Figure 5-13 H_∞ and LQR responses for height at 30m/s

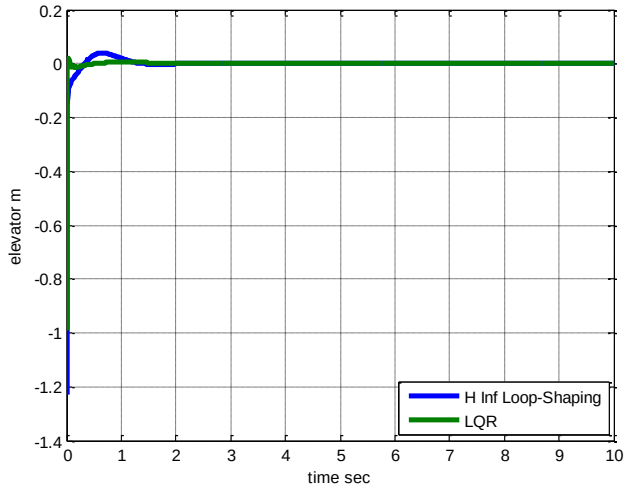

Figure 5-14 H_∞ and LQR responses for elevator at 30m/s

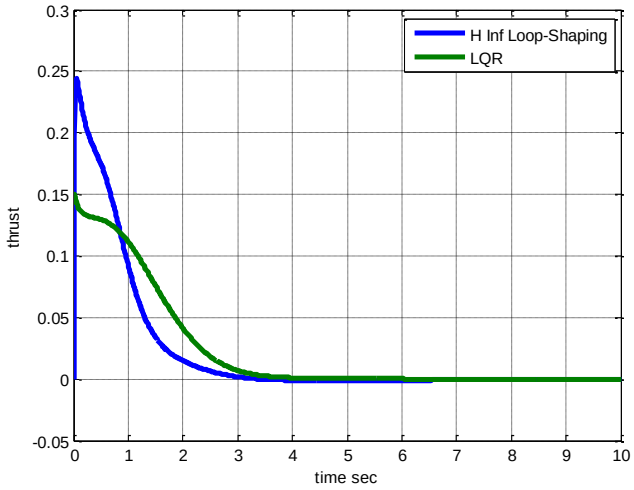

Figure 5-15 H_∞ and LQR responses for throttle at 30m/s

5.5 H_∞ Loop-Shaping and LQR at Different Velocities

In order to examine the robustness of the two designs with respect to speed variations. The following procedure was followed. A H_∞ and LQR controller was designed for a nominal speed of 30 m/s and these were tested on the models corresponding to speeds of 25 and 35 m/s. The simulation results are summarised in Figure 5-16 to Figure 5-22 for H_∞ and Figure 5-22 to Figure 5-29 for LQR. Overall the variation of the results was remarkably low. Since H_∞ design was slightly faster it tends to produce a slightly higher overshoot (about 10%) relative to LQR controller at the same speed. Note however the LQR design is state feedback based

and therefore uses all five state variables whereas the H_∞ controller is this case uses only four out the five state variables. Further improvements in the results can be achieved by scheduling the gains of the two controllers via the speed of the UAV.

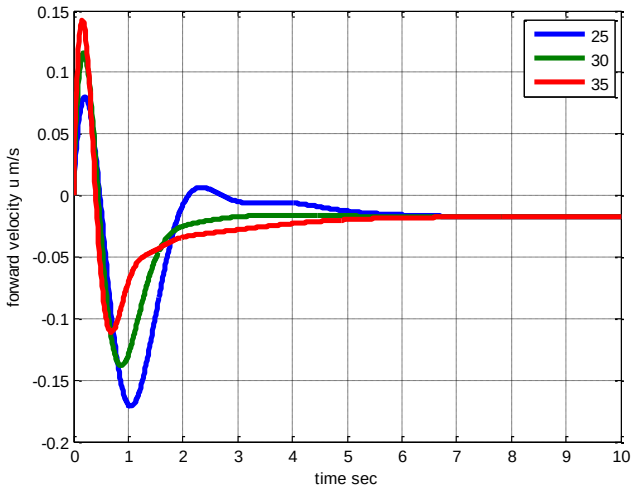

Figure 5-16 H_∞ responses at different velocities for forward velocity

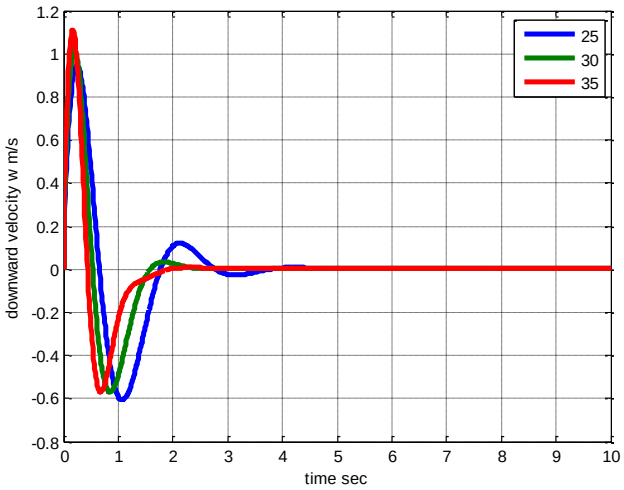

Figure 5-17 H_∞ responses at different velocities for downward velocity

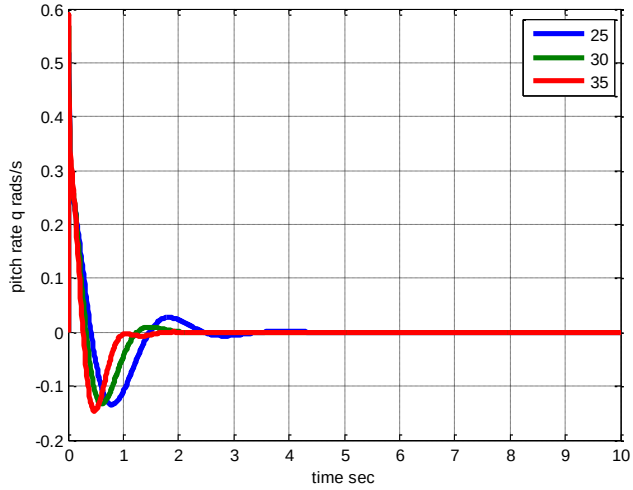

Figure 5-18 H_∞ responses at different velocities for pitch rate

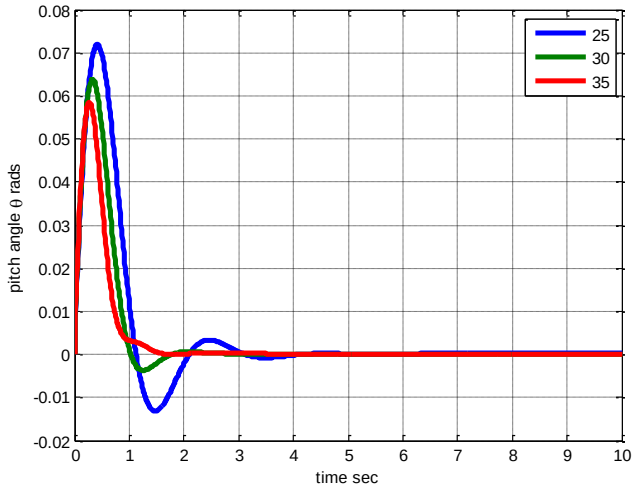

Figure 5-19 H_∞ responses at different velocities for pitch angle

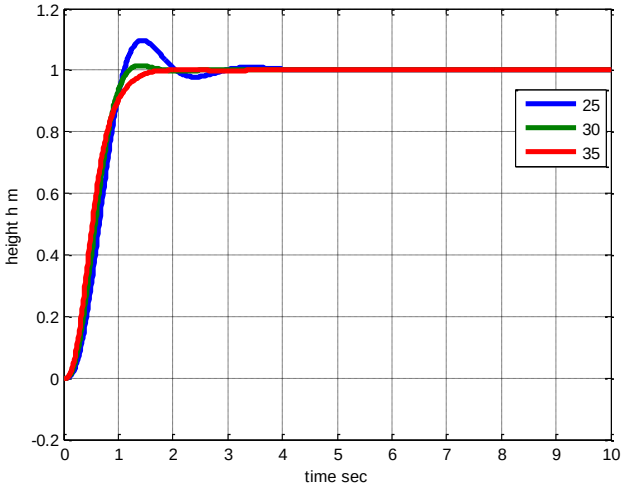

Figure 5-20 H_∞ responses at different velocities for height

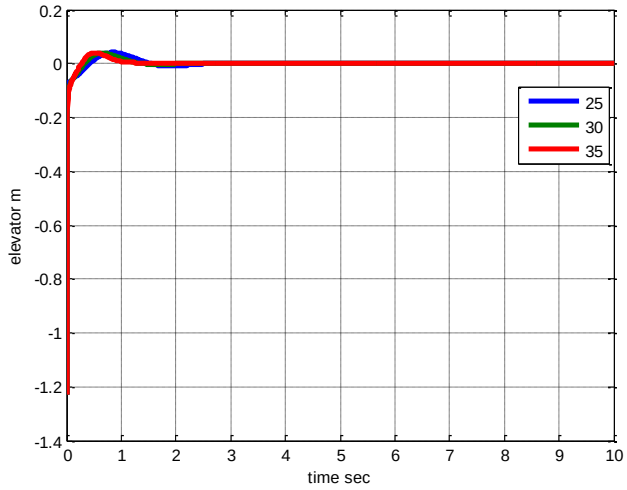

Figure 5-21 H_∞ responses at different velocities for downward elevator

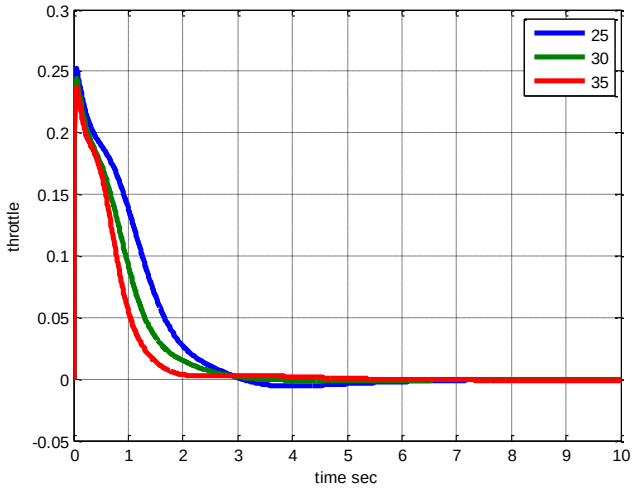

Figure 5-22 H_∞ responses at different velocities for downward throttle

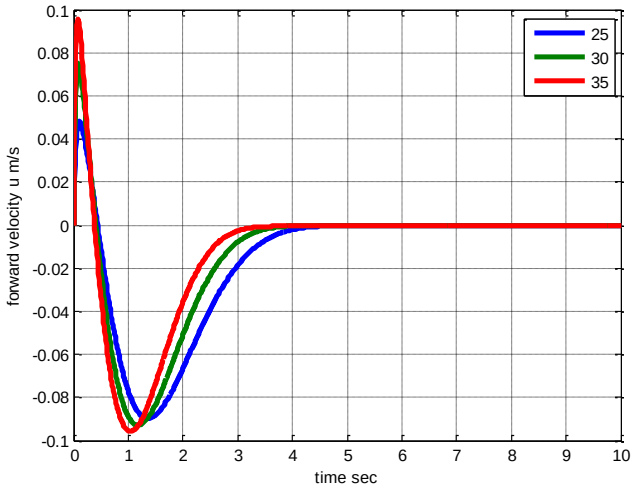

Figure 5-23 LQR responses at different velocities for forward velocity

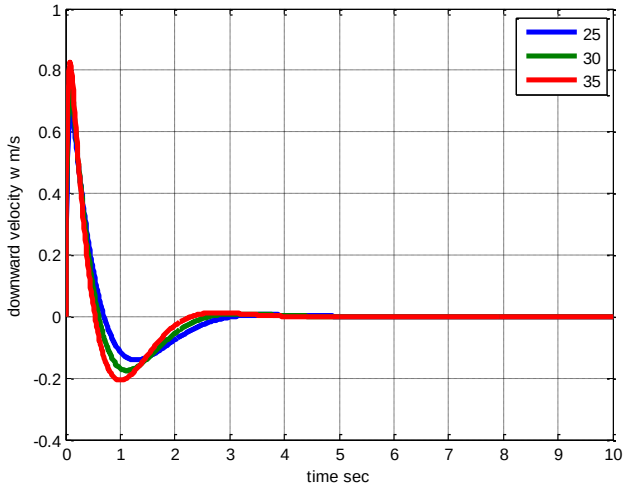

Figure 5-24 LQR responses at different velocities for downward velocity

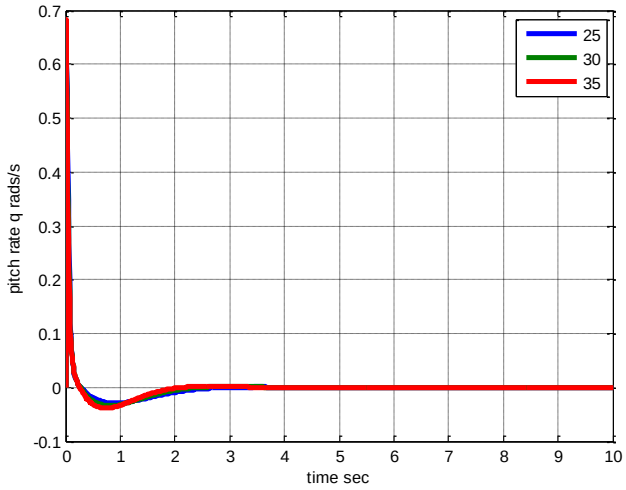

Figure 5-25 LQR responses at different velocities for pitch rate

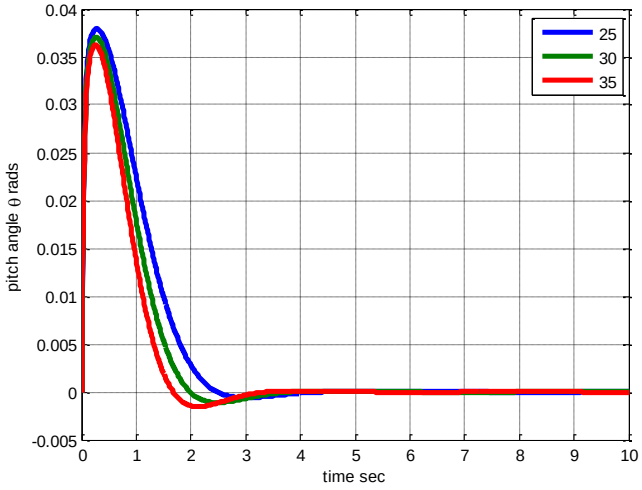

Figure 5-26 LQR responses at different velocities for pitch angle

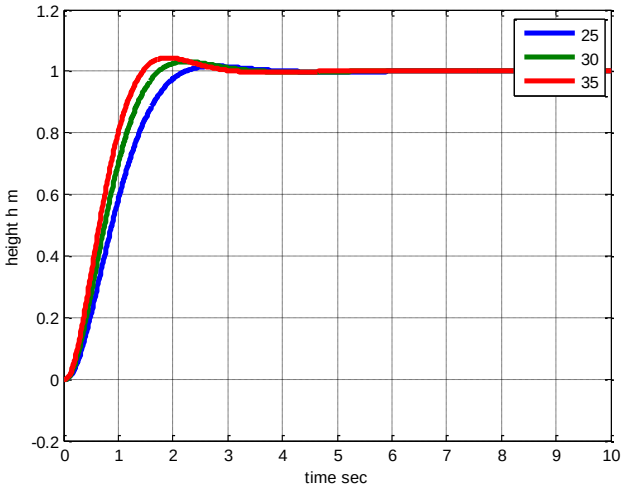

Figure 5-27 LQR responses at different velocities for height

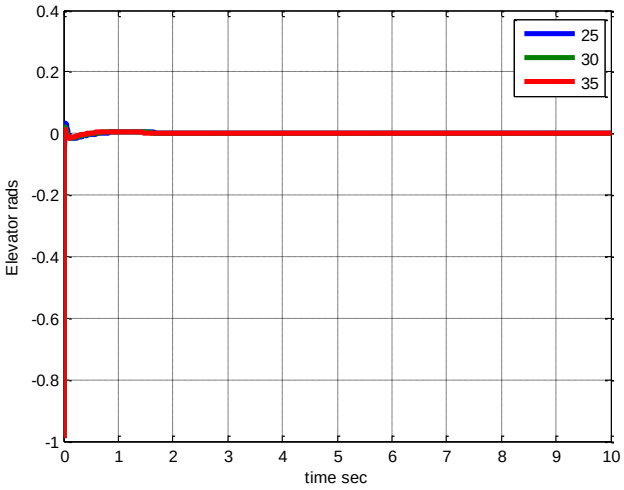

Figure 5-28 LQR responses at different velocities for elevator

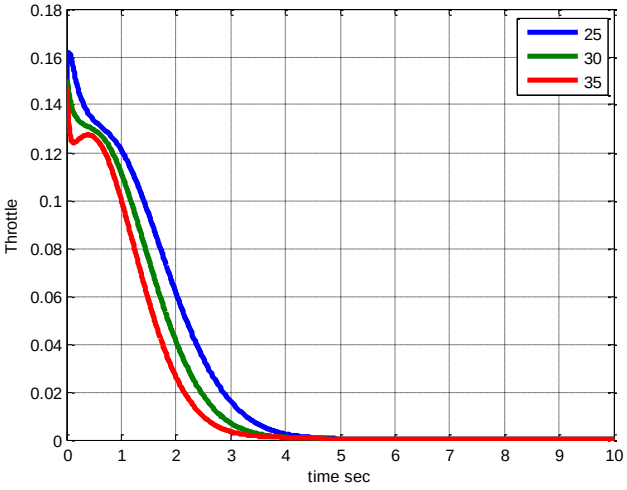

Figure 5-29 LQR responses at different velocities for throttle

5.6 Summary

A brief review of a number of widely-used control design techniques such as, pole-placement, Linear-Quadratic Regulator (LQR), Linear Quadratic Gaussian (LQG) control and optimisation with loop shaping is initially presented. Of these methods LQR and optimisation with loop shaping were selected to design the multivariable, robust flight control system for the X-RAE1 due to their common use in aero applications. Both control design techniques were analysed and responses compared both having very fast responses of under 5 seconds in the height response. Then the robustness of the two designs with respect to speed variations was examined at 25, 30 and 35 m/s. Overall the variation of the results was remarkably low. In addition the control system design indirectly validated the mathematical model of the UAV.

CHAPTER

6

Effector Array CFD Model

This Chapter gives an outline of the Computational Fluid Dynamics Procedure used to construct both a two and three dimensional models of the X-RAE1 unmanned aircraft wing.

The first model is a reconstruction of the actual wing which is a Wortmann FX63-137 wing which has a concave lower surface and is used to validate the CFD results against experimental data. The second model is the modified Wortmann FX63-137 with an embedded effector array to modify the air flow.

The CFD work in this chapter can be used to validate the model of the wing by direct comparison with the experimental data provided. The close agreement of the two sets of results which is established in this chapter provide further evidence for the accuracy of the overall aerodynamic model used in chapter 4 and 5. Moreover, the accuracy of the above results ensures indirectly the validity of the aerodynamic characteristics of the modified wing with the embedded effector array.

The CFD process involves creating two and three dimensional models for the Wortmann FX63-137 using geometry data gathered by the National Advisory Committee for Aeronautics. These models were then meshed in Gambit, then loaded into FLUENT where flow boundary conditions were set. The airfoil lift, drag and moment coefficients from the numeric simulation were then gathered. The results are presented graphically for a selected range of values. Contour plots of velocity

magnitude and pressure coefficient are also included to help describe the behaviour of the flow and its impact on the computed lift, drag and moments coefficients.

6.1 Computational Fluid Dynamics Procedure

Computational Fluid Dynamics is a tool for providing a solutions to many complex aerodynamic flow fields that without it, would never have been solved theoretically (Anderson, 2011). CFD uses high speed digital computers to solve the full Navier-Stokes equations for any three dimensional, steady, unsteady, incompressible, compressible, inviscid or viscous flow problem (Wendt et al., 2009). Using the dramatic advances in computing CFD analysis is becoming a replacement for wind tunnel testing as it is much more cost effective.

To analyse the air flow around the wing of the X-RAE1 a complete 3-D CFD-analysis is required. This is computed by solving the Navier-Stokes equations, which define any single-phase fluid flow. A 3-D model of the X-RAE1 wing was created featuring only the wing and no controls. As the controls have insignificant impact on the overall results and are removed since these details would only add to the amount of computer work needed further on in the CFD process.
Once complete the geometrical 3-D model is discretised to form a volume mesh befitting the case under investigation. Then run through the flow solver in order to evaluate the quality of the mesh. The flow solver boundary conditions are then set along with a number of parameters in order to reach convergence. Forces are then monitored and thereafter visualised and analysed.

A large number of elements are used to accurately describe the flow. Also this requires that the dimensions are described as precisely as possible. As of today there exists no software which includes all necessary parts of the CFD process, therefore the process is divided into four steps, each designed to carry out one specific task; geometry creation, mesh generating, flow solving and analysing results. Figure 6-1 illustrates the CFD analysis steps taken and a breakdown of the tasks required for each step. As can be seen the CFD analysis is a complex process, which requires a smooth transition between steps. Each step is discussed further below.

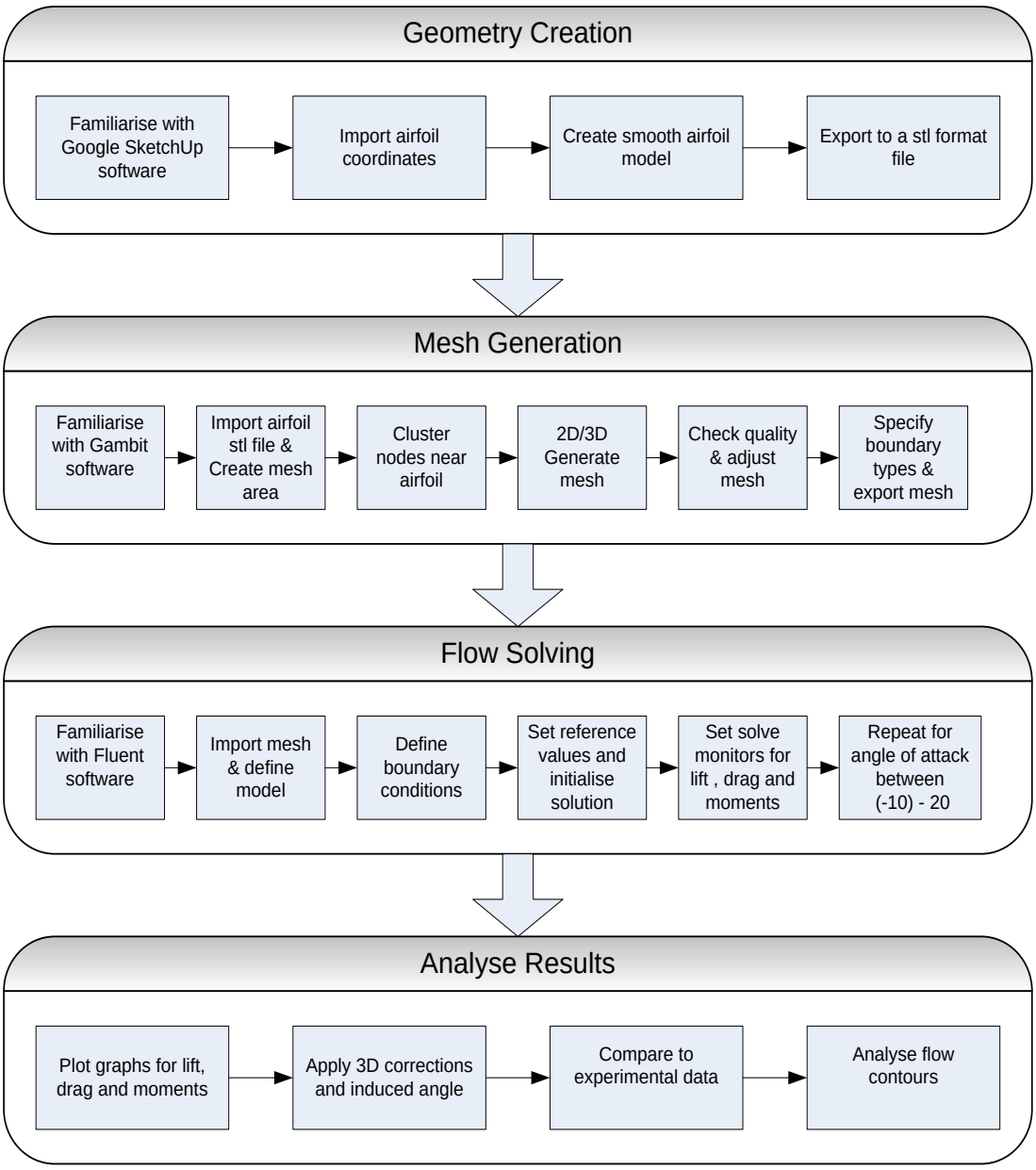

Figure 6-1 Steps carried out for CFD analysis

6.1.1 Geometry Creation

The airfoil geometry was created using Google SketchUp software. Google SketchUp is a design tool for creating 2D and 3D models effectively. Initially the airfoil profile is set by importing the point coordinates that define the airfoil profile (Selig, 2011). This was approximately 100 points for both bottom and top sides of the airfoil. The points are then connected smoothly using a bezier curve plugin giving a closed model area. The chord length is defined as 0.353 meters for the 2D

models. For the 3D models, two cross sections airfoil's are used. One has a tip chord and the other has a centre chord which are joined together with distance apart of the span length as shown if Figure 6-2. The model design is saved as a stl file and exported ready to be used by Gambit software.

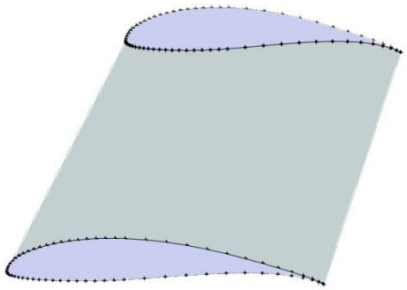

Figure 6-2 3D Geometry of Wortmann FX63-137

6.1.2 Mesh Generation

The stl file is imported into Gambit. Gambit is a modelling software that is capable of creating meshed geometries that can be read into FLUENT and other analysis software.

The coordinates that define a farfield boundary and mesh region between the airfoil geometry are set. The farfield boundary is positioned far away from the airfoil to insure the flow has not been disturbed and are at ambient conditions.
When designing the mesh nodes are clustered near the airfoil as this is where the flow is modified the most and are critical at the leading and trailing edge. This is shown in Figure 6-3 of the 2D model of the airfoil. The mesh resolution becomes progressively coarser at the farfield boundaries since the flow gradients approaches zero. To increase the accuracy of the model the number of cells that exist around the airfoils surface where repeatedly increased up to eight million. However, by increasing the density of the mesh the calculation time is increased. It was demonstrated that any further increase of cells above two million had no effect to the accuracy of the data. This enforced the quality of the mesh. After completing the mesh the boundary types are defined. This being of type wall for the airfoil and type pressure-far-field for the area round the airfoil. Finally the air

flow region is defined as air and the mesh is exported ready to be read by FLUENT. Figure 6-4 shows the volume mesh of the 3D wing.

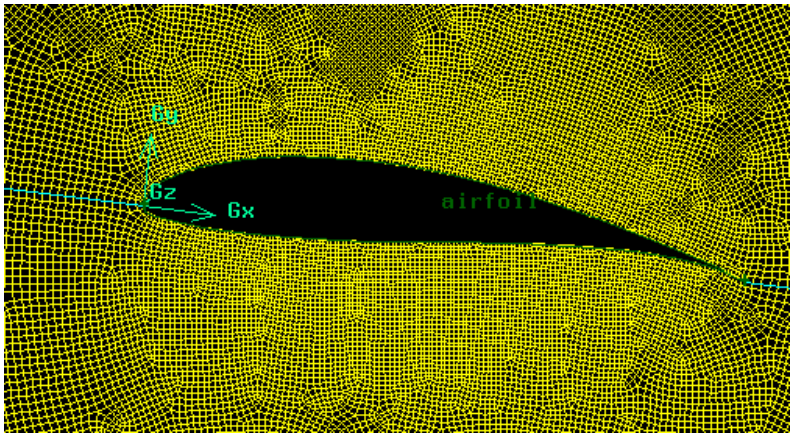

Figure 6-3 2D mesh of airfoil boundry layer

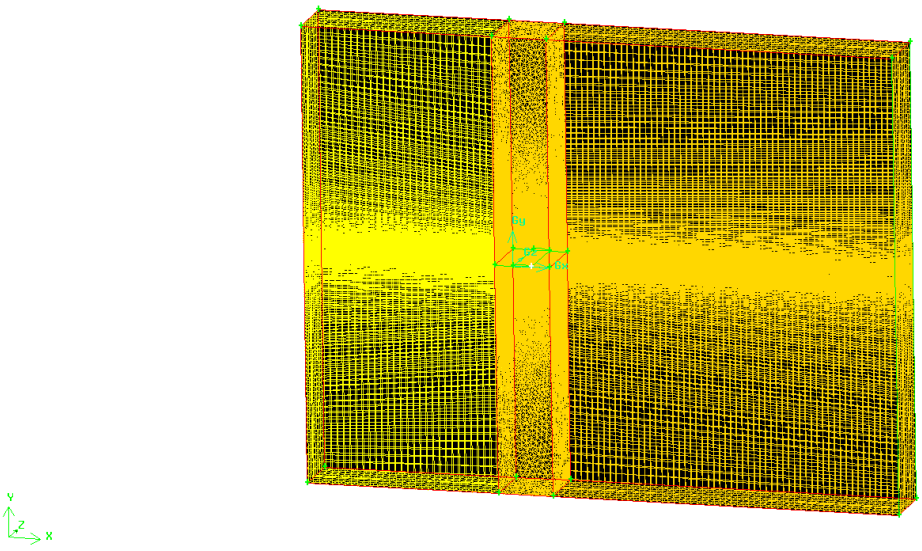

Figure 6-4 3D mesh of the Wortmann FX63-137 wing

6.1.3 Flow Solving

The desired mesh is read into FLUENT which runs the geometry through the numerical analysis. Double precision operation (2ddp) is used for two dimensional operations and 3D double precision (3ddp) for three dimensional operations.

Two different viscosity models were tested. The first is the inviscid model which assumes no viscosity. The second is the Spalart-Allmaras (SA) model which is a turbulent eddy viscosity model. Instead of solving for the kinetic energy of turbulence the Spalart-Allmaras model solves directly for the eddy viscosity from a transport equation. The Spalart-Allmaras model was designed for aerospace applications involving wall-bounded flows. After running both viscosity models over a range of angles of attack between -10° and 20° the results concluded that the Spalart-Allmaras model gave a greater accuracy.

The boundary conditions for the boundaries that were defined in Gambit are defined similarly the reference values which include the dimensions of the airfiol are set.
The convergence criterion was set to $1x10^{-6}$ for each residual. Due to the large number of cells in 3D models a small convergence criterion lead to long computation times. Monitors were then configured in order to directly monitor the lift, drag and pitch moment coefficients for the airfoil.

6.1.4 3D Corrections of CFD Data

A correction was required for the 2D CFD data to be comparable to the experimental wind tunnel data. The lift of the 3D wing at a certain angle of attack is less than the lift of the two dimensional airfoil, which corresponds to a wing of infinite span. This relationship depends on the aspect ratio of the wing and can be used to approximate the lift of a 3D wing from the 2D data.

The curve slope a_0 obtained from CFD simulation has been used to calculate the 3D lift curve slope for a finite aspect ratio wing, using approximation derived by

Helmbold and reported in Laiton, (1989). Equation 6.1 shows the derivation of a_0 and a.

$$\alpha_{2D} = ((\alpha_{3D} - \alpha_0)\frac{a}{a_0}) + \alpha_0$$
$$a_0 = \frac{\Delta C_t}{\Delta \alpha_0} = 5.615 \qquad (6.1)$$
$$a = \frac{a_0}{1 + \frac{a_0}{\pi e \Lambda}} = 4.438$$

Where:

e span efficiency factor

a_0 lift slope of the infite wing (2D airfoil)

a lift slope of the finite wing (3D wing)

6.2 Experimental Data

The experimental data has been taken from wind-tunnel tests carried out on a full-scale model of the X-RAE1 unmanned aircraft in the RAE 24ft wind-tunnel over an airspeed range from 20 m/s to 50 m/s (Trebble, 1985b). The Wortmann FX63-137 wing which has a concave lower surface and it is positioned on the fuselage with the tangent from the tangent from the trailing edge to the lower wing surface inclined at +1 degrees to the fuselage datum.

6.3 CFD model comparison against experimental model

This section reports a comparison of experimental measurements taken from wind tunnel data (Trebble, 1985b) and the computed CFD data of the X-RAE1 wing. An initial 2D CFD study was created followed by a 3D CFD study. The purpose of the study was to assist the experiments, ascertain the capability of CFD to calculate Lift, Drag and Pitch forces.

Figure 6-5 shows the comparison of the lift coefficient of the airfoil from wind tunnel data, 2D and 3D CFD results. The simulated 2D and 3D lift curve slope compares well with the one obtained experimentally. The lift curve slope obtained

from 2D calculations has been corrected for a finite aspect ratio wing, using finite aspect ratio wing theory corrections, reported above. The lift curve slope was used to predict the lift coefficient up to an angle of attack of 20 degrees. Experimental data showed that lift varies linearly up to 10 degrees. It can be seen from Figure 6-5 that the agreement between estimated and measured values of lift is plausible. Once the CFD data was validated, qualitative evaluation from the CFD results (pressure distributions, velocity contours, etc.) were created.

Figure 6-6 shows the comparison of the drag vs lift coefficients of the airfoil between experimental and CFD data. It can be seen that the agreement between estimated and measures values of drag are good. The peak value of the lift/drag ratio is 20 which is attained at C_L = 0.5. The 2D CFD curve slightly deviates from the experimental data at lower values of lift coefficient. This non-linearity is almost certainly related to the interaction between transition and separation points on both surfaces and has previously been observed in experimental research at low Reynolds number by (Mueller and Batill, 1982).

Figure 6-7 illustrates the comparison of the moment coefficient of the airfoil against the lift coefficient from experimental data, 2D and 3D CFD results. The simulated 2D and 3D lift curve slope compares well with the one obtained experimentally. Similarly to Drag there is a slight deviation from the experimental data at lower values of the lift coefficient.

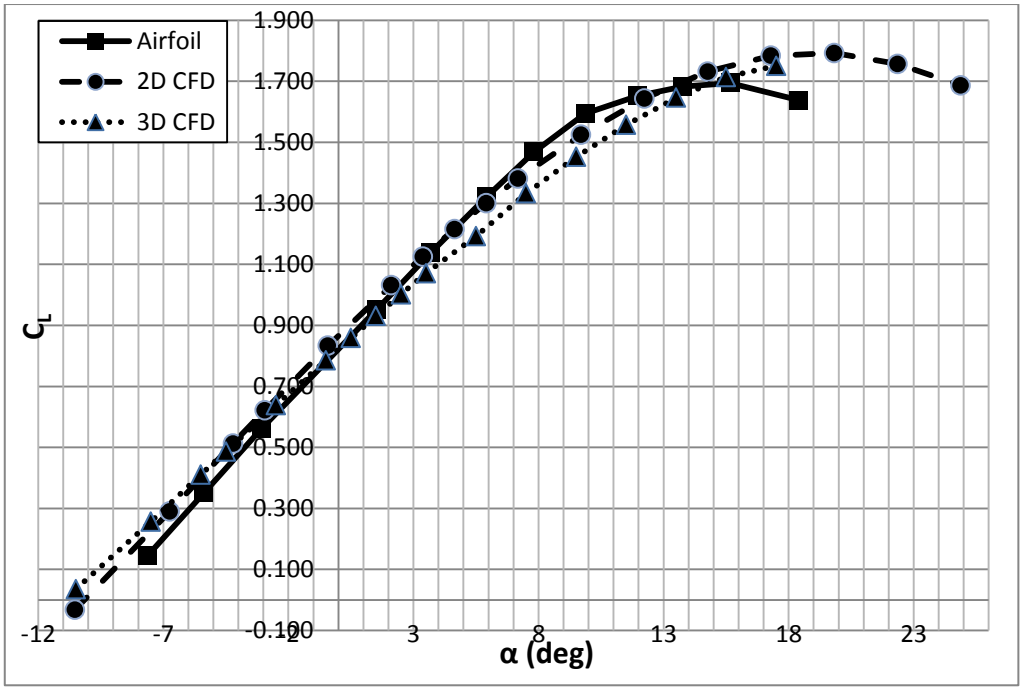

Figure 6-5 Comparison of computed lift coefficient and wind tunnel results

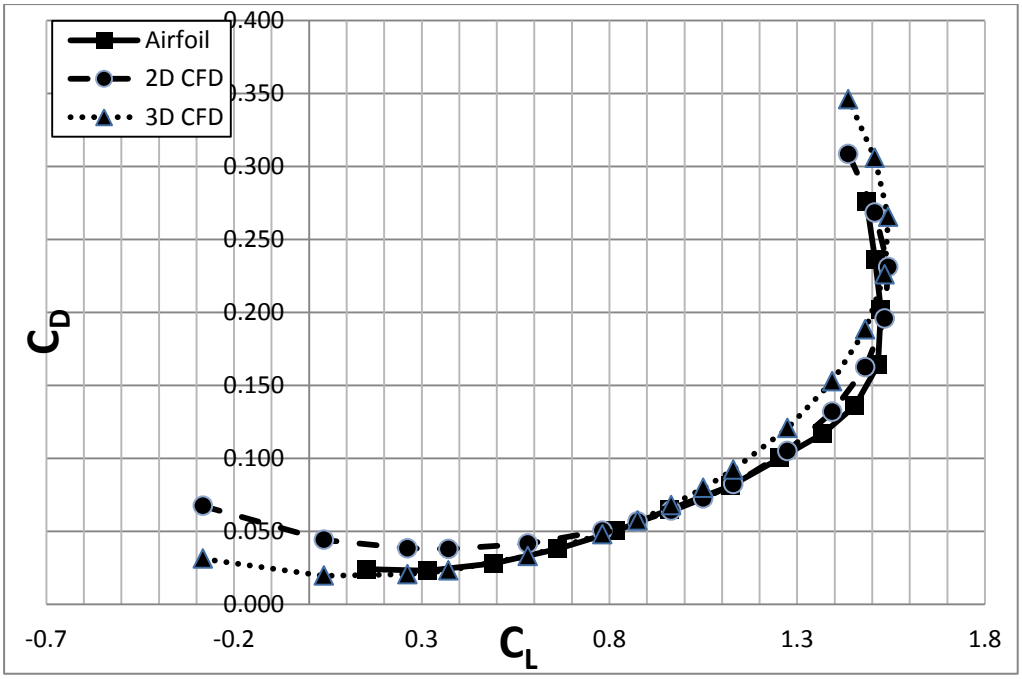

Figure 6-6 Comparison of computed drag coefficient and wind tunnel results

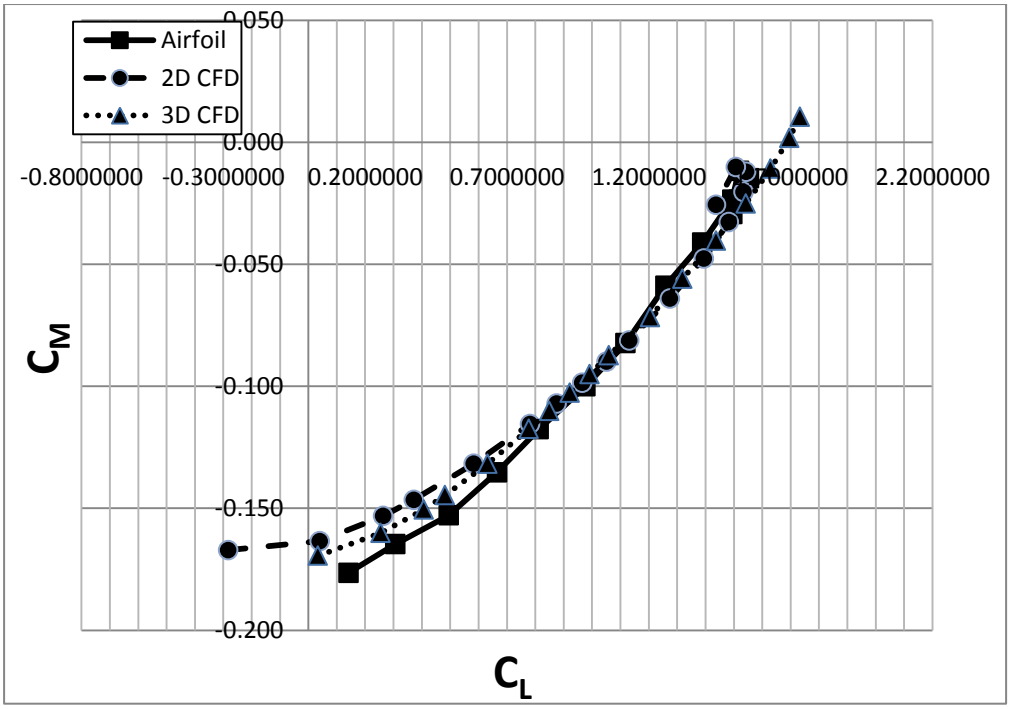

Figure 6-7 Comparison of computed moments coefficient and wind tunnel results

6.3.1 Flow Studies

Flow studies have been carried out on the X-RAE1 (Trebble, 1985b) using fluorescent powder suspend in oil was painted on the wing upper surface. The tunnel was then run at the desired speed until most of the oil had evaporated, when flow patterns could be seen clearly on wing as shown in Figure 6-8. The line of flow separation moves progressively forward as the angle of attack is increased and early signs can be seen from an incidence of 4 degrees.

This was reconfirmed using CFD simulation to illustrate the flow around the X-RAE1 wing. Figure 6-9 and Figure 6-10 shows the speed contours at 40m/s for an angle of attack of 8 degrees. The flow moves smoothly around the airfoil, remaining fully attached to the upper surface with only a slight flow separation towards the trailing edge taking place on the leading edge, the stagnation point is clear where the velocity of the flow is nearly zero. The fluid accelerates on the upper surface as can be seen from the change in colours of the vectors and on reaching the trailing edge, the flow on the upper surface decelerates and converge with the flow on the lower surface.

Figure 6-11and Figure 6-12 illustrates the contours and plot of the pressure coefficient. The negative part of the plot is upper surface of the airfoil as the pressure is lower than the reference pressure. This complies with the Bernoulli equation whenever there are high velocity vectors, we have low pressures and vice versa. There is slight evidence of flow separation visible in the pressure distribution over the upper surface, where the distribution is altered. This is noticeably clear in Figure 6-13 which shows the pressure distribution at an angle of attack of 14 degrees. At this angle, the viscous forces within the flow are strong enough to cause flow separation which can be seen. Here the initial decrease in pressure is much greater, reaching a minimum value within the first 5% of the chord length from the leading edge. The flow is then subjected to severe adverse pressure gradients where the pressure increases rapidly as the flow moves downstream from the leading edge. As a result, the flow begins to separate from the upper surface. Preceding this event, the pressure distribution becomes flat towards the trailing edge at a value of -2. Indicating the flow fails to recover above the free stream pressure at the trailing edge.

The location where the pressure distribution suddenly becomes flat over the upper surface is known as the separation point. The flow tends to separate from the trailing to the leading edge as the angle of attack is increased.

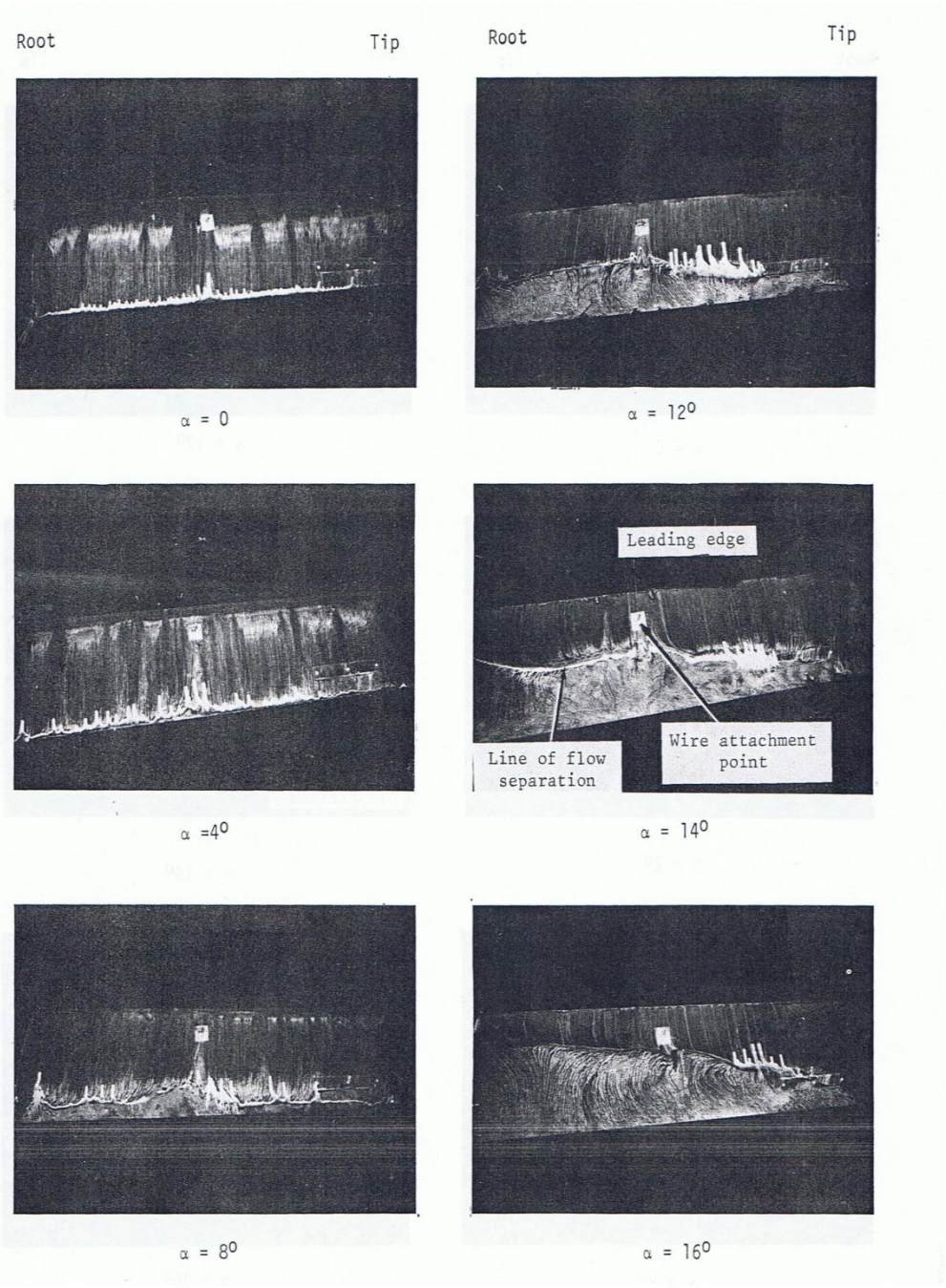

Figure 6-8 Flow over upper surface of X-RAE1 wing

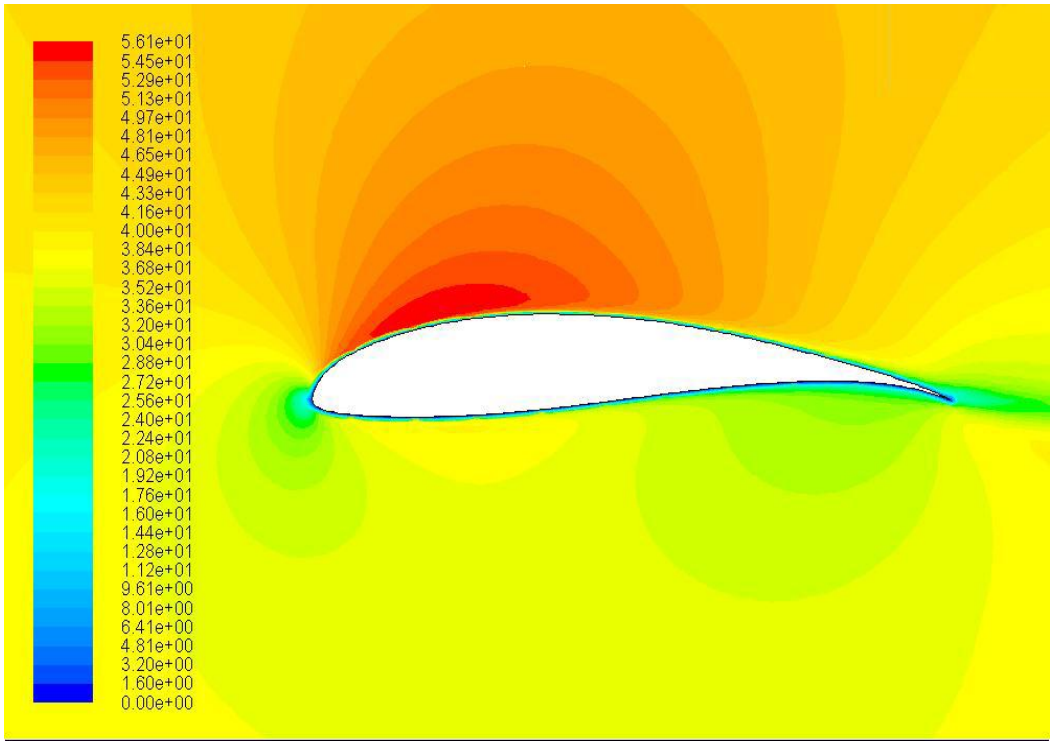

Figure 6-9 Contours of velocity Magnitude of 2D CFD model

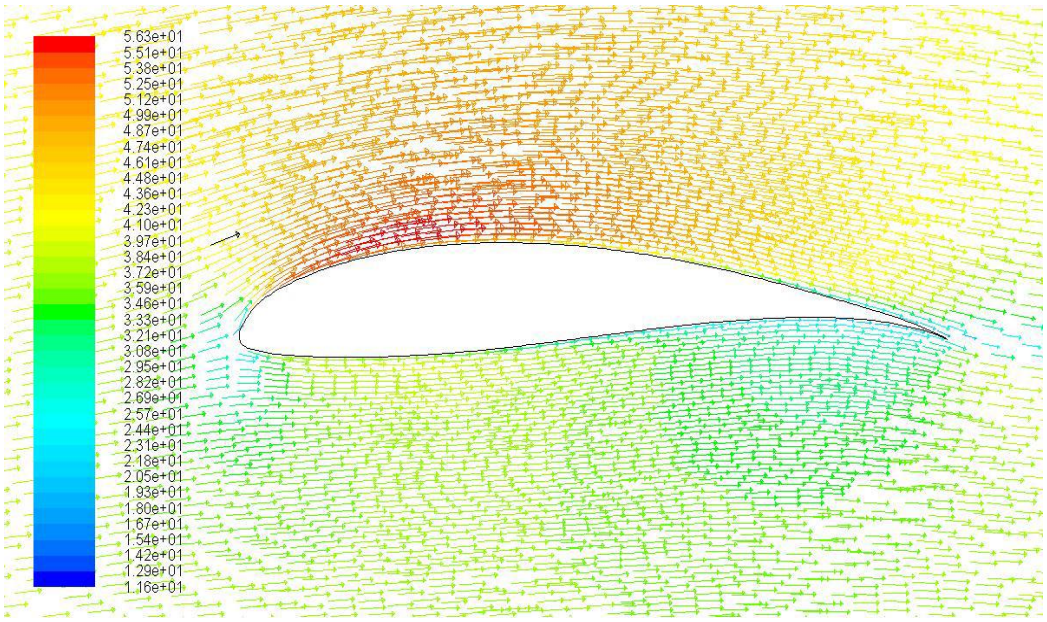

Figure 6-10 Contours of velocity Magnitude and direction of 2D CFD model

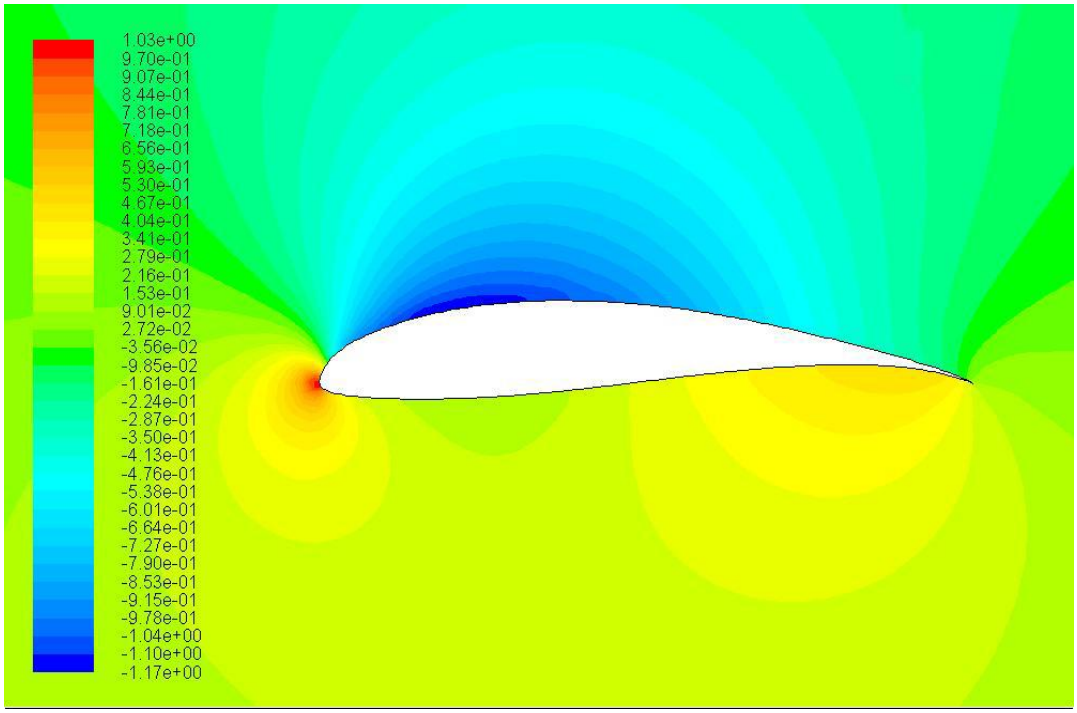

Figure 6-11 Contours of pressure coefficient of 2D CFD model

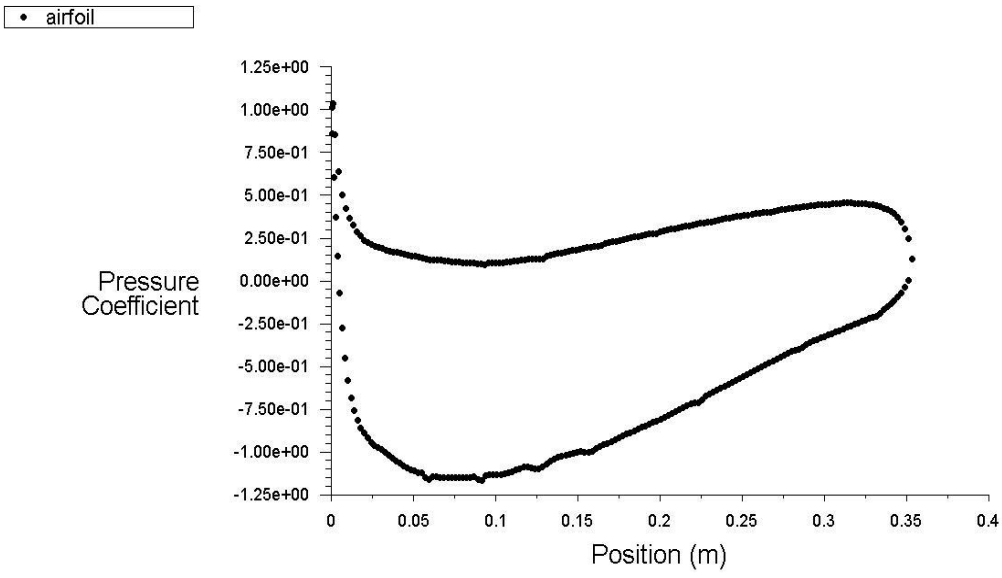

Figure 6-12 Plot of pressure coefficient of 2D CFD model

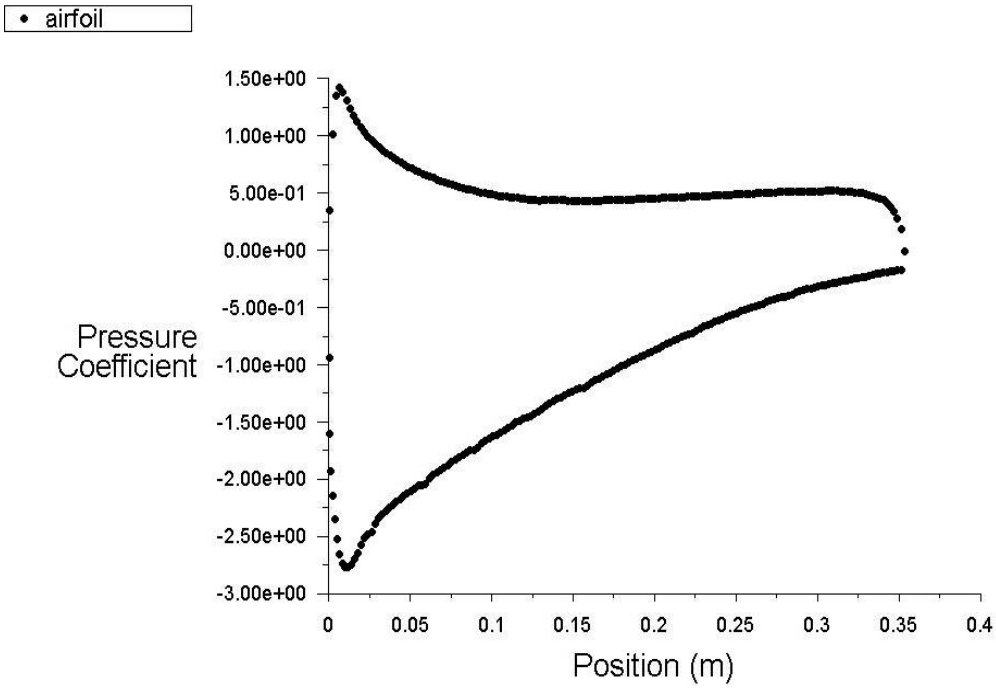

Figure 6-13 Plot of pressure coefficient of 2D CFD model at 14 degrees

6.4 Distributed Effector Array

As discussed in the literature review flow control techniques are the most suitable for any successful shape morphing of low speed/small aircraft. Using the generic model defined in (Raney et al., 2004, Raney et al., 2000) on the X-RAE1 a suitable model using flow control can be simulated and examined.

This model consists of small bump which deflects normal to the surface of the X-RAE1 wing imitating the effect of shape memory alloy diaphragms, piezoelectric domes and inflatable blisters, which all produce real surface distortions. The placement of these bubbles is distinguished by analysing wind tunnel data and CFD simulation at different placement on the wing. The size of the bubble was set to 6mm height to approximate the physical displacement produced by such materials.

6.4.1 Distributed Effector Array Placement

The placement of the bubble was tested on three different locations on the airfoil. This being the front, middle and back of the airfoil as show in Figure 6-14. Creating

2D CFD models for each placement and examining the flow around the airfoil it can be seen that that the placement of the bubble at the back of the airfoil, i.e. the trailing edge has the most dramatic effect on the airfoil lift. Figure 6-15 shows the lift coefficient at different angels of attack for the different bubble placements. It can be seen at low angles of attack the lift is highest where the bubble position is at the back of the airfoil.

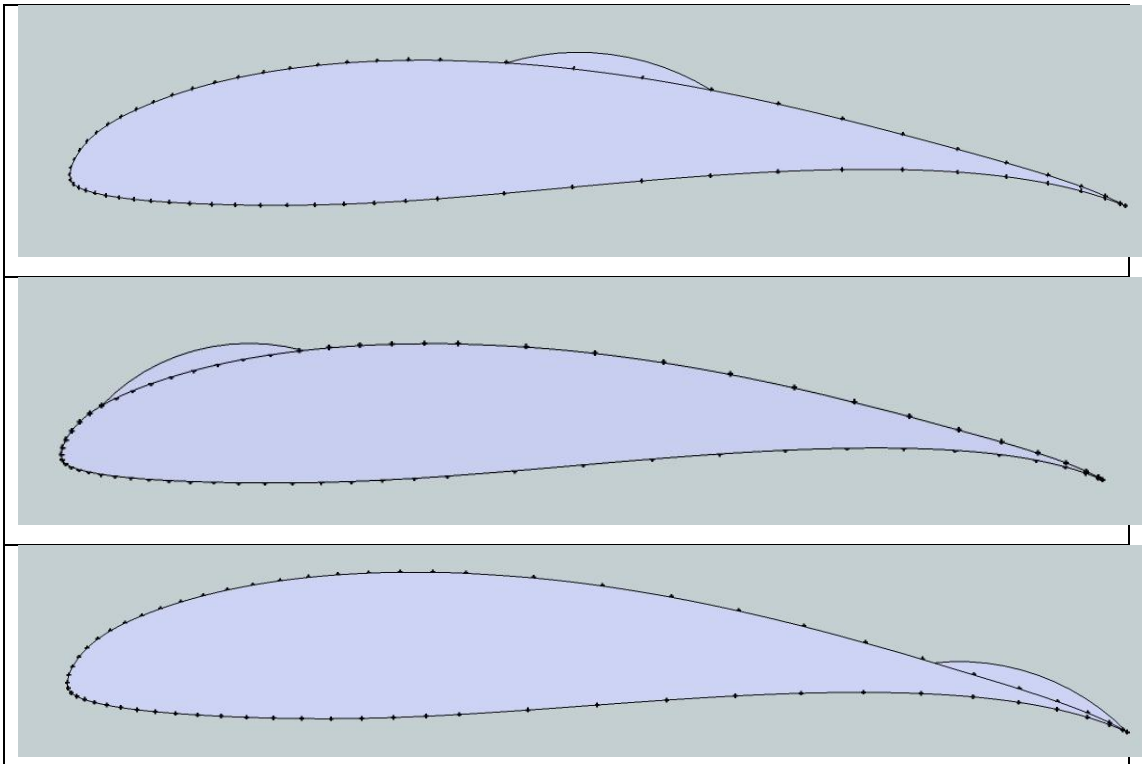

Figure 6-14 Bubble location on airfoil

The explanation for this is due to the fact that the flow separation starts at the trailing edge of the airfoil and progressively moves forward with larger angle of attack. By placing the bubble at the trailing edge; the flow separation is delayed giving rise to higher lift at the lower angles of attack as. The improvement is small of approximately 0.05. As the angle of incidence is increased the flow separation happens towards the middle/front of the airfoil, which has no or even a negative effect of the bubble at the trailing edge.

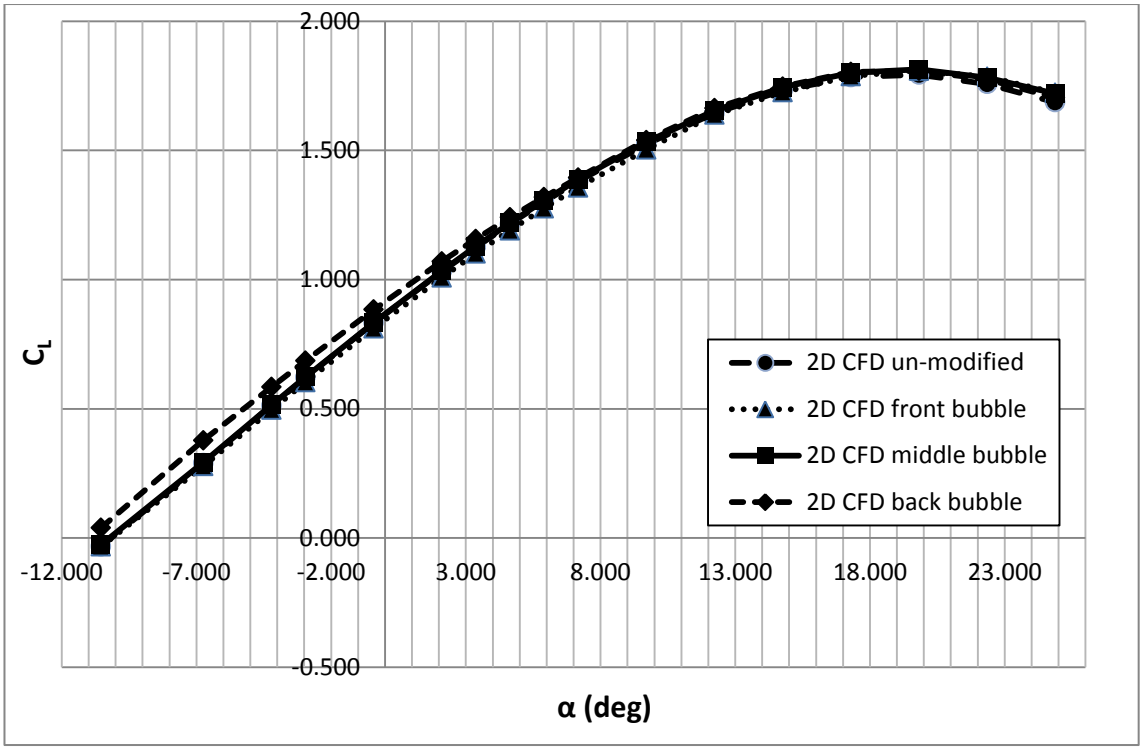

Figure 6-15 2D Comparison of computed lift coefficient at diffrent bubble placement

6.5 3D CFD Model of Effector Array

A 3D Model of the airfoil with a bubble at the trailing edge was created as shown in Figure 6-16 . This bubble was extended across the trailing edge. Using 3D CFD analysis this modified 3D model was compared to the 3D un-modified airfoil.

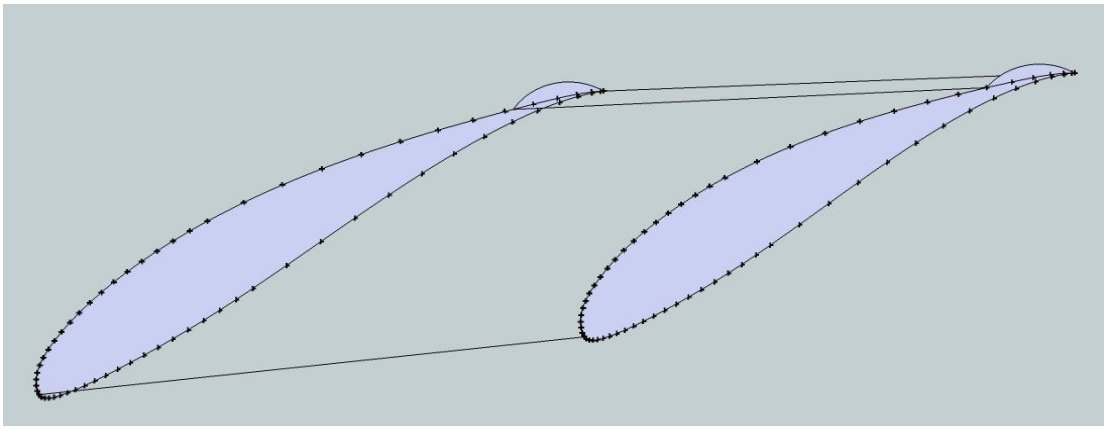

Figure 6-16 3D model of airfoil with bubble at trailing edge

The computed values of lift, drag and pitch forces are presented for both the modified and un- modified 3D airfoil. Figure 6-17 shows the comparison of the lift coefficient of the airfoil from the 3D un-modified and the 3D modified with a back bubble airfoils. An initial look would suggest that no drastic change has been made by having a bubble present on the trailing edge. Looking closer it can be derived that the modified wing favours well with lower angles of attack having an increase in lift coefficient with an average of 0.155 between angle of attack 0 and -10.5. Towards the higher angles of attack near the stall angle the modified wing has a reverse effect and has an average decrease of lift of 0.028 between angle of attack 11.5 and 17.5.

Figure 6-18 shows the comparison of the moment coefficient of the airfoil from the 3D un-modified and the 3D modified with a back bubble airfoils. The modified wing has an overall lower moment's gradient of approximately 0.05 compared to the un-modified wing.

Figure 6-19 shows the comparison of the drag vs lift coefficients of the airfoil from the 3D un-modified and the 3D modified with a back bubble airfoils. It can be seen that there is an overall increase in drag in the modified wing with an average increase of 0.005 at low angles of attack and 0.006 at high angles of attack. At high angles of attack there is a significant increase of the C_L / C_D ratio which will delay the stall of the UAV. A summary of the average change in the C_L, C_M and C_D coefficients for the modified wing is listed in
Table 6-1.

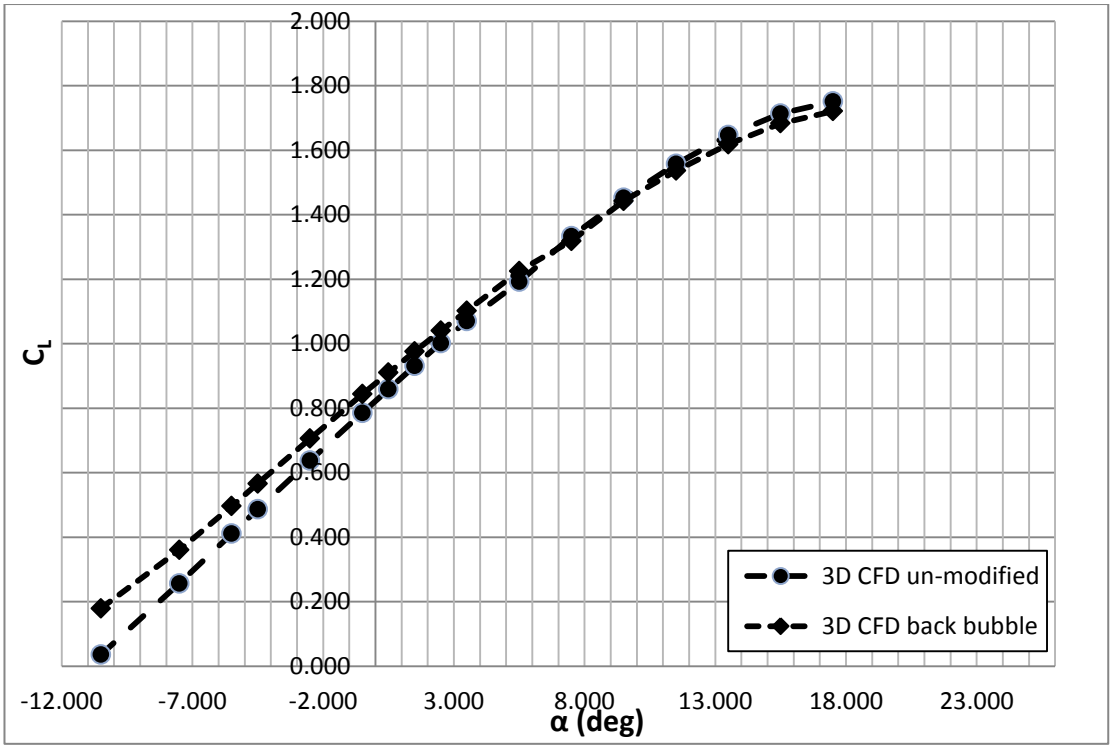

Figure 6-17 3D Comparison of computed lift coefficient between un-modified and modified back bubble

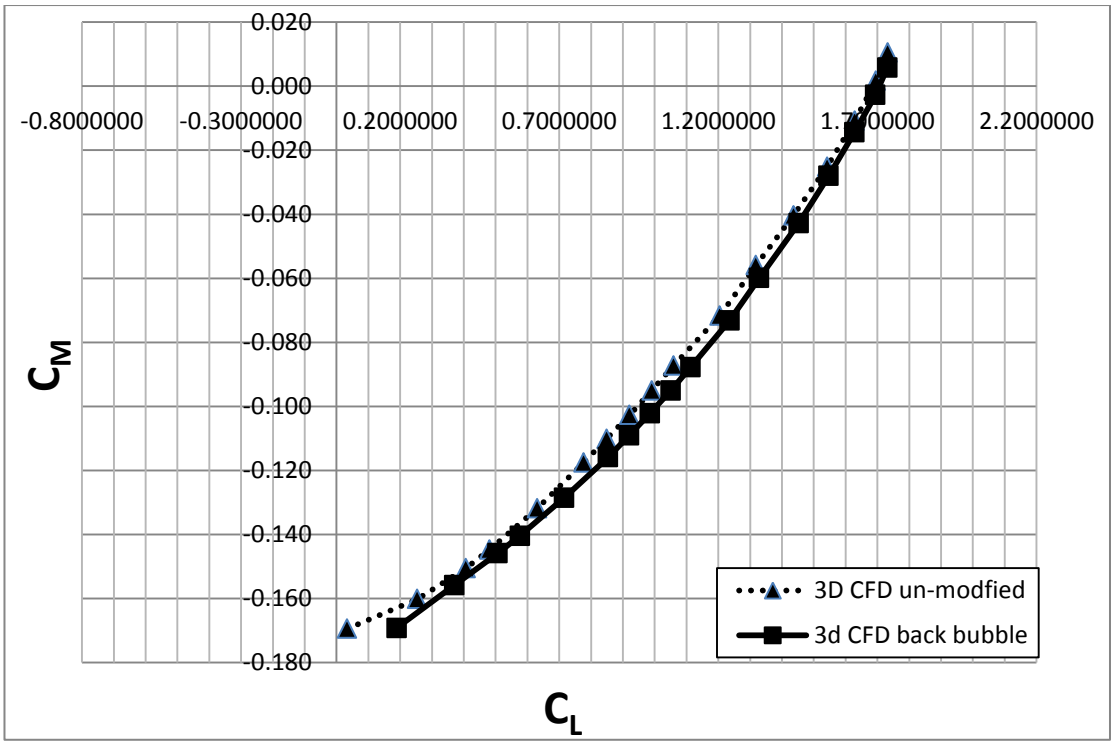

Figure 6-18 3D Comparison of computed moments coefficient between un-modified and modified back bubble

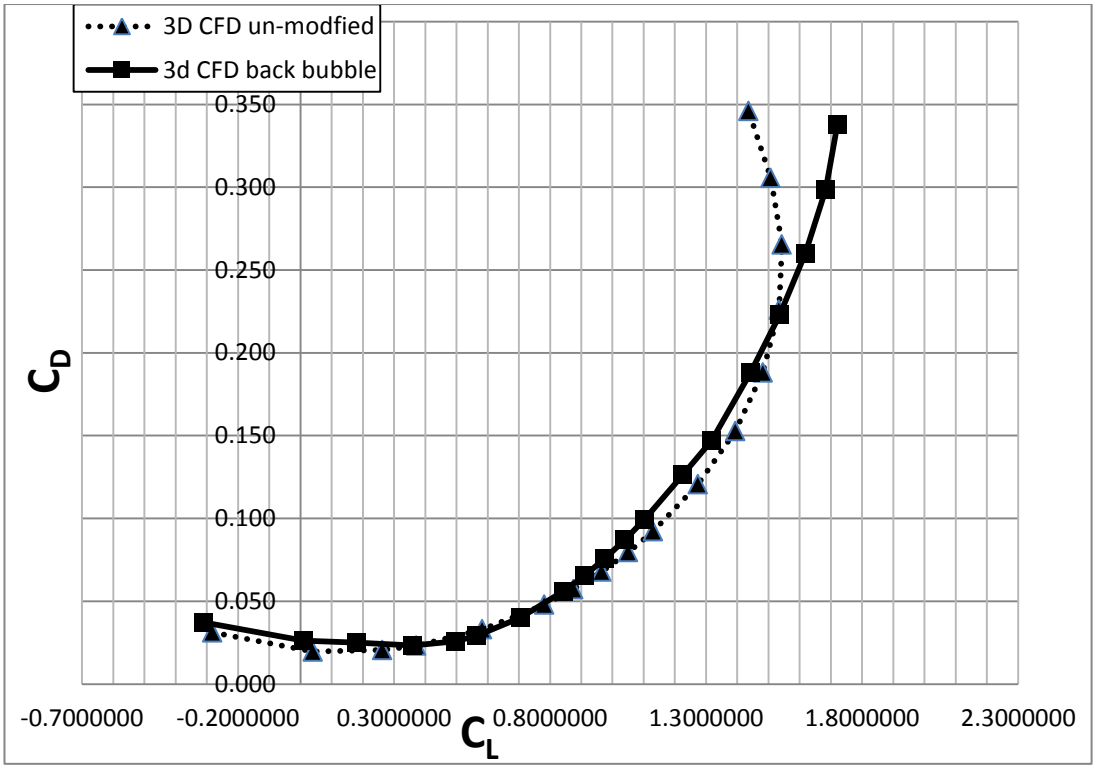

Figure 6-19 3D Comparison of computed drag coefficient between un-modified and modified back bubble

	C_L	C_M	C_D
Low angle of attack	0.1 (40%)	0.005 (5%)	0.005 (22%)
High angle of attack	-0.028 (2%)	0.005 (5%)	0.008 (9%)

Table 6-1 Summary of average change to the coefficients for the modfied wing

6.5.1 Flow Comparison between Modified and Un-modified 3D models

The flow around the 3D un-modified and modified models are examined below. Figure 6-20 shows the speed contours at 40m/s for an angle of attack of 8 degrees and Figure 6-21 is a more close-up view of the speed contours towards the trailing edge of the airfoil. The fluid accelerates on the upper surface as can be seen from the change in colours to orange/red of the vectors and on reaching the trailing edge, the flow on the upper surface decelerates and converge with the flow on the lower surface. Comparing this to the modified wing in Figure 6-22 and Figure 6-23. The

speed contours have a second acceleration point where the bubble has been placed. After which the flow on the upper surface decelerates and converge with the flow on the lower surface without flow separation.

Figure 6-24 and Figure 6-25 illustrates the contours of the pressure coefficient for the unmodified and modified 3D models respectively. The pressure at the upper surface is lower than the reference pressure. In Figure 6-25 there is a second dip in pressure where the bubble has been placed. This coincides with the increase in velocity caused by the bubble.

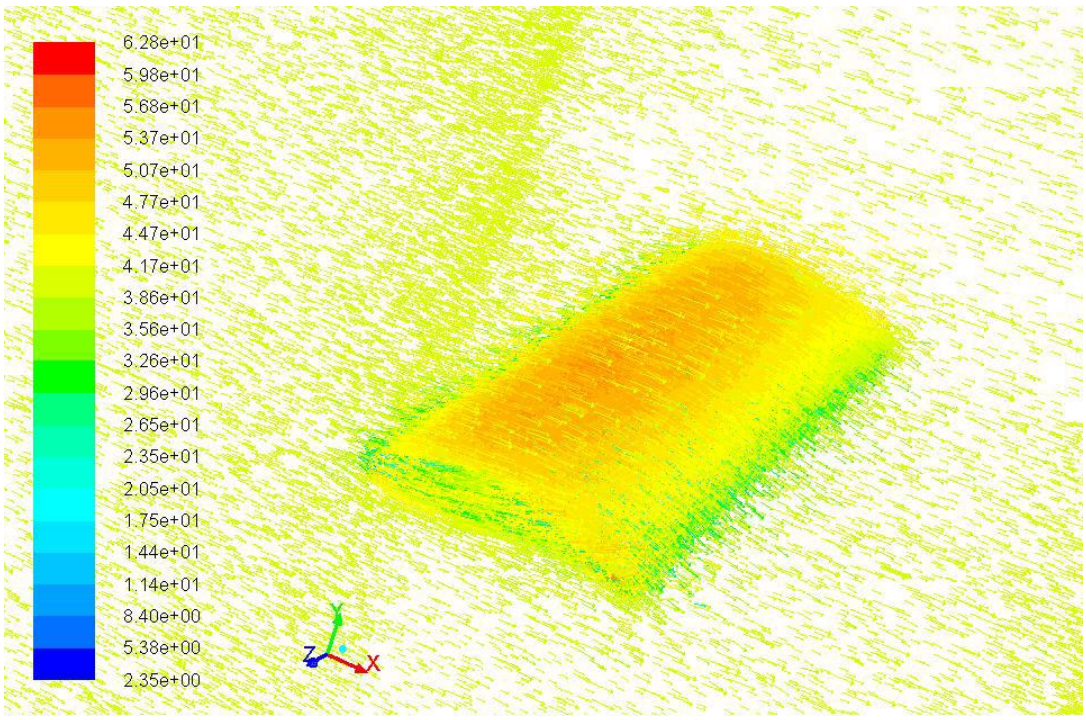

Figure 6-20 Contours of velocity magnitude and direction of 3D CFD model

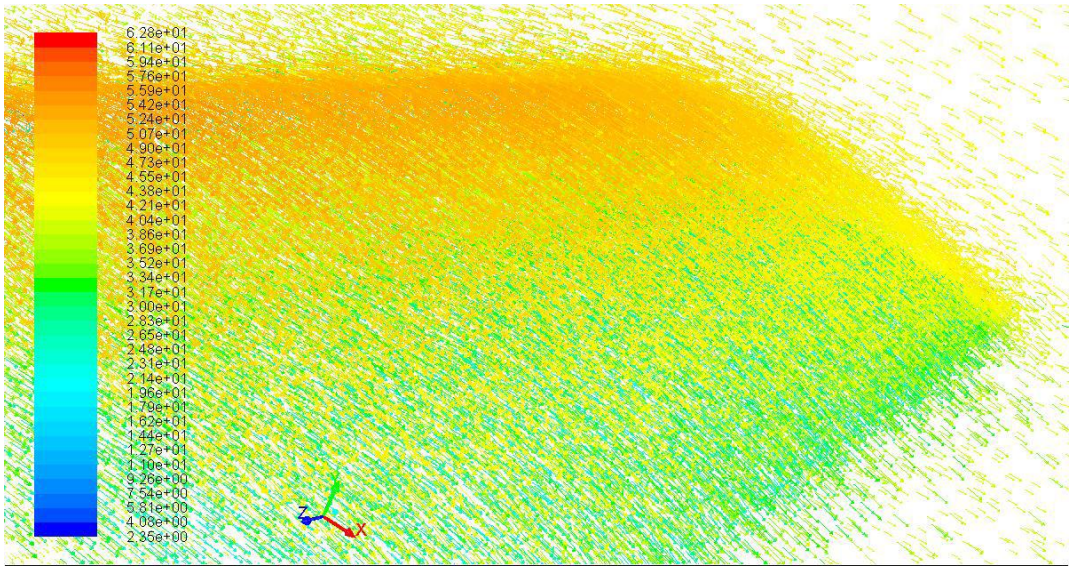

Figure 6-21 A close-up of the velocity magnitude and direction contours for the 3D CFD model

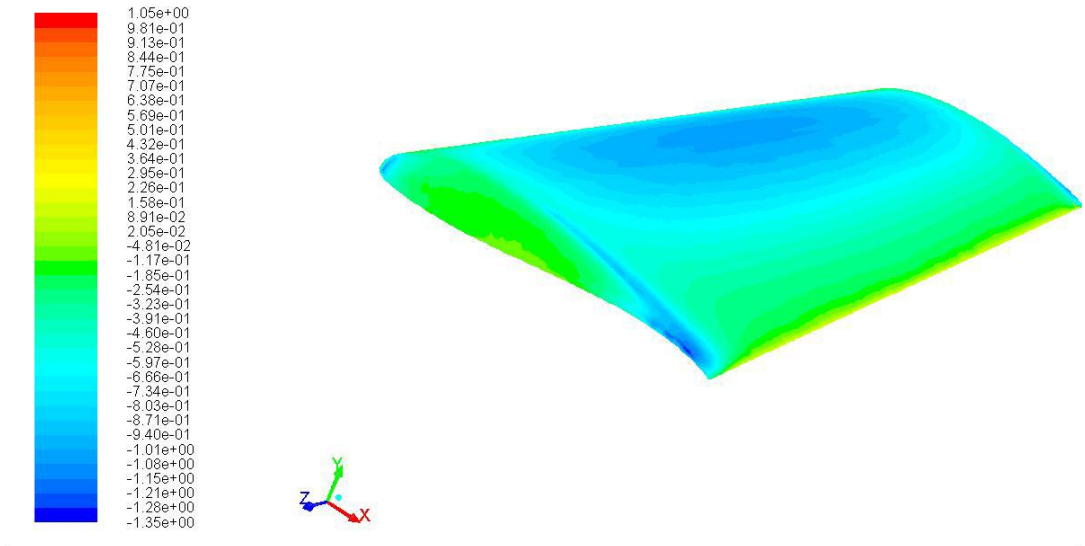

Figure 6-22 Contours of pressure coefficient of 3D CFD model

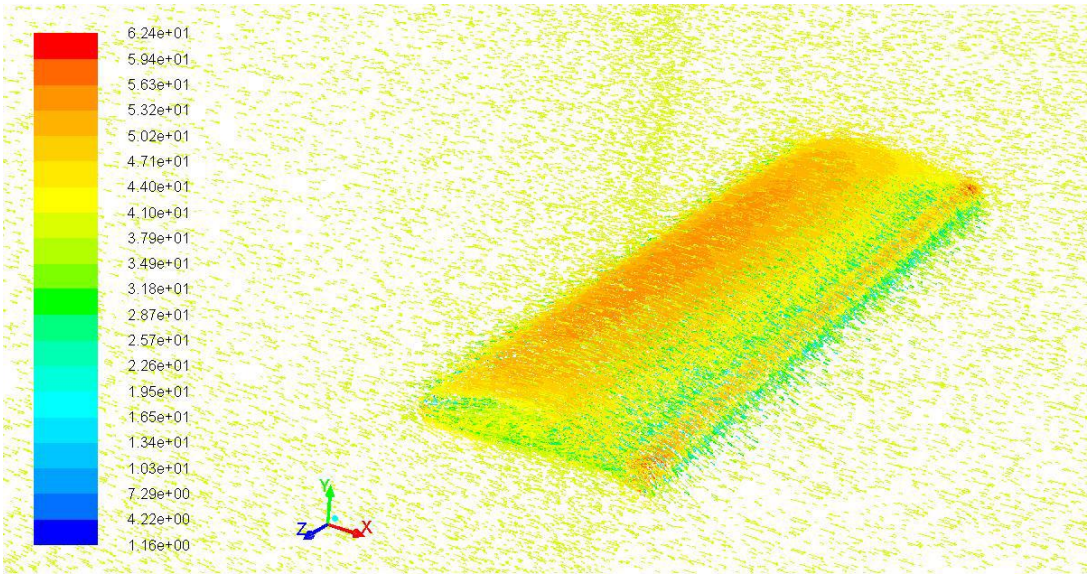

Figure 6-23 Contours of velocity magnitude and direction of 3D modified CFD model

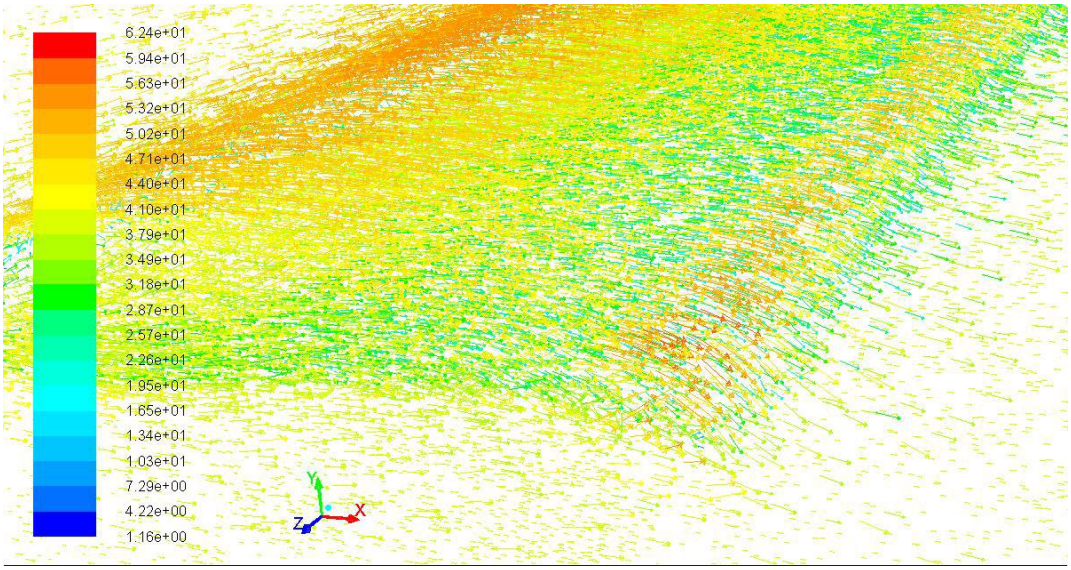

Figure 6-24 A close-up of the velocity magnitude and direction contours for the 3D modified CFD model

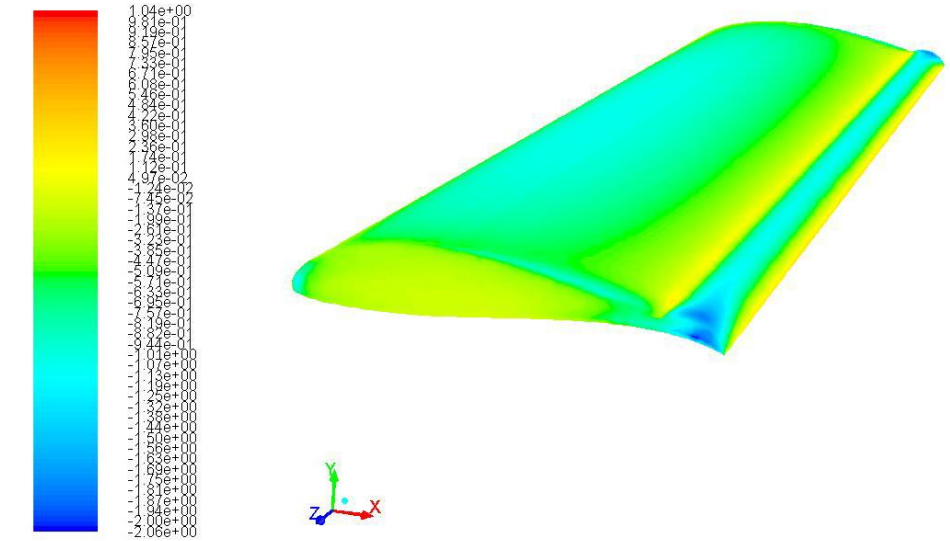

Figure 6-25 Contours of pressure coefficient of 3D modified CFD model

6.6 Summary

The identification of current state of the art wing morphing techniques capable of improving overall performance for a low speed UAVs was investigated as part of the literature review and it was derived that the concept of flow control would be further analysed for the X-RAE1 UAV. This chapter provided an outline of the Computational Fluid Dynamics Procedure used to construct both a two and three dimensional models of the X-RAE1 wing. The first model was a reconstruction of the actual wing which is a Wortmann FX63-137 wing and is used to validate the CFD results against experimental data. Prior to creating the second model the position of the distributed effector array was tested to specify the optimal position for increased lift. The second model was the modified Wortmann FX63-137 with an embedded effector array. The effect of having an effector array was analysed for lift, drag and moments. Contours around the wing were examined to facilitate the results obtained. The lift coefficient favoured well with lower angles of attack having an increased lift coefficient with an average of 0.155 between angle of attack 0 and -10.5. There was also an overall increase in drag in the modified wing with an average increase of 0.005 which counteracted the increased lift for low angles of attack. Nevertheless at high angles of attack there was a significant increase of the ratio which would have a positive effect and delay the stall of the UAV.

CHAPTER

7

Conclusions & Recommendations for Future Work

This chapter begins by presenting the main findings and conclusions drawn from the literature analysis and the empirical research carried out. This is followed by an overview of the contributions the research makes to the body of knowledge, and the research implications. The chapter concludes by providing recommendations that can be used as a foundation for future research in the areas of low speed UAVs modelling and control.

7.1 Research Overview and Findings

This thesis analysed performance enhancement techniques for low speed UAVs using the X-RAE1 UAV. This was based on a framework of theory, modelling and simulation and covered over three key areas of research of which are mathematical modelling, control design and CFD analysis.

Mathematical Modelling

A X-RAE1 model was successfully carried out and provided an aerodynamic model of the vehicle. Using wind tunnel data and ESDU data sheets six degrees of freedom simulation model for the X-RAE1 was developed and used to develop a linearised model for straight level flight at different velocities. The validity of the longitudinal and lateral model was checked by comparing the linearised responses against the non-linear models. This showed a good match confirming the validity for small perturbation analysis. The definitions and derivation of the aerodynamic stability and control derivatives have been listed. This was used to assess the UAVs trim, stability

and control properties. Simulations proved the UAV to have acceptable stability properties over the design operating range. Phugoid and dutch roll modes have been computed and found to exhibit low damping rations. An unstable spiral mode was found but it would not appear to present any significant problems as it is characterised by a large time constant.

Finally an investigation was carried out to study the relationship between the modes of the system and velocity. The phugoid remains almost invariant to velocity change while the short period has an almost invariant damping coefficient and an increasing natural frequency with respect to velocity.

The dutch roll decay is almost invariant to velocity variation, while the frequency of oscillation is increasing with velocity. The roll subsidence becomes substantially faster with increase in velocity and the spiral divergence is almost invariant to velocity changes.

Control System Design

A multivariable, robust flight control system for the X-RAE1 has been designed using LQR and H_∞ optimisation with loop shaping. Both H_∞ and LQR designs produced very fast responses, with settling times 2 and 3 seconds correspondingly in the height response. This results in significantly large undershoots in the elevator deflection and a also large overshoots in the throttle settings which would be an undesirable practice. However it should be noted that the model does not include both sensor and actuator dynamics. Sensors and actuators are typically second order under damped systems. Including these dynamics of these devices in the model will limit the effective bandwidth of the system and would result in smother and slower responses and will make the design feasible.

The robustness of the two designs with respect to speed variations was examined at 25, 30 and 35 m/s. Overall the variation of the results was remarkably low. Since H_∞ design was slightly faster it tends to produce a slightly higher overshoot (about 10%) relative to LQR controller at the same speed. Nonetheless the LQR design is state feedback based and therefore uses all five state variables whereas the H_∞ controller

in this case uses only four out the five state variables. Further improvements in the results can be achieved by scheduling the gains of the two controllers via the speed of the UAV.

CFD Modelling and Analysis

The identification of current state of the art wing morphing techniques capable of improving overall performance for a low speed UAVs was investigated as part of the literature review and it was derived that the concept of flow control would be further analysed for the X-RAE1 UAV. The key concept of flow control is to affect the flow-field round the UAV which has an impact on the aerodynamics and in turn can be used to reduce lift/drag ratio or produce a control force. Applying CFD analysis an investigation of the effect an embedded smart effector array on a UAV was carried out.

Using the Computational Fluid Dynamics Procedure defined in chapter six both a two and three dimensional models of the X-RAE1 unmanned aircraft wing were constructed. The first model is a reconstruction of the actual Wortmann FX63-137 wing which has a concave lower surface and is used to validate the CFD results against experimental data. The second model is the modified Wortmann FX63-137 with an embedded effector array to modify the air flow. Prior to creating the second model the position of the distributed effector array was tested to specify the optimal position for increased lift and was found to be at the trailing edge of the wing.

3D CFD analysis was then carried out on second model with the distributed effector array placed on the trailing edge. The lift, drag and moments coefficients were compared to the un-modified 3D model and the contours around the wing were used to help illustrate the flow around the models. It was found that there were two significant improvements to the aerodynamic coefficients for the modified wing with the embedded effector array. The lift coefficient favoured well with lower angles of attack having an increased lift coefficient with an average of 0.155 between angle of attack 0 and -10.5.

There was also an overall increase in drag in the modified wing with an average increase of 0.005 which counteracted the increased lift for low angles of attack. Nevertheless at high angles of attack there was a significant increase of the C_L / C_D ratio which would have a positive effect and delay the stall of the UAV.

7.2 Recommendations for Future Work

Wing morphing is a promising technology, because it allows the aerodynamic potential of an aircraft wing to be explored, by adapting the wing shape for several flight conditions encountered in a typical mission profile. Moreover, the aero-elastic deformations can increase the performance and manoeuvrability, and improve the structural efficiency.

The overall research aim of the future work in this area is to improve the manoeuvrability of UAVs through the use of sophisticated control and wing morphing. Below are recommendations for future work:

1. More detailed control studies can be undertaken based on strict performance and robust stability requirements and validated through simulation based on the full nonlinear model and numerous flight regimes.

2. Investigate the control requirements for wing morphing by redesigning the flight control system of the modified UAV.

3. To further investigate the placement of the “smart effector array” at different flight regimes and design a flight control system capable of actively setting the required elements accordingly.

4. To decide the type of smart effector array to be implemented (shape memory alloys, synthetic jets, dimples, etc.) by carrying out a study on the energy and performance requirement. Once the selected smart effector array is constructed and embedded into the wing, validate the CFD analysis against wind tunnel testing.

CHAPTER

8

Appendices

The appendices A.1 through to A.9 cover the derivation and correction of both the longitudinal and lateral aerodynamic derivatives. These being listed as follows :

Appendix A.1 : Longitudinal Aerodynamic Derivatives
Appendix A.2 : Derivatives Due To Sideslip
Appendix A.3 : Derivatives Due to Rate of Roll
Appendix A.4 : Derivatives Due to Rate of Yaw
Appendix A.5 : Derivatives Due to Aileron Deflection
Appendix A.6 : Derivatives Due to Rudder Deflection
Appendix A.7 : X-RAE1 Useful Details
Appendix A.8 : Calculation of Centre of Pressure of Fin
Appendix A.9 : Lift-Curve of Wing and Fin

A.1.1 Longitudinal Aerodynamic Derivatives

The longitudinal aerodynamic derivatives of X-RAE1 are estimated in this section. Most of the estimation is based on static wind – tunnel tests of a model fitted with the modified wing with rounded tips.

X-RAE1 longitudinal geometry
$S = 0.9307\,\mathrm{m}^2$
$c = 0.353\,\mathrm{m}$
$S_t = 0.2576\,\mathrm{m}^2$
$l = 1.228\,\mathrm{m}$
$\mathrm{l_n} = 1.093\,\mathrm{m}$
$l_t = 1.182\,\mathrm{m}$
$h_0 = 0.207$
$h = 0.337$
$h_n = 0.589$
$h_{n_0} = 0.382$
$x' = -0.046\,\mathrm{m}$

Table 8-1 Longitudinal geometry (Trebble, 1985b)

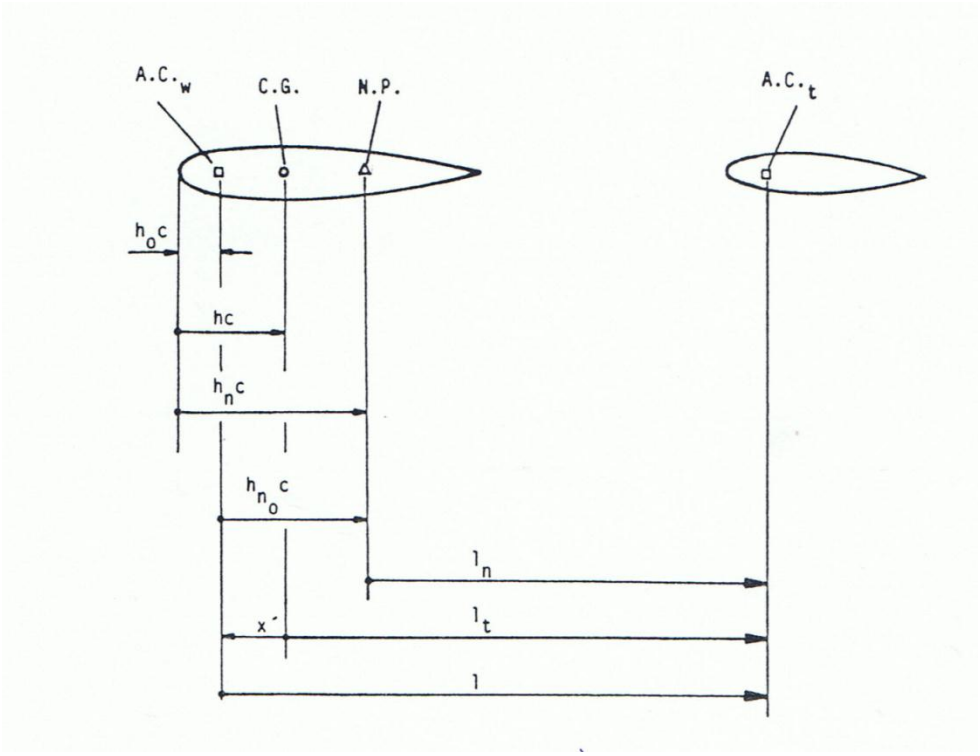

Figure 8-1 X-RAE1 longitudinal geometry ((Trebble 1985)

Reference wing / modified wing ratio	
S_r/S	0.989
c_r/c	1.006

Table 8-2 Reference wing to modified wing ratio

$\bar{V} = \frac{S_t l}{Sc} = 0.963$
$F = \frac{ch_{n_0}}{l_n} = 0.123$
$V_T' = \frac{\bar{V}}{1+F} = 0.858$
$k_n = -\frac{\partial C_m}{\partial C_L} = 0.25$
$H_n = h_n - h = 0.25$

Table 8-3 X-RAE1 parameters for the estimation of the longitudinal derivatives (Klein, 1979)

A.1.2 Lift Derivatives

Lift derivative w.r.t Angle of attack ((Klein, 1979))

$$C_{L_\alpha} = \frac{\partial C_L}{\partial \alpha} = a + \frac{S_t}{S} a_1 (1 - \frac{\partial \varepsilon}{\partial \alpha})$$

$$C_{L_\alpha} = \frac{\partial C_L}{\partial \alpha} = a + aF$$

Where:

$$\frac{\partial \varepsilon}{\partial \alpha} = 0.43 \text{ (ref 3)} \tag{1}$$

$$a = \frac{\partial C_{L_W}}{\partial \alpha} = \frac{(1.12 - 0.4)}{(4.4 + 4.8)} * \frac{360}{2\pi} * \frac{S_r}{S} = 4.43/\text{rad} \tag{2}$$

$$a_1 = \frac{\partial C_{L_t}}{\partial \alpha_t} = aF \frac{S}{S_t (1 - \partial \varepsilon / \partial \alpha)} = 3.45/\text{rad} \text{ (Ref. 1)} \tag{3}$$

Then:

$$\boxed{\begin{aligned} C_{L_\alpha} &= \frac{\partial C_L}{\partial \alpha} + \frac{\partial C_L}{\partial \alpha} F \\ &= 4.43 + (4.43 * 0.123) \\ &= 4.97/\text{rad} \end{aligned}} \tag{4}$$

Lift Derivative w.r.t. Rate of the angle of attack

$$C_{L_{\dot\alpha}} = C_{L_{\dot\alpha}}|_{\text{tail}} = \frac{\partial C_L}{\partial \left(\frac{\dot\alpha c}{2V_T} \right)}$$

$$= 2aF \frac{l}{c} \frac{\partial \varepsilon / \partial \alpha}{1 - \partial \varepsilon / \partial \alpha} = 2a_1 \frac{\partial \varepsilon}{\partial \alpha} \frac{l}{c} \frac{S_t}{S}$$

$$= 2 * 4.43 * 0.123 * \frac{1.228}{0.353} * \frac{0.43}{1 - 0.43}$$

$$= 2.856/\text{rad}$$

$$\boxed{C_{L_{\dot\alpha}} = 2.86/\text{rad}} \tag{5}$$

Lift Derivative w.r.t. Pitch Rate

$$C_{L_q} = C_{L_q}|_{wing} + C_{L_q}|_{tail}$$

Where:

$$C_{L_q}|_{wing} = \frac{2x'}{c} C_{L_{\alpha w}} = 2 * \frac{-0.046}{0.353} * 4.43 = -1.15/\text{rad} \tag{6}$$

$$C_{L_q}|_{tail} = 2aF \frac{l_t}{c} \frac{1}{(1 - \partial\varepsilon/\partial\alpha)} = 2 * 4.43 * 0.123 * \frac{1.182}{0.353} * \frac{1}{1 - 0.43} = 6.40/\text{rad} \tag{7}$$

Therefore:

$$\boxed{\begin{aligned} C_{L_q} &= -1.15 + 6.40 \\ &= 5.25/\text{rad} \end{aligned}} \tag{8}$$

Lift Derivative w.r.t Elevator Deflection

$$\begin{aligned} C_{L_\eta} &= \frac{c}{l_t} \frac{-K_n}{(1 - H_n c/lt)} / \frac{\partial\eta}{\partial C_L}\Big|_{C_m = 0} \\ &= \frac{0.353}{1.182} . \frac{-0.25}{(1 - \frac{0.25 * 0.353}{1.182})} / (-0.165) \\ &= 0.483/\text{rad} \end{aligned} \tag{9}$$

$$\boxed{C_{L_\eta} \triangleq \frac{\partial C_L}{\partial \eta} = 0.48/\text{rad}} \tag{10}$$

A.1.3 Pitching Moment Derivatives

Pitching Moment Derivative w.r.t. Angle of Attack

$$\boxed{\begin{aligned} C_{m_\alpha} &= -C_{L_\alpha} H_n \\ &= -4.97 * 0.25 \\ &= -1.24/\text{rad} \end{aligned}} \tag{11}$$

Pitching Moment Derivative w.r.t Rates of the Angle of Attack

$$C_{m_{\dot{\alpha}}} = C_{m_{\dot{\alpha}}}|_{tail} = -\frac{l_t}{c} C_{L_{\dot{\alpha}}}|_{tail}$$
$$= -\frac{1.182}{0.353} * 2.856$$
$$= -9.56 \text{ /rad}$$

$$\boxed{C_{m_{\dot{\alpha}}} \triangleq \frac{\partial C_m}{\partial(\frac{\dot{\alpha} c}{2V_T})} = -9.56 \text{/rad}} \quad (12)$$

Pitching Moment Derivative w.r.t. Pitch Rate

$$C_{m_q} = C_{m_q}|_{wing} + C_{m_q}|_{tail}$$

Where:

$$C_{m_q}|_{wing} = -\frac{|x'|}{c} C_{L_q}|_{wing} = -\frac{0.046}{0.353} * -1.15 = 0.15 \text{/rad}$$
$$C_{m_q}|_{tail} = -\frac{l_t}{c} C_{L_q}|_{tail} = -\frac{1.182}{0.353} * 6.40 = -21.43 \text{/rad}$$

Then from Table A.1-1 and Equations 6 and 7, C_{m_q} becomes:

$$\boxed{C_{m_q} \triangleq \frac{\partial C_m}{\partial(\frac{qc}{2V_T})} = -21.28 \text{/rad}} \quad (13)$$

Pitching Moment Derivative w.r.t. Elevator Deflection

$$C_{m_\eta} = -\frac{l_t}{c} C_{L_\eta}$$
$$= -\frac{1.182}{0.353} * 0.483$$
$$= -1.617 \text{/rad}$$

So (Table A.1-1, equation 10):

$$\boxed{C_{m_\eta} \triangleq \frac{\partial C_m}{\partial \eta} = -1.62 \text{/rad}} \quad (14)$$

A.1.4 Drag Derivatives

Drag is estimated from the formula

$$C_D = C_{D_0}\frac{S_r}{S} + kC_{L_w}^2\left(\frac{S}{S_r}\right)^2$$

For the drag coefficient, where C_{D_0} is computed by applying regressional analysis to wind tunnel data ((Trebble, 1985b).

Assuming profile drag is constant Then:

$$C_{D_0} = 0.0227\frac{S_r}{S} = 0.02245 \text{ and}$$

$$k = 0.0514\left(\frac{S}{S_r}\right)^2 = 0.0520$$

Therefore:

$$C_D = 0.02245 + 0.0520C_{L_w}^2 \qquad (15)$$

According to Equation 15 the derivative of the drag coefficient with respect to angle of attack is:

$$\boxed{C_{D_\alpha} \triangleq \frac{\partial C_D}{\partial \alpha} = 2kC_{L_w}C_{L_{\alpha w}} = 0.4607C_{L_w} \text{/rad}} \qquad (16)$$

If the <u>viscous drag</u> coefficient is defined as

$$C_{D'} = C_D - \frac{C_L^2}{\pi A} \qquad \text{then}$$

$$\boxed{C_{D'_\alpha} \triangleq \frac{\partial C_{D'}}{\partial \alpha} = (0.466 - \frac{2}{\pi A}C_{L_{\alpha w}})C_{L_w} = 0.0837C_{L_w} \text{/rad}} \qquad (17)$$

A.1.5 Engine Model (from (Milonidis, 1987) for completion)

<u>Thrust Components</u>

An analytical method for the computation of the thrust characteristics of X-RAE1 is used. A graphical method, as opposed to the analytical one, is impossible to be used due to lack of sufficient data.

The available power p_{av} for a fixed pitch propeller is given by the formula (Von Mises, 1959):

$$\boxed{p_{av} = \frac{M_{br}}{r \tan \beta'} V_T - \frac{\alpha_P S_P}{S \sin^3 \beta'} \frac{W}{V_1^2} V_T^3} \quad (18)$$

Where:

M_{br} : Brake torque moment.

r : Distance of a representative blade element of the propeller from the axis of rotation.

β' : Representative blade setting angle w.r.t. the zero lift direction of the blade profile.

α_P : Zero lift drag coefficient of the propeller profile.

S_P : Blade area.

S : Wing area.

W : Weight of the UAV – assumed constant.

V_1 : $V_1^2 = 2W / \rho S$

If the altitude effects are ignored, p_{av} becomes:

$$\boxed{p_{av} = k_1 \delta_T V_T - k_2 V_T^3} \quad (19)$$

Where:

$k_1 = [M_{br}$ (full throttle)$] / r \tan \beta'$

δ_T : throttle setting (from 0 to 1).

k_2 : constant to be computed.

$r \tan \beta' \simeq p / 2$ and p is the propeller pitch.

Computation of k_1

Assume that p_{br} (full throttle) is 50% of 1.9Kw at 14000PM (losses not modelled in the p_{av} equation and bad engine performance, Table 3.1)

Then:

$$M_{br} \text{ (full throttle)} = p_{br} \text{ (full throttle)} / 2\pi n$$

Where:

p_{br} (full throttle) = 950 Watts and

n = 14000RPM = 14000/60 $\sec^{-1}$ (Table 3.1)

k_1 then becomes: $p_{av} = k_1 = p_{br}(\text{f.t.}) / pn$ (p=6inches), i.e.:

$$k_1 = 26.7154\,\text{Wsec/m} \tag{20}$$

Computation of k_2

If a maximum speed of 40 m/sec is assumed, the required power p_{re} for an UAV mass of 18.5 Kg is:

$$p_{re} = \frac{1}{2}\rho V_T^2 S C_D V_T = 896.0\,\text{Watts}$$

Where:

$$C_D = C_{D_0} + kC_L^2$$

$$C_L = \frac{2W}{\rho V_T^2 S}$$

$$W = mg = 18.5g$$

Allow a throttle margin and an all-up weight greater than 18.5 Kg.

So, assume:

p_{av} =900 Watts at 35 m/sec, full throttle. (21)

Then Eqns 19, 20 and 21 give:

$$k_2 = 0.0055\,\text{W(m/sec)}^{-3} \tag{22}$$

If T is the thrust produced by the propeller, $T = p_{av} / u$ and according to Eqns 19, 20 and 21 the thrust model is

$$\boxed{T = 26.7154\delta_T - 0.0026u^2} \tag{23}$$

A.1.6 Derivatives Due to Thrust

Thrust Derivative w.r.t. the Velocity

According to Eqn 23:

$$\boxed{\frac{\partial T}{\partial V_T} = -0.0052 V_T} \tag{24}$$

Thrust Derivative w.r.t. Throttle Settings

$$\boxed{\frac{\partial T}{\partial \delta_T} = 26.7154} \tag{25}$$

Appendix A.2 : Derivatives Due To Sideslip

A.2.1 Derivatives due to sideslip (from (Milonidis, 1987) for completion)

ESDU Data Sheets are used for the estimation of the lateral derivatives due to sideslip. All the derivatives are assumed to be given in stability axes unless it is stated otherwise.

Side Force Derivatives due to sideslip (Y_V)

$$Y_V = \frac{\partial Y}{\partial V} / \frac{1}{2}\rho V_T S$$

Wing-Body Side Force Derivative Due to Sideslip (Item 79006)

$$\frac{|z|}{h} = \frac{|h_0|}{H} = 0.139 \text{ (Apx A.7)}$$

$$\frac{2b}{H+W} = 11.04 \quad \text{(Apx A.7)}$$

Then $F = 0.012$ (Item 79006)

$$A = 7.48 \quad \text{(Apx A.7)}$$

$$\lambda = 0.87 \quad \text{(Apx A.7)}$$

Then $F_W = 0.820$ (Item 79006)

$$-Y_{vWB} = [0.0714 + 0.674\frac{h^2}{S_{bs}} + \frac{hbFF_w}{S_{bs}}(\frac{4.95|z|}{h} - 0.12)]\frac{S_{bs}}{S} \quad \text{(Item 79006)}$$

$$= [0.0714 + 0.674\frac{H^2}{S_{bs}} + \frac{HbFF_w}{S_{bs}}(4.95\frac{|h_0|}{H} - 0.12)]\frac{S_{bs}}{S}$$

$$= 0.1085 \text{ (Apx A.7)}$$

Therefore:

$$\boxed{Y_{vWB} = -0.1085}$$

Contribution of Fin to Side Force Derivative Due to Sideslip in the presence of Body Wing and Tailplane (Item 82010)

From Apx A.8:

$J_B = 0.7513$

$J_T = 1.304$

$J_W = 0.91$

$C_{L_{\alpha F}} = 1.88/\text{rad}$

$\mathrm{S_F} = 0.1093\ m^2$

Then:

$$Y_{vF} = -J_B J_T J_W C_{L_{\alpha F}} \frac{\mathrm{S_F}}{S} = -0.1969$$

$$\boxed{Y_{vF} = -0.1969}$$

Side Force Derivative Due to Sideslip for complete Aircraft (Item 82011)

$$\boxed{Y_v = Y_{vWB} + Y_{vF} = -0.3054}$$

A.2.2 Rolling Moment Derivative Due to Sideslip (L_v)

$$L_v = \frac{\partial L}{\partial v} / \frac{1}{2}\rho V_T S b$$

Effects of Isolated Body (L_{vb}) and Wing-Body Interference (L_{vh}) on Rolling Moment Due to Sideslip (Item 73006)

Isolated Body

$$L_{vb} = -0.014 \frac{l_b}{b} \frac{S_{bm}}{S} a_b = -0.0005\alpha_b \text{ (Apx A.7)}$$

Where:

α_b : Body incidence measured from its zero-lift value (in degrees)

$$\boxed{L_{vb} = -0.0005\alpha_b}$$

Wing-body interference

$$\frac{h_0}{H} = -0.139 \text{ (Apx A.7)}$$

$$\frac{H}{b} = 0.125 \quad \text{(Apx A.7)}$$

$$\frac{W}{H} = 0.449 \quad \text{(Apx A.7)}$$

$$l = \frac{L_{vh}}{(l + W/H) f(A)} = -0.0076 \text{ (Item 73006)}$$

A=7.48 then (Item 73006), f(A)=1.08

Therefore:

$$\boxed{L_{vh} = -0.0119}$$

Contribution of Wing Planform to Rolling Moment Derivative Due to Sideslip (L_{vW}) (Item 80033)

$$L_{vW} = [L_{vW}]_0 + [L_{vW}]_{\Lambda\frac{1}{2}}$$

$$\Lambda\frac{1}{2} = 1.13$$

Then

$$\lambda = 0.87$$

$$-\frac{L_{vW}}{C_L} = 0.0074$$

Therefore:

$$\boxed{L_{vW} = -0.0074 C_L}$$

Where C_L is the wing lift coefficient.

Contribution of Fin to Rolling Moment Derivative Due to Sideslip L_{vF} (Item 82010)

$$L_{vF} = Y_{vF}(\bar{z}_F \cos\alpha - \bar{l}_F \sin\alpha)/b$$

Where:

α : angle between stability x-axis and longitudinal body axis (ie. Angle of attack)

Then (Apx A.80, the rolling moment derivative due to sideslip becomes:

$$\boxed{L_{vF} = \frac{-0.1969(8.87\cos\alpha - 109.51\sin\alpha)}{263.8}}$$

Estimation of Rolling Moment Derivative Due to Sideslip for Complete Aircraft at subsonic speeds (Item 81032)

$L_v = L_{vb} + L_{vh} + L_{vW} + L_{vF}$ so,

$$\boxed{L_v = -0.0005\alpha_b - 0.0119 - 0.0074C_L - 0.1969(8.87\cos\alpha - 109.51\sin\alpha)/263.8}$$

A.2.3 Yawing Moment Derivative Due to Sideslip (N_v) (from (Milonidis, 1987) for completion)

$$N_v = \frac{\partial N}{\partial v} / \frac{1}{2}\rho V_T S b$$

Wing-Body Yawing Moment Derivative Due to Sideslip (N_{vWB}) (Item 79006)

$$-N_{v_{mid}} = [0.2575 + \frac{l_b^2}{S_{bs}}(0.0008\frac{l_b^2}{S_{bs}} - 0.024)][1.39\frac{h_1^{\frac{1}{2}}}{h_2^{\frac{1}{2}}} - 0.39]\frac{S_{bs}l_b}{Sb}$$

$$= 0.0515 \text{ (Apx A.7)}$$

$$N_{vWB} = N_{v_{mid}} + \frac{l - 0.5l_b}{b} Y_{vWB} \text{ (Item 79006)}$$

Where

l : distance of C.G. from the nose of fuselage ($l = 0.681\text{m}$)

Then

$$\boxed{N_{vWB} = -0.0363}$$

Contribution of Fin to Yawing Moment Derivative Due to Sideslip (N_{vF}) (Item 82010)

$$N_{vF} = -Y_{vF}(\bar{l}_F \cos\alpha + \bar{z}_F \sin\alpha)/b$$

Where:

α : angle between stability x-axis and longitudinal body axis (ie. Angle of attack)

Then according to Apx A.8, N_{vF} is:

$$\boxed{N_{vF} = 0.1969(109.51\cos\alpha + 8.87\sin\alpha)/263.8}$$

Estimation of Yawing Moment Derivative Due to Sideslip for Complete Aircraft at subsonic speeds (Item 82011)

$N_v = N_{vWB} + N_{vF}$ so,

$$\boxed{N_v = -0.0363 + 0.1969(109.51\cos\alpha + 8.87\sin\alpha)/263.8}$$

Appendix A.3 : Derivatives Due to Rate of Roll

A.3.1 Derivatives Due to Rate of Roll (from (Milonidis, 1987) for completion)

The lateral derivatives due to rate of roll are estimated in this appendix using ESDU Data Sheets. All the derivatives are assumed to be given in stability axes unless it is stated otherwise.

Side Force Derivatives due to Rate of Roll (Y_p)

$$Y_p = \frac{\partial Y}{\partial p} / \frac{1}{2}\rho V_T S b$$

Contribution of Wing planform to Side Force Derivative Due to Rate of Roll (Y_{pW}) (Item 81014)

$$\frac{x_{ac}}{b} = \frac{x'}{b} = -0.0174 \ \text{(Apx A.1)}$$

$$-[\frac{Y_{pW}}{C_L}]_0 = 0.078 \ \text{(Item 81014)}$$

Therefore:

$$\boxed{Y_{pW} = 0.078 C_L}$$

Contribution of Fin to Side Force Derivative Due to Rate of Roll (Y_{pF}) (Item 83006)

$$\frac{b_t}{h_F} = 3.16 \ \left(\text{Apx A.8}\right)$$

$$\frac{z_T}{z_F} = 1 \qquad \left(\text{Apx A.8}\right)$$

$$K_1 = 0.625 \ \left(\text{Item 83006}\right)$$

Then,

$$K_2 = 0.975 \ \left(\text{Item 83006}\right)$$

$$K_3 = 1 \qquad \left(\text{Item 83006}\right)$$

Then (Item 83006)

$$Y_{pF} = -(k_1 + k_2 k_3)\frac{S_F h_F}{Sb}\left[\frac{(\bar{z}_{\underset{F}{*}} \cos\alpha - \bar{l}_{\underset{F}{*}} \sin\alpha)/b - \partial\bar{\sigma}_W / \partial(pb/V_T) - \partial\bar{\sigma}_\alpha / \partial(pb/V_T)}{(\bar{z}_{\underset{F}{*}} - \bar{z}_{crF})/b}\right]$$

Where:

α : angle between stability x-axis and longitudinal body axis (ie. Angle of attack).

$\partial\bar{\sigma}_W / \partial(pb/V_T)$: Sidewash term due to wing (independent from angle of attack variations).

$\partial\bar{\sigma}_\alpha / \partial(pb/V_T)$: sidewash term due to body (function of angle of attack). It is given w.r.t. $k = [\bar{z}_{\underset{F}{*}} - (\bar{z}_{\underset{F}{*}} \cos\alpha - \bar{l}_{\underset{F}{*}} \sin\alpha)]/b$ (*Item* 83006)

According to Apx A.8, Y_{pF} becomes:

$$\boxed{Y_{pF} = -0.3133[(11.32\cos\alpha - 110.19\sin\alpha)/263.8 - 0.18 - \partial\bar{\sigma}_\alpha / \partial(pb/V_T)]}$$

Estimation of Side Force Derivative Due to Rate of Roll for Complete Aircraft (Item 85010)

$$Y_p = Y_{pW} + Y_{pF}$$

$$\boxed{Y_p = 0.078C_L - 0.3133[(11.32\cos\alpha - 110.19\sin\alpha)/263.8 - 0.18 - \partial\bar{\sigma}_\alpha / \partial(pb/V_T)]}$$

A.3.2 Rolling Moment Derivative Due to Rate of Roll (L_p) (from (Milonidis, 1987) for completion)

$$L_p = \frac{\partial L}{\partial p} / \frac{1}{2}\rho V_T S b^2$$

Rolling Moment Derivative Due to Rate of Roll for swept and tapered wings (L_{pW}) (Item A.06.01.01)

$$\beta = (1 - M^2)^{\frac{1}{2}} = 1$$

$$k = \frac{\beta(\alpha_{l0})_M}{2\pi} = 1$$

$(\alpha_{l0})_M$ **:** two dimensional lift-curve slope ($\simeq 2\pi$)

$$\frac{\beta A}{k} \simeq A = 7.48 \quad \text{(Apx A.7)}$$

$$\Lambda_E \simeq \tan^{-1}(\tan \Lambda_{\frac{1}{4}}) = 1.66^0 \quad \text{(Apx A.7)}$$

$$\lambda = 0.87 \quad \text{(Apx A.7)}$$

Then (Item A.06.01.01)

$$\boxed{L_{pW} = -0.2438}$$

Contribution of Fin to Rolling Moment Derivative Due to Rate of Roll (L_{pF}), in the presence of Body, Wing and Tailplane (Item 83006)

$L_{pF} = Y_{pF}(\overline{z}_{\underset{F}{*}} \cos\alpha - \overline{l}_{\underset{F}{*}} \sin\alpha)/b$ therefore (Apx A.8):

$$\boxed{L_{pF} = Y_{pF}(11.32\cos\alpha - 110.19\sin\alpha)/263.8}$$

Contribution of Tailplane to Rolling Moment Derivative Due to Rate of Roll L_{pT} *(Item 83006, A.06.01.01)*

From Item A.06.01.01, $L_{pT} = -01.27$ based on S_t and b_t.

Then:

$L_{pT} = -0.127 * 0.5 S_t b_t^2 / S b^2$ Hence (Apx A.7):

$$\boxed{L_{pT} = -0.0019}$$

Estimation of Rolling Moment Derivative Due to Rate of Roll for Complete Aircraft (Item 85010)

$$L_p = L_{pW} + L_{pW} + L_{pF} + L_{pT} \qquad \text{so,}$$

$$\boxed{L_p = -0.2457 + Y_{pF}(11.32\cos\alpha - 110.19\sin\alpha)/263.8}$$

A.3.3 Yawing Moment Derivative Due to Rate of Roll (N_p)

$$N_p = \frac{\partial N}{\partial p} / \frac{1}{2}\rho V_T S b^2$$

Contribution of Wing Planform to Yawing Moment Derivative Due to Rate of Roll (N_{pW}) (Item 81014)

Linear contribution to N_{pW}

$$[\frac{N_{pW}}{C_L}]_0 = -0.034 \ \ (\text{Item}\,81014, \text{Fig.}1)$$

Nonlinear contribution to N_{pW}

$$[\frac{N_{pW}}{\frac{\partial C'_D}{\partial \alpha}}]_0 = 1.23 \ \ (\text{Item}\,81014, \text{Fig.}3)$$

Where $\frac{\partial C'_D}{\partial \alpha}$: viscous drag-curve slope (per degrees).

Then

$$\boxed{N_{pW} = -0.034 C_L + 1.23\frac{\partial C'_D}{\partial \alpha}}$$

Contribution of Fin to Yawing Moment Derivative Due to Rate of Roll (N_{pF}) in the presence of Body, Wing and Tailplane (Item 85010)

$$N_{pF} = -Y_{pF}(\bar{l}_{\substack{* \\ F}} \cos\alpha + \bar{z}_{\substack{* \\ F}} \sin\alpha)/b$$

Hence:

$$\boxed{N_{pF} = -Y_{pF}(110.19\cos\alpha + 11.32\sin\alpha)/263.8}$$

Estimation of Yawing Moment Derivative Due to Rate of Roll for Complete Aircraft (Item 85010)

$N_p = N_{pW} + N_{pF}$ so,

$$\boxed{N_p = -0.034C_L + 1.23\frac{\partial C_D'}{\partial \alpha} - Y_{pF}(110.19\cos\alpha + 11.32\sin\alpha)/263.8}$$

Appendix A.4 : Derivatives Due to Rate of Yaw

A.4.1 Derivatives Due to Rate of Yaw (from (Milonidis, 1987) for completion)

The derivatives due to rate of yaw are estimated in this appendix. Their derivation is based on ESDU Data Sheets. All the derivatives are assumed to be given in stability axes.

Side Force Derivatives due to Rate of Yaw (Y_r)

$$Y_r = \frac{\partial Y}{\partial r} / \frac{1}{2}\rho V_T S b$$

Contribution of Body to Side Force Derivative Due to Rate of Yaw (Y_{rB}) (Item 83026)

$$Y_{rB} = -0.04\frac{S_{bs} l_b}{Sb} \quad \text{therefore (Apcs A.7 and A.8):}$$

$$\boxed{Y_{rB} = -0.0109}$$

Contribution of Fin to Side Force Derivative Due to Rate of Yaw (Y_{rF}) (Item 82017)

$$Y_{rF} = -[Y_{vF}]_{J_w=1}(\bar{l}_F \cos\alpha + \bar{z}_F \sin\alpha)/b$$

From Apx A.2(section 1.2), $[Y_{vF}]_{J_w=1} = -0.2164$. Then Y_{rF} becomes (Apcs A.7 and A.8):

$$\boxed{Y_{rF} = 0.2164(109.51\cos\alpha + 8.87\sin\alpha)/263.8}$$

Estimation of Side Force Derivative Due to Rate of Yaw for Complete Aircraft (Item 84002)

$$Y_r = Y_{rB} + Y_{rF}$$

$$\boxed{Y_r = -0.0109 + 0.2164(109.51\cos\alpha + 8.87\sin\alpha)/263.8}$$

A.4.2 Rolling Moment Derivative Due to Rate of Yaw (L_r)

$$L_r = \frac{\partial L}{\partial r} / \frac{1}{2}\rho V_T S b^2$$

Effect of Wing on Rolling Moment Derivative Due to Rate of Yaw (L_{rW}) (Item 72021)

$$L_{rW} = L_{rp} + L_{r\Gamma} + L_{r\varepsilon} + L_{rf}$$

Where:

L_{rp}: due to wing planform

$L_{r\Gamma}$: due to dihedral $L_{r\Gamma} = 0$

$L_{r\varepsilon}$: due to wing twist

L_{rf} :due to flaps (L_{rf} =0, flaps not deflected)

$$\frac{L_{rp}}{C_L} = \frac{1}{g(\Lambda_{\frac{1}{4}})} \frac{L_{rp}}{C_L} * g(\Lambda_{\frac{1}{4}})$$

$$\frac{1}{g(\Lambda_{\frac{1}{4}})} \frac{L_{rp}}{C_L} = 0.1219 \quad (\text{Item } 72021 \text{fig.1a})$$

$$g(\Lambda_{\frac{1}{4}}) = 1.02 \text{ (Item } 72021 \text{fig.1b)}$$

Hence L_{rp} =$0.1243\,C_L$

$L_{r\varepsilon} = -0.00185 / \text{degree}$

Then, for $g(\Lambda_{\frac{1}{4}}) = 1.02$ and $\varepsilon = 1^\circ$ washout, $L_{r\varepsilon} = -0.00189$

So

$$\boxed{L_{rW} = 0.1243 C_L - 0.00189}$$

Contribution of Fin to Rolling Moment Derivative Due to Rate of Roll (L_{rF}) (Item 82017)

$$L_{rF} = Y_{rF}(\bar{z}_F \cos\alpha - \bar{l}_F \sin\alpha) / b$$

So, from Apx A.8

$$\boxed{L_{rF} = Y_{rF}(8.87\cos\alpha - 109.51\sin\alpha)/263.8}$$

Estimation of Rolling Moment Derivative Due to Rate of Yaw for Complete Aircraft (Item 84002)

$$L_r = L_{rW} + L_{pF} \qquad \text{so:}$$

$$\boxed{L_r = -0.00189 + 0.1234C_L + Y_{rF}(8.87\cos\alpha - 109.51\sin\alpha)/263.8}$$

A.4.3 Yawing Moment Derivative Due to Rate of Yaw (N_r)(from (Milonidis, 1987) for completion)

$$N_r = \frac{\partial N}{\partial r} / \frac{1}{2}\rho V_T S b^2$$

Contribution of Body to Yawing Moment Derivative Due to Rate of Yaw (N_{rB}) (Item 83026)

$$N_{rB} = -0.01\frac{l_b^2 S_{bs}}{b^2 S} \qquad \text{therefore (Apx A.7)}$$

$$\boxed{N_{rB} = -0.0022}$$

Effect of Wing on Yawing Moment Derivative Due to Rate of Yaw (N_{rW}) (Item 71017)

$$N_{rW} = \frac{N_{r_0}}{C_{D_0}} C_{D_0} + \frac{N_{r_v}}{C_L^2} C_L^2$$

$$A = 7.48, \lambda = 0.87, \Lambda_{\frac{1}{4}} = 1.66^\circ$$

$$(\frac{N_{r_0}}{C_{D_0}})_{\lambda=1} = -0.168 \quad (\text{Item } 71017 \text{ Fig.1a})$$

$$(\frac{(N_{r_0}/C_{D_0})_{\lambda=0.87}}{(N_{r_0}/C_{D_0})_{\lambda=1}}) = 0.9675 \quad (\text{Item } 71017 \text{ Fig.1b})$$

$$(\frac{N_{r_0}}{C_{D_0}}) = -0.1621$$

$$(\frac{N_{r_v}}{C_L^2})_{\lambda=0.5} = -0.008 \quad (\text{Item } 71017 \text{ Fig. 2c})$$

$$(\frac{N_{r_v}}{C_L^2})_{\lambda=1} = -0.01 \qquad (\text{Item } 71017 \text{ Fig. 2c})$$

$$\frac{N_{r_v}}{C_L^2} = -0.009$$

Hence

$$\boxed{N_{rW} = -0.1621 C_{D_0} - 0.009 C_L^2}$$

Contribution of Fin to Yawing Moment Derivative Due to Rate of Yaaw (N_{rF}) (Item 82017)

$$N_{rF} = -Y_{rF}(\bar{l}_F \cos\alpha + \bar{z}_F \sin\alpha)/b$$

So from Apx A.8:

$$\boxed{N_{rF} = -Y_{rF}(109.51\cos\alpha + 8.87\sin\alpha)/263.8}$$

Estimation of Yawing Moment Derivative Due to Rate of Yaw for Complete Aircraft (Item 84002)

$N_r = N_{rB} + N_{rW} + N_{rF}$ so,

$$\boxed{N_r = -0.0022 - 0.1621 C_{D_0} - 0.009 C_L^2 - Y_{rF}(109.51\cos\alpha + 8.87\sin\alpha)/263.8}$$

A.5.1 Derivatives Due to Aileron Deflection (from (Milonidis, 1987) for completion)

The rolling moment and yawing moment derivatives of X-RAE1 due to aileron deflection are given in this appendix. The side force due to aileron deflection is assumed negligible. All the derivatives are expressed in stability axes.

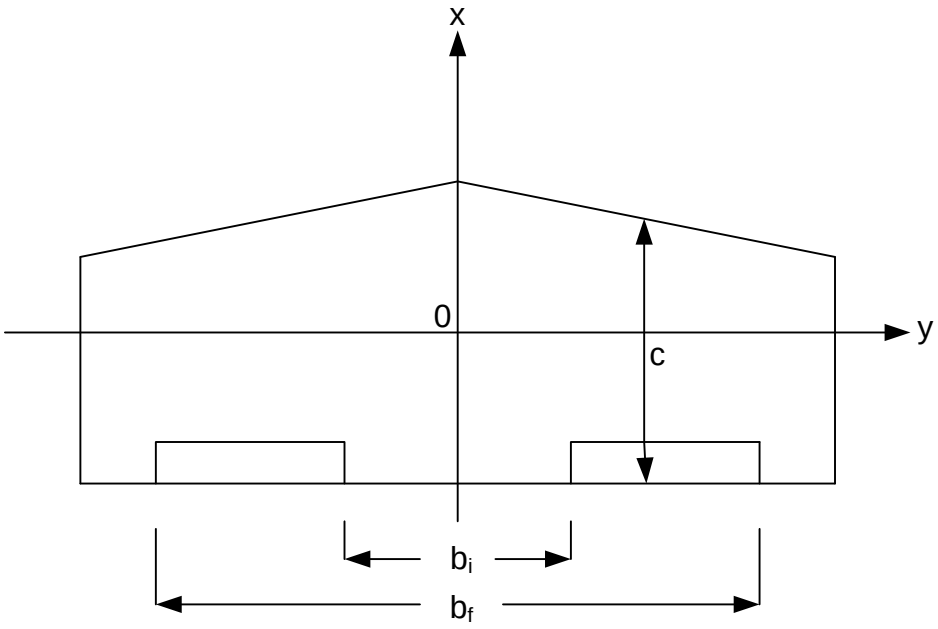

Fig. A.5-1 Aileron geometry of X-RAE1

$b_i = 0.4588\,\text{m}$

$b_f = 1.932\,\text{m}$

$c = 0.357\,\text{m}$

Rolling Moment Derivative Due to Aileron Deflection (L_ξ)

$$\frac{\partial L}{\partial \xi} = -\rho V_T^2 \frac{\partial C_L}{\partial \xi} c \int_{b_i/2}^{b_f/2} y dy$$

$$\frac{\partial C_L}{\partial \xi} = 1.79 \text{ /rad} \quad (\text{Apx A.9})$$

Then, $\frac{\partial L}{\partial \xi} = -\frac{1}{2}\rho V_T^2 0.5626$

$$\boxed{L_\xi = \frac{\partial L}{\partial \xi} / \frac{1}{2}\rho V_T^2 Sb = -0.2291/\text{rad}}$$

Yawing Moment Derivative Due to Aileron Deflection (N_ξ)

The yawing moment due to aileron deflection is caused by the difference on drag between up and down aileron (only vortex drag is assumed). Then, the components that produce the yawing moment are:

Starboard: $C_{L_0}\Delta C_L / \pi A$

Portboard: $-C_{L_0}\Delta C_L / \pi A$

Where:

$$\Delta C_L \triangleq \Delta L / \frac{1}{2}\rho V_T^2 S = \frac{c(b_f - b_i)}{S}\frac{\partial C_L}{\partial \xi}\xi \text{ (Fig. A.5-1)}$$

Then:

$$\frac{\partial N}{\partial \xi}\xi = \frac{1}{2}\rho V_T^2 \mathrm{S}\frac{C_{L_0}\Delta C_L}{\pi A} 2\mathrm{l_n} \text{ (Fig. A.5-1)}$$

$$\mathrm{l_n} = (b_f + b_i)/4 \text{ (Fig. A.5-1)}$$

Therefore $$\boxed{N_\xi = \frac{\partial N}{\partial \xi} / \frac{1}{2}\rho V_T^2 Sb = 0.0195 C_{L0} \text{ / rad}}$$

Where C_{L0}, is the lift coefficient about which the variation in lift coefficient due to aileron deflection takes place.

Appendix A.6 : Derivatives Due to Rudder Deflection

A.6.1 Derivatives Due to Rudder Deflection

The aerodynamic derivatives of X-RAE1 due to rudder deflection are estimated in this appendix. All the derivatives are given in body axes.

Side Force Derivatives due to Rudder (Y_ζ)

$$\frac{\partial Y}{\partial \zeta} = J_B J_T J_W \frac{\partial C_{L_F}}{\partial \zeta} \frac{1}{2} \rho V_T^2 S_F$$

Where

$\frac{\partial C_{L_F}}{\partial \zeta}$: lift curve slope of fin due to rudder deflection.

Then according to Apcs A.8 and A.9 Y_ζ becomes:

$$\boxed{Y_\zeta \triangleq \frac{\partial Y}{\partial \zeta} / \frac{1}{2} \rho V_T^2 S = 0.1393 / \text{rad}}$$

Rolling Moment Derivative Due to Rate of Yaw (L_ζ)

$\frac{\partial L}{\partial \zeta} = \frac{\partial Y}{\partial \zeta} \bar{z}_F$ so, according to Apx A.8

$$\boxed{L_\zeta \triangleq \frac{\partial L}{\partial \zeta} / \frac{1}{2} \rho V_T^2 S b = 0.00468 / \text{rad}}$$

Yawing Moment Derivative Due to Rate of Yaw (N_ζ)

$\frac{\partial N}{\partial \zeta} = -\frac{\partial Y}{\partial \zeta} \bar{l}_F$, so :

$$\boxed{N_\zeta \triangleq \frac{\partial N}{\partial \zeta} / \frac{1}{2} \rho V_T^2 S b = -0.0579 / \text{rad}}$$

Appendix A.7 : X-RAE1 Useful Details

A.7.1 X-RAE1 Geometry

Wing With Rounded Tips	
Area (S)	0.9307 m^2
Span (b)	2.638 m
Mean Chord (c)	0.353 m
Aspect Ratio (A)	7.48
Sweepback of Quarter chord ($\Lambda_{\frac{1}{4}}$)	1.66^o
Tapper Ratio (λ)	0.87
Distance of the Centre of Gravity from Leading edge of mean chord	0.121 m
Aileron	
Span	0.7336 m
Chord	0.055 m
Tailplane	
Area (S_t)	0.2576 m^2
Span (b_t)	0.860 m
Mean Chord (c_t)	0.2995 m
Tail Arm (l_t) (Distance of C.G. to tailplane mean quarter-chord)	1.182 m
Tail Volume ($S_t l_t / Sc$)	0.932
Elevator	
Span	0.860 m
Chord	0.063 m

Table 8-4 X-RAE1 geometry

A.7.2 Centre of Gravity Nominal Position, Cross-Sectional Areas and Side Elevation Area

C.G. Position and Useful Cross-Sectional Areas (Item 73006)

The centre of gravity is assumed to the centroid of the cross-section through the longitudinal position of it (0.34c aft of leading edge of mean chord).

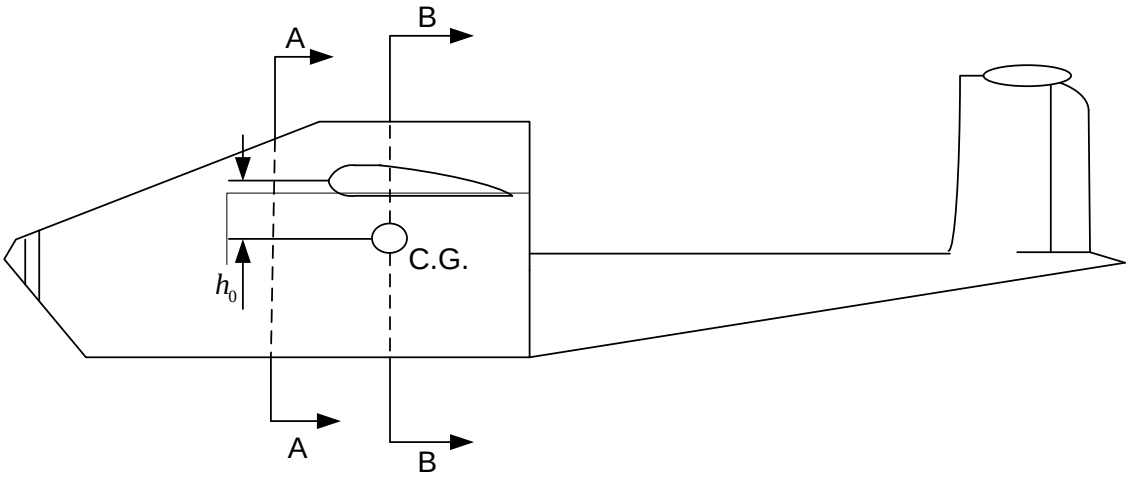

Fig. A.7-1 C.G. nominal position

h_0 : lateral distance of C.G. from mean quarter-chord (negative for C.G. below mean quarter chord).

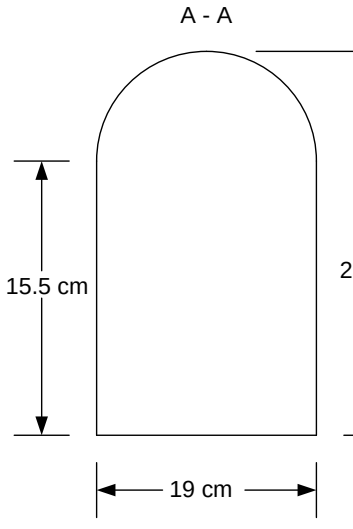

Figure 8-2 Maximum cross-sectional area (S_{bm}) =436.26 cm^2

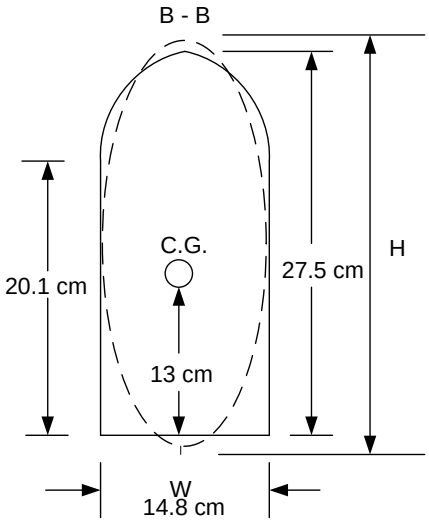

Figure 8-3 Equivalent elliptical area S_{BB} =383.5 cm^2

Side Elevation Area (Item 79006)

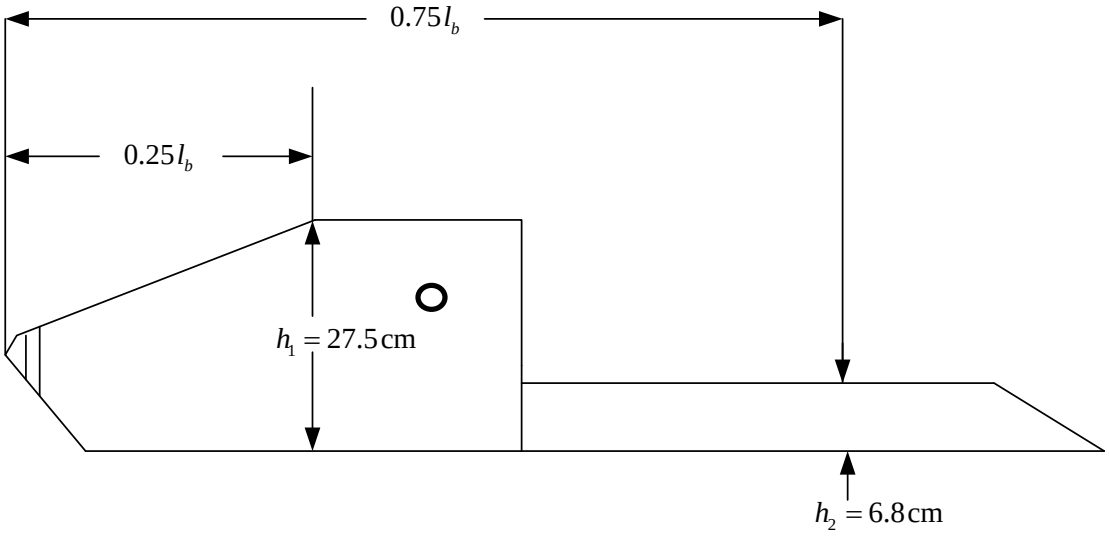

Figure 8-4 Side elevation area (S_{bs})

$$S_{bs} = 3187.65\,\text{cm}^2$$

Summary

Body Length (l_b)	210 cm
Maximum cross-sectional area (S_{bm})	436.26 cm^2
Equivalent height (H)	23.99 cm
Width (W)	14.8 cm
Lateral distance of C.G. from mean quarter –chord (h_0)	-2.84 cm
Side elevation area (S_{bs})	3187.65 cm^2

A.8.1 Lift-Curve Slope of Fin

(Items 82010, 70011)

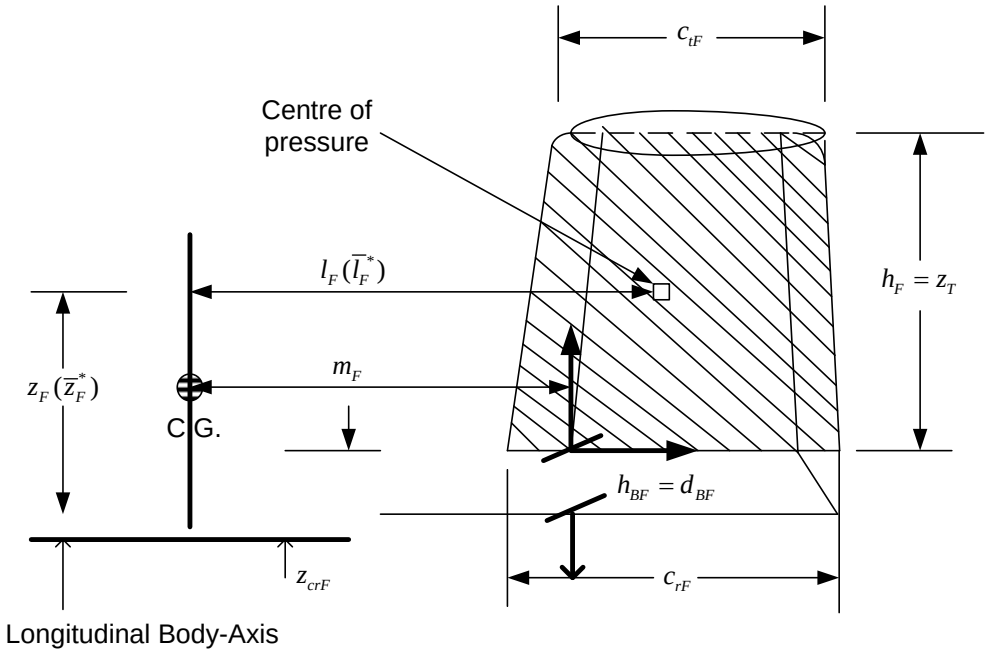

Figure 8-5 Geometry of X-RAE1 Fin

c_{rF}	44.0	cm
c_{tF}	33.2	cm
$h_F = z_T$	27.2	cm
$h_{BF} = d_{BF}$	6.0	cm
z_{crF}	-5.0	cm
$\Lambda_{\frac{1}{4}F}$	8.0^o	
m_F	107.9	cm

Table 8-5 Fin Characteristics

Then (Item 82010, Table A.8-1):

$S_F = h_F (c_{rF} + c_{tF}) / 2 = 1093.44\,\text{cm}^2$

$A_F = 2h_F^2 / S_F = 1.35$

$\lambda_F = c_{tF} / c_{rF} = 0.83$

$A_F \tan \Lambda_{\frac{1}{2}F} = A_F \tan \Lambda_{\frac{1}{4}F} - (1-\lambda_F)/(1+\lambda_F) = 0.0968$

$(1-M^2)^{\frac{1}{2}} A_F = 1.35$

Hence (Item 70011):

$$\boxed{C_{L_{\alpha F}} \triangleq \frac{\partial C_L}{\partial \alpha}|_{Fin} = 1.88/\text{rad}}$$

A.8.2 Calculation of J_B, J_T and J_W

(Item 82010)

$A_F = 1.35$

$h_{BF} / (h_{BF} + h_F) = 0.181$ $\qquad J_B = 0.7513$

$\frac{b_t}{h_F} = 3.16$ (Table A.7-1)

$\frac{z_F}{h_F} = 1$ $\qquad J_T = 1.304$

$\frac{z_W}{h_{BW}} = \frac{h_0}{H} = -0.139$ $\qquad J_W = 0.91$

A.8.3 Centre of Pressure of Fin (derivatives due to sideslip)

(Item 82010)

$\bar{z}_{Fl} = 0.6 h_F = 16.32\,\text{cm}$ (Item 82010)

Then

$\bar{l}_F = m_F + 0.7\bar{z}_{Fl} \tan \Lambda_{\frac{1}{4}F} = 109.51\text{cm}$ (Item 82010)

$\bar{z}_F = z_{crF} + 0.85\bar{z}_{Fl} = 8.87\,\text{cm}$ (Item 82010)

$$\boxed{\begin{aligned} \bar{l}_F &= 109.51\text{cm} \\ \bar{z}_F &= 8.87\,\text{cm} \end{aligned}}$$

A.8.4 Centre of Pressure of Fin (derivative due to rate of roll)

(Item 83006)

$\overline{l}_{*_{\mathrm{F}}} = m_F + 0.6\mathrm{h_F} \tan \Lambda_{\frac{1}{4}F} = 110.19\,\mathrm{cm}$ (Item 83006)

$\overline{\mathrm{z}}_{*_{\mathrm{F}}} = z_{crF} + 0.6\mathrm{h_F} = 11.32\,\mathrm{cm}$ (Item 83006)

$\overline{l}_{*_{\mathrm{F}}} = 110.19\,\mathrm{cm}$

$\overline{\mathrm{z}}_{*_{\mathrm{F}}} = 11.32\,\mathrm{cm}$

Appendix A.9 : Lift-Curve of Wing and Fin

A.9.1 Lift-Curve Slope of Wing Due to Aileron Deflection (from (Milonidis, 1987) for completion)

(Items W.01.01.05, C.01.01.03, C.01.01.04)

From Item W.01.01.05 ($\log_{10} R = 5.87$, out of range) and for trailing edge transition:

$$\frac{(\alpha_1)_o}{(\alpha_1)_{oT}} = 0.814$$

Where $(\alpha_1)_{oT} = \partial C_L / \partial \alpha$ for two-dimensional theoretical flow.

Also:

$$\frac{c_f}{c_l} = \frac{0.055}{0.357}$$

c_f :aileron chord

c_l : wing local chord

$t/c = 0.141$

$$(\alpha_2)_{oT} = 3.225 \ \text{(Item c.01.01.03)}$$

Where $(\alpha_2)_{oT} = \partial C_L / \partial \xi$ for two-dimensional theoretical flow.

Then from (1), (2) and Item C.01.01.03

$$\frac{(\alpha_2)_o}{(\alpha_2)_{oT}} = 0.67 \qquad \text{so, } (\alpha_2)_o = 2.16/\text{rad}$$

$$a_2 = \frac{\partial C_L}{\partial \xi} = (\alpha_2)_o \, f \ \text{(Item C.01.01.04)}$$

$$f = 0.83 \ \text{(Item C.01.01.04 no balance)}$$

Therefore:

$$\boxed{a_2 \triangleq \frac{\partial C_L}{\partial \xi} = 1.79/\text{rad}}$$

A.9.2 Lift-Curve Slope of Fin Due to Rudder Deflection

(Item 74011)

$(\frac{\partial C_L}{\partial \alpha})_{FT} = 1.88/\text{rad}$ (Apx A.8)

$\frac{c_f}{c} = 0.22$

$c_f = 0.092\,\text{m}$: rudder chord

$c = 0.42\,\text{m}$: local fin chord

$\frac{\partial C_L}{\partial \zeta} = 0.71(\frac{\partial C_L}{\partial \alpha})_{FT}$ (Item 74011)

Subscript T mean theoretical value, Then:

$$\boxed{\frac{\partial C_L}{\partial \zeta} = 1.13/\text{rad}}$$

CHAPTER

9

References

ABDULRAHIM, M., GARCIA, H. & LIND, R. 2005. Flight Characteristics of Shaping the MembraneWing of a Micro Air Vehicle. *JOURNAL OF AIRCRAFT,* 42.

ABZUG, M. J. & LARRABEE, E. E. 2005. *Airplane stability and control : a history of the technologies that made aviation possible,* Cambridge, UK ; New York, Cambridge University Press.

ADAMS, R. J. 1994. *Robust multivariable flight control,* London, Springer-Verlag.

AGASHE, J., ARNOLD, D. P. & CATTAFESTA, L. 2009. Development of Compact Electrodynamic Zero-Net Mass-Flux Actuators *AIAA,* 1308.

ALSWAILEM, S. 2003. *Application of Robust Control in Unmanned Vehicle Flight Control System Design.* PhD, Cranfield University,.

AMITAY, M., SMITH, D., KIBENS, V., PAREKH, A. & A., G. 2001. Aerodynamic flow control over an unconventional airfoil using synthetic jet actuators. *AIAA,* 39**,** 361-370.

ANDERSON, J. D. 2011. *Fundamentals of aerodynamics,* New York, McGraw-Hill.

ANTSAKLIS, P. J. & MICHEL, A. N. 1997. *Linear systems,* New York ; London, McGraw-Hill.

ARTHUR, G., MCKEON, B., DEARING, S., MORRISON, J. & CUI, Z. 2006. Manufacture of micro-sensors and actuators for flow control. *Microelectron. Eng.,* 83**,** 1205-8.

AUSTIN, F., ROSSI, M. J., VAN NOSTRAND, W., KNOWLES, G. & JAMESON, A. 1994. Static shape control for adaptive wings. *AIAA Journal,* 32**,** 1895-1901.

BABISTER, A. W. 1980. *Aircraft dynamic stability and response,* Oxford ; New York, Pergamon Press.

BARBARINO, S., BILGEN, O., AJAJ, R. M., FRISWELL, M. I. & INMAN, D. J. 2011. A Review of Morphing Aircraft. *Journal of Intelligent Material Systems and Structures,* 22**,** 823-877.

BENARD, N., MIZUNO, A. & MOREAU, E. 2009. A large-scale multiple dielectric barrier discharge actuator based on an innovative three-electrode design. *Phys. D Appl. Phys,* 42**,** 235204.

BLAKELOCK, J. H. 1991. *Automatic control of aircraft and missiles,* New York, Wiley.

BLONDEAU, J. E. 2004. *DEVELOPMENT AND TESTING OF A VARIABLE ASPECT RATIO WING USING PNEUMATIC TELESCOPIC SPARS.* MSC, Maryland.

BONNET, J. P. & ANTHOINE, J. 2009. *Flow control : fundamentals, advances and applications,* Rhode Saint Genèse, von Karman Institute for Fluid Dynamics.

CATTAFESTA, L., GARG, S. & SHUKLA, D. 2001. Development of piezoelectric actuators for active flow control. *AIAA,* 39**,** 1562-68.

CATTAFESTA, L. N. & SHEPLAK, M. 2011. Actuators for Active Flow Control. *Annual Review of Fluid Mechanics,* 43**,** 247-272.

CESNIK, C. E. S., LAST, H. R. & MARTIN, C. A. 2004. A FRAMEWORK FOR MORPHING CAPABILITY ASSESSMENT. *45th Structural Dynamics & Materials Conference.* California.

COOK, M. V. 2007. *Flight dynamics principles : [a linear systems approach to aircraft stability and control]*, Oxford UK ; Burlington, MA, Butterworth-Heinemann/Elsevier.

CORKE, T., ENLOE, C. & WILKINSON, S. 2010. Dielectric barrier discharge plasma actuators for flow control. *Annu. Rev. Fluid Mech,* 42**,** 505-29.

CORKE, T., POST, M. & ORLOV, D. 2007. SDBD plasma enhanced aerodynamics: concepts, optimization and applications. *Prog. Aerosp. Sci,* 43**,** 193-217.

DAVIS, M. H. A. & VINTER, R. B. 1985. *Stochastic modelling and control,* London, Chapman and Hall.

DAY, D. 2011. *Slotted Wings, Flaps, and High Lift Devices". US Centennial Flight Commission. 9/06/08* [Online]. Available: <http://www.centennialofflight.gov/essay/Evolution_of_Technology/High_Lift_Devices/Tech6.htm> [Accessed 04/04/2011.

DEARING, S., LAMBERT, S. & MORRISON, J. 2007. Flow control with active dimples. *THE AERONAUTICAL JOURNAL*.

DEWEY, H. H. & PEZHMAN, M. 2013. Passive Morphing of Flying Wing Aircraft - Part I: Z Configuration. *54th AIAA/ASME/ASCE/AHS/ASC Structures, Structural Dynamics, and Materials Conference.* American Institute of Aeronautics and Astronautics.

DIACONU, C. G., WEAVER, P. M. & MATTIONI, F. 2007. Solutions for morphing airfoil sections using bi-stable laminated composite structures. *48th AIAA/ASME/ASCE/AHS/ASC Structures, Structural Dynamics, and Materials Conference.* Honolulu, Hawaii.

DONG, Y., BOMING, Z. & JUN, L. 2008. A changeable aerofoil actuated by shape memory alloy springs. *Materials Science and Engineering* 243-250.

DOYLE, J. & STEIN, G. 1981. Multivariable feedback design: Concepts for a classical/modern synthesis. *Automatic Control, IEEE Transactions on,* 26**,** 4-16.

DURSCHER R, R. S. 2010. Novel multi-barrier plasma actuators for increased thrust. *48th AIAA Aerosp.Sci. Meet.* Orlando.

ELZEY, D. M., SOFLA, A. Y. N. & WADLEY, H. N. G. 2003. A bio-inspired high-authority actuator for shape morphing structures. 92-100.

ENGLISH, B., KERCHER, D. S., LEE, J.-B. & ALLEN, M. G. 2010. *Flow Control Research* [Online]. Georgia Institute of Technology. Available: http://mems.mirc.gatech.edu/research/flow.html [Accessed 01/05/2011 2011].

ETKIN, B. & REID, L. D. 1996. *Dynamics of flight : stability and control,* New York, Wiley.

FONTANAZZA, A., TALLING, R., JACKSON, M., DASHWOOD, R., DYE, D. & IANNUCCI, L. Morphing Wing Technologies Research. 1st SEAS DTC Technical Conference, 2006 Edinburgh.

FORTE, M., JOLIBOIS, J., PONS, J., MOREAU, E., TOUCHARD, G. & CAZALENS, M. 2007. Optimization of a dielectric barrier discharge actuator by stationary and non-stationary measurements of the induced flow velocity: application to airflow control. *Exp. Fluids,* 43**,** 917-28.

FRISWELL, M. I. 2011. *Multistable Structures* [Online]. Available: http://www.aer.bris.ac.uk/research/morphing/multistableStruct.html [Accessed 06/04/2011 2011].

FRISWELL, M. I. & INMAN, D. J. 2006. Morphing Concepts for UAVs. *21st Bristol UAV Systems.*

GALANTAI, V. P., SOFLA, A. Y. N., MEGUID, S. A., TAN, K. T. & YEO, W. K. 2012. Bio-inspired wing morphing for unmanned aerial vehicles using intelligent materials. *International Journal of Mechanics and Materials in Design,* 8**,** 71-79.

GEVERS, D. E. 1997. *Gevers Aircraft, Inc Multi-Purpose Aircraft* 5,645,250.

GILARRANZ, J. L., TRAUB, L. W. & REDINIOTIS, O. K. 2005a. A New Class of Synthetic Jet Actuator – Part I: Design, Fabrication and Bench Top Characterization. *ASME J. Fluids Eng,* 127**,** 367-376.

GILARRANZ, J. L., TRAUB, L. W. & REDINIOTIS, O. K. 2005b. A New Class of Synthetic Jet Actuator – Part II: Application to Flow Separation Control. *ASME J. Fluids Eng,* 127**,** 377-387.

GLEZER, A. & AMITAY, M. 2002. Synthetic jets. *Annu. Rev. Fluid Mech,* 34**,** 503-29.

GOMEZ, J. C. & GARCIA, E. 2011. Morphing unmanned aerial vehicles. *Smart Materials and Structures,* 20.

HOLMAN, R., UTTURKAR, Y., SMITH, B. & CATTAFESTA, L. 2005. Formation Criterion for Synthetic Jets. *AIAA,* 43.

HOROWITZ, I. & BAÑOS, A. 2001. Fundamentals of nonlinear quantitative feedback theory. *In:* BAÑOS, A., LAMNABHI-LAGARRIGUE, F. & MONTOYA, F. (eds.) *Advances in the control of nonlinear systems.* Springer London.

HULL, D. G. 2007. *Fundamentals of airplane flight mechanics,* Berlin ; London, Springer.

HURLEBAUS, S. G., L 2006. Smart structure dynamics. *Mechanical Systems and Signal Processing*.

JACOBSON, S. A. & REYNOLDS, W. C. 1998. Active control of streamwise vortices and streaks in boundary layers. *Fluid Mechanical,* 360**,** 179-211.

JEON, W.-P. & BLACKWELDER, R. F. 2000. Perturbations in the wall region using flush mounted piezoceramic actuators. *Exp Fluids,* 29**,** 485-496.

JOHNSON, T. 2010. *BISTABLE DEVICES FOR MORPHING ROTOR BLADES.* PhD, The Pennsylvania State University.

JOLIBOIS, J. & MOREAU, E. 2009. Enhancement of the electromechanical performances of a single dielectric barrier discharge actuator. *IEEE Trans. Dielectr. Electr. Insul,* 16**,** 758-67.

JOOS, H.-D. 1997. Multi-objective parameter synthesis (MOPS). *In:* MAGNI, J.-F., BENNANI, S. & TERLOUW, J. (eds.) *Robust Flight Control.* Springer Berlin Heidelberg.

JOSLIN, R. D. & MILLER, D. N. 2009. *Fundamentals and applications of modern flow control,* Reston, Va., American Institute of Aeronautics and Astronautics.

KEGERISE, M., CABELL, R. & CATTAFESTA, L. 2007a. Real-time feedback control of flow-induced cavity tones, Part 1: Fixed-gain control. *Sound Vib,* 307**,** 906-23.

KEGERISE, M., R.CABELL & CATTAFESTA, L. 2007b. real-time feedback control of flow-induced cavity tones, Part 2: Adaptive control. *Sound Vib,* 307**,** 924-40.

KLEIN, V. 1979. Determination of Longitudinal aerodynamic derivatives from Steady-state measurement of an aircraft. *Atmospheric Flight Mechanics Conference.* AIAA.

KOTA, S., HETRICKA, J., OSBORNA, R., PAUL, D., PENDLETON, E., FLICK, P. & TILMANN, C. Design and application of compliant mechanisms for morphing aircraft structures,Smart Structures and Materials *In:* ANDERSON, E. H., ed. Industrial and Commercial Applications of Smart Structures Technologies, 2003.

KRIEGSEIS, J., MÖLLER, B., GRUNDMANN, S. & TROPEA, C. 2012. On Performance and Efficiency of Dielectric Barrier Discharge Plasma Actuators for Flow Control Applications. *International Journal of Flow Control,* 4**,** 125-132.

LAZOS, B. 2005 Biologically Inspired Fixed-Wing Configuration Studies *Journal of Aircraft* 42**,** 1089-1098.

LEE, H.-T. 2005. *Computational Investigation of Miniature Trailing Edge Effectors.* PhD PhD, Stanford University.

LV, H., JIANG, C., HOU, H., ZHOU, Z., DENG, J., MA, B. & YUAN, W. 2012. Flexible balloon actuators for active flow control. *Microsystem Technologies,* 18**,** 267-275.

MA, B.-F., LIU, P.-Q. & WEI, Y. 2004. Effects of Wing and Canard Sweep on Lift-Enhancement of Canard-Configurations. *Journal of Aircraft,* 41**,** 1521-1523.

MACIEJOWSKI, J. M. 1989. *Multivariable feedback design,* Wokingham, Addison-Wesley.

MANZO, J. E. 2006. *ANALYSIS AND DESIGN OF A HYPER-ELLIPTICAL CAMBERED SPAN MORPHING AIRCRAFT WING.* MSC, Cornell University.

MATHEW, J., SONG, Q., SANKAR, B., SHEPLAK, M. & CATTAFESTA, L. 2006. Optimized design of piezoelectric flap actuators for active flow control. *AIAA,* 44**,** 2919-28.

MCCLAMROCH, N. H. 2011. *Steady aircraft flight and performance,* Princeton, N.J., Princeton University Press.

MCCORMICK, B. W. 1995. *Aerodynamics, aeronautics, and flight mechanics,* New York, Wiley.

MCCORMICK, D. C. 2000. Boundary Layer Separation Control with Directed Synthetic Jets. *AIAA,* 0519.

MCFARLANE, D. & GLOVER, K. 1992. A loop-shaping design procedure using H_∞ synthesis. *Automatic Control, IEEE Transactions on,* 37**,** 759-769.

MCFARLANE, D. C. & GLOVER, K. 1989. *Robust controller design using normalized coprime factor plant descriptions,* Berlin ; New York, Springer-Verlag.

MCRUER, D., ASHKENAS, I. & GRAHAM, D. 1973. *Aircraft dynamics and automatic control*, Princeton University Press.

MILONIDIS, D. E. 1987. *the development of the mathematical model of a remotely piloted vehicle and an investigation on the use of an extended kalman filter for identification of its aerodynamic derivatives.* m.phil, cranfield

MOREAU, E. 2007. Airflow control by non-thermal plasma actuators. *Phys. D Appl. Phys,* 40**,** 605-36.

MOREAU, E., SOSA, R. & ARTANA, G. 2008. Electric wind produced by surface plasma actuators: a new dielectric barrier discharge based on a three-electrode geometry. *Phys. D Appl. Phys,* 41.

MUELLER, T. J. & BATILL, S. M. 1982. Experimental studies of separation on two-dimensional airfoil at low Reynolds number. *AIAA,* 20**,** 457-463.

NAGIB, H., KIEDAISCH, J., WYGNANSKI, I., STALKER, A., WOOD, T. & MCVEIGH, M. 2004. First-in-flight full-scale application of active flow control: The XV-15 tiltrotor download reduction. *RTO-MP-AVT-111*.

NARAYANASWAMY, V., RAJA, L. & CLEMENS, N. 2010. Characterization of a high-frequency pulsed-plasma jet actuator for supersonic flow control. *AIAA,* 48**,** 297–305.

NARCIS, U., ANDY, K. & NEIL, B. 2006. On the Design of Morphing Airfoils Using Spinal Structures. *47th AIAA/ASME/ASCE/AHS/ASC Structures, Structural Dynamics, and Materials Conference.* American Institute of Aeronautics and Astronautics.

OSGAR, O., BRIAN, D., SETH, T., KEVIN, K., TROY, P., PAUL, G. & JONATHON, C. 2013. Piezoelectric Morphing versus Servo-Actuated MAV Control Surfaces, Part II: Flight Testing. *51st AIAA Aerospace Sciences Meeting including the New Horizons Forum and Aerospace Exposition.* American Institute of Aeronautics and Astronautics.

PAREKH, D., WILLIAMS, S., AMITAY, M., GLEZER, A., WASHBURN, A., GREGORY, I. & SCOTT, R. 2003. Active Flow Control on the Stingray UAV: Aerodynamic Forces and Moments. *AIAA,* 4002.

PERKINS, D. A., REED, J. L. & HAVENS, E. 2004. Adaptive wing structures,. *Smart Structures and Materials and Nondestructive Evaluation for Health Monitoring and Diagnostics conference.* San Diego: International Society for Optical Engineering.

PICK, P., SKÁLA, V. & MATĚJKA, M. 2013. Efficiency of Active Flow Control by a Synthetic Jet Around a Hump. *EPJ Web of Conferences,* 45**,** 01075.

PILON, A. 2004. Aerospace Science. *Aerospace America***,** 13-16.

PINES, J. B. A. D. 2003. Wind Tunnel Testing of a Morphing Aspect Ratio Wing Using an Pneumatic Telescoping Spar. *In:* AIAA (ed.) *2nd AIAA "Unmanned Unlimited" Conf. and Workshop & Exhibit.*

POWERS, S. G., WEBB, L. D., FIREND, E. L. & KOLOS, W. A. 1992. Flight test results from a supercritical mission adaptive wing with smooth variable camber. *NASA technical Memorandum 4415*.

PUGLIESE, A. J. & ENGLAR, R. J. 1979. Flight Testing the circulation Control Wing. *AIAA***,** 79-1791.

RAMAN G, C. A. Innovative actuators for active flow and noise control. Inst. Mech. Eng. Part. G. J. Aerosp. Eng, 2002. 303–24.

RANEY, D. L., CABELL, O. H., SLOAN, A. R., BARNWELL, W. G., LION, S. T. & HAUTAMAKI, B. A. 2004. Wind Tunnel Test of an RPV with Shape-

Change Control Effector and Sensor Arrays. *AIAA Guidance, Navigation & Control Conference.* Providence, Rhode Island.

RANEY, D. L., MONTGOMERY, R. C. & .GREEN, L. L. 2000. Flight Control using Distributed Shape-Change Effector Arrays. *41st AIAA/ASME/ASCE/AHS/ASC Structures, Structural Dynamics, and Materials Conference & Exhibit.* Atlanta, Georgia.

RANEY, D. L. C., RANDOLPH H.; SLOAN, ADAM R.; BARNWELL, WILLIAM G.; LION, S. TODD; HAUTAMAKI, BRET A. 2004. Wind Tunnel Test of an RPV with Shape-Change Control Effector and Sensor Arrays. *AIAA Guidance, Navigation & Control Conference.* Providence, Rhode Island: AIAA

SAMIMY, M., ADAMOVICH, L., WEBB, B., KASTNER, J. & HILEMAN, J. 2004. Development and characterization of plasma actuators for high-speed jet control. *Exp. Fluids,* 37**,** 577-88.

SANDRA, U. 2007. *Experimental Analysis and Analytical Modeling of Synthetic Jet-Cross Flow Interactions.* PhD, University of Maryland.

SANTHANAKRISHNAN, A. & JACOB, J. D. 2007. Flow control with plasma synthetic jet actuators. *Phys. D Appl. Phys,* 40**,** 637-51.

SANTHANAKRISHNAN, A., PERN, N. J., RAMAKUMAR, K., SIMPSON, A. & JACOB, J. D. 2005. Enabling Flow Control Technology for Low Speed UAVs. *AIAA Infotech@Aerospace.*

SEIFERT, A., ELIAHU, S., GREENBLATT, D. & WYGNANSKI, I. 1998. Use of Piezoelectric Actuators for Airfoil Separation Control. *AIAA,* 36**,** 1535-37.

SELIG, M. S. 2011. *UIUC Airfoil Data Site* [Online]. University of Illinois. Available: www.ae.uiuc.edu/m-selig/ads.html [Accessed 10/04/2013.

SHAW, L. L., SMITH, B. R. & SADDOUGHI, S. 2006. Full-scale flight demonstration of active control of a pod wake. *AIAA Flow Control.* San Francisco.

SKOGESTAD, S. & POSTLETHWAITE, I. 2005. *Multivariable feedback control : analysis and design,* Chichester, Wiley.

SMETANA, F. O. 1984. *Computer assisted analysis of aircraft performance, stability, and control,* New York, McGraw-Hill.

SOFLA, A., ELZEY, D. & WADLEY, H. An antagonistic flexural unit cell for design of shape morphing structures. Proceedings of the ASME aerospace division: adaptive materials and systems, aerospace materials and structures, 2004 Anaheim, CA.

SOFLA, A. Y. N., MEGUID, S. A., TAN, K. T. & YEO, W. K. 2009. Shape morphing of aircraft wing: Status and challenges. *Elsevier,* Materials and Design.

SOFLA, A. Y. N., MEGUID, S. A., TAN, K. T. & YEO, W. K. 2010. Shape morphing of aircraft wing: Status and challenges. *Materials & Design,* 31**,** 1284-1292.

STENGEL, R. F. 2004. *Flight dynamics,* Princeton, NJ, Princeton University Press.

THOMAS, F., CORKE, T., IQBAL, M., KOZLOV, A. & SCHATZMAN, D. 2009. Optimization of dielectric barrier discharge plasma actuators for active aerodynamic flow control. *AIAA,* 47**,** 2169-78.

TREBBLE, W. J. G. 1985a. Low-Speed wind-Tunnel Tests on a Full-Scale Unmanned Aircraft (X-RAE1). *AERO 2043*.

TREBBLE, W. J. G. 1985b. *Low-Speed Wind tunnel Tests on a Full-Scale Unmanned Aircraft (X-RAE1),* London,, RAE.

TROY, P., KEVIN, K., BRANDON, S., CHRISTOPHER, H., OSGAR, O., ETAN, K., CHRISTOPHER, O. & AARON, B. 2012. Smart material actuators as a means of UAV flight control. *50th AIAA Aerospace Sciences Meeting including the New Horizons Forum and Aerospace Exposition.* American Institute of Aeronautics and Astronautics.

UTKIN, Y., KESHAV, S., KIM, J., KASTNER, J., ADAMOVICH, I. & SAMIMY, M. 2007. Development and use of localized arc filament plasma actuators for high-speed flow control. *Phys. D Appl. Phys,* 40**,** 685-94.

UTTAMCHANDANI, D. 1994. Fibre-optic sensors and smart structures: Developments and prospects. *Electronics & Communication Engineering* 6**,** 237 - 246.

VALASEK, J. 2012. *Morphing aerospace vehicles and structures,* Chichester, Wiley.

VON MISES, R. 1959. *Theory of flight,* New York,, Dover Publications.

WASHBURN, A. & AMITAY, M. 2004. Active Flow Control on the Stingray UAV: Physical Mechanisms. *AIAA,* 4004.

WASHBURN, A. E. G., ALTHOFF SUSAN; ANDERS, G. SCOTT 2002. A Snapshot of Active Flow Control Research at NASA Langley. *1st Flow Control Conference.* St. Louis, Missouri: AIAA.

WEISSHAAR, T. A. 2006. New Aircraft Systems Concepts-Towards New Horizons in Aeroelasticity. Purdue University.

WENDT, J. F., ANDERSON, J. D. & VON KARMAN INSTITUTE FOR FLUID DYNAMICS. 2009. *Computational fluid dynamics : an introduction,* Berlin, Springer.

WHITEHEAD J., G. I. 2003. Aerodynamics and Propulsion of Synthetic Jet Based Micro Air Vehicles. *AIAA,* 4004.

WIGGINS, L. D., STUBBS, M. D., JOHNSTON, C. O., ROBERTSHAW, H. H., REINHOLTZ, C. F. & INMAN, D. J. 2004. A Design and Analysis of a Morphing Hyper-Elliptic Cambered Span (HECS) Wing. *45th AIAA/ASME/ASCE/AHS/ASC Structures, Structural Dynamics & Materials Conference.* Palm Springs, California.

YECHOUT, T. R. & MORRIS, S. L. 2003. *Introduction to aircraft flight mechanics : performance, static stability, dynamic stability, and classical feedback control,* Reston, VA, American Institute of Aeronautics and Astronautics.

ZIPFEL, P. H. 2007. *Modeling and simulation of aerospace vehicle dynamics,* Reston, Va., American Institute of Aeronautics and Astronautics.